



SAPIENZA  
UNIVERSITÀ DI ROMA

## Constraining Modified Gravity Theories With Cosmology

Scuola di Dottorato in Scienze Astronomiche,  
Chimiche, Fisiche e Matematiche "Vito Volterra"

Dottorato di Ricerca in Fisica – XXIV Ciclo

Candidate

Matteo Martinelli

ID number 698465

Thesis Advisor

Prof. Alessandro Melchiorri

A thesis submitted in partial fulfillment of the requirements  
for the degree of Doctor of Philosophy in Physics

December 2011

Thesis not yet defended

Matteo Martinelli. *Constraining Modified Gravity Theories With  
Cosmology.*

Ph.D. thesis. Sapienza – University of Rome

© 2011

VERSION: December 9, 2011

EMAIL: [Matteo.Martinelli@roma1.infn.it](mailto:Matteo.Martinelli@roma1.infn.it)

## Abstract

We study and constrain the Hu and Sawicki  $f(R)$  model using CMB and weak lensing forecasted data. We also use the same data to constrain extended theories of gravity and the subclass of  $f(R)$  theories using a general parameterization describing departures from General Relativity. Moreover we study and constrain also a Dark Coupling model where Dark Energy and Dark Matter are coupled together.



# Contents

<b>Introduction</b>	<b>vii</b>
<b>1 Cosmological standard model and the cosmological constant problem</b>	<b>1</b>
1.1 Friedmann's equations . . . . .	3
1.1.1 First Friedmann equation . . . . .	4
1.1.2 Second Friedmann equation . . . . .	6
1.2 Redshift and luminosity distance . . . . .	8
1.3 Observations in agreement with the standard cosmological model . .	9
1.3.1 Hubble Law . . . . .	9
1.3.2 Nucleosynthesis . . . . .	10
1.3.3 Cosmic Microwave Background . . . . .	12
1.4 Beyond the homogeneous model: growth of perturbations . . . . .	14
1.4.1 Jeans theory . . . . .	14
1.4.2 Matter perturbations growth . . . . .	17
<b>2 Beyond the standard cosmological model</b>	<b>19</b>
2.1 Dark Matter . . . . .	19
2.2 Dark Energy . . . . .	21
2.2.1 The cosmological constant . . . . .	22
2.2.2 Alternatives to the cosmological constant . . . . .	26
<b>3 Extended Theories of Gravity</b>	<b>31</b>
3.1 $f(R)$ -theories and the Hu and Sawicki model . . . . .	32
3.1.1 Cosmological Viability . . . . .	35
3.1.2 The Hu and Sawicki model . . . . .	36
3.2 General Parameterization of Extended Theories of Gravity . . . . .	42
<b>4 Observational signatures of Extended Theories of Gravity</b>	<b>45</b>
4.1 Background Observables . . . . .	45
4.1.1 Standard Candles . . . . .	45
4.1.2 Standard Rulers . . . . .	47
4.1.3 Hubble Parameter . . . . .	51
4.2 Perturbations Observables . . . . .	52
4.2.1 CMB spectrum . . . . .	52
4.2.2 Weak Lensing . . . . .	59

<b>5</b>	<b>Observational constraints on the Hu and Sawicki Model</b>	<b>63</b>
5.1	Background constraints . . . . .	63
5.2	Forecasted perturbation constraints . . . . .	66
5.2.1	Future Data Analysis and Results . . . . .	68
<b>6</b>	<b>General Constraints on Extended Theories of Gravity</b>	<b>73</b>
6.1	Current CMB constraints . . . . .	73
6.1.1	Data . . . . .	74
6.1.2	Results & constraints . . . . .	75
6.1.3	On the parametrisations and the Bayesian priors . . . . .	78
6.2	Forecasted constraints . . . . .	80
6.2.1	CMB data . . . . .	81
6.2.2	Galaxy weak lensing data . . . . .	82
6.2.3	Forecasted Results . . . . .	84
<b>7</b>	<b>Dark Coupling</b>	<b>93</b>
7.1	Observational Signatures . . . . .	95
7.2	Constraints on Dark Coupling . . . . .	97
<b>8</b>	<b>Conclusion</b>	<b>107</b>
<b>A</b>	<b>Principle of Maximum Likelihood</b>	<b>109</b>
A.1	Statistical Inference . . . . .	110
A.1.1	Likelihood Intervals . . . . .	111
A.2	Monte Carlo Markov Chain . . . . .	115

# Introduction

Cosmology is a science whose purpose is to understand the evolution of the Universe and to explain its observable properties.

In order to do this, many different branches of physics are used, from spectroscopy to particle physics, but the theory that has a fundamental role in describing the Universe is for sure General Relativity.

We can in fact think that modern cosmology was born in 1917, when Einstein applied his gravity theory to describe the Universe; at the time scientists thought that the Universe was finite and static, thus Einstein was forced to introduce a new term, the *cosmological constant* ( $\Lambda$ ), into his equations in order to satisfy these assumptions. A static and finite Universe will in fact collapse under the effect of gravitational interaction and the cosmological constant term can avoid this problem introducing a repulsive interaction that oppose to gravity.

The model considered by Einstein is outdated today; we know, in fact, that the Universe is expanding. The overcoming of this first model of the Universe was possible thanks to the improvement of observational techniques that allowed to study more and more distant astrophysical sources; this allowed, 1929, the discovery of the recession motion of galaxies, that prompted scientist to abandon the static model of the Universe.

The present cosmological model is instead based on the assumption that the Universe is homogeneous and isotropic, at least at first approximation, assumption that is supported by large scale observations and in particular by observations of the cosmic microwave background radiation, one of the best observable validations of the current cosmological model.

Anyway, in order to quantitatively describe the evolution of the Universe it is necessary to identify the energy components of which it is composed, which are non-relativistic matter and radiation. With a Universe containing this two components and ruled by General Relativity it is possible to reproduce the expansion of the Universe observed by Hubble in 1929.

However, recent measures showed that the expansion of the Universe has recently entered in an accelerated phase that can not be explained with ordinary matter and radiation only as components of the Universe.

These observation made the cosmological constant come back into interest as this term, used in an expanding Universe model, is able to explain the acceleration.

Nevertheless, this term is affected by serious theoretical problems connected with its interpretation that drove people to look for models alternative to the cosmological constant; most of these alternative models are based on the introduction of an additional energy component, alongside matter and radiation, able to produce the accelerated phase of the expansion.

However this is not the only way to produce the acceleration; it is in fact possible to think that just matter and radiation are the components of the Universe, but that General Relativity must be modified on cosmological scales. This brings to modified gravity models that can account for the accelerated expansion through a modified gravitational interaction.

In this Thesis this last possibility will be explored with the introduction of a specific modified gravity model and of a parameterization that allows to quantify the deviations from Einsteins' General Relativity. After an introduction to the cosmological standard model in Chapter 1, in Chapter 2 the problems of this model are described and the cosmological constant, *Dark Matter* and *Dark Energy* are introduced.

Chapter 3 is focused on modified gravity models; at first their general properties are analyzed, then the Hu and Sawicki model is introduced. At the end of the Chapter, the parameterization of deviations from General Relativity is described.

In Chapter 4 we focus on the observational signatures of extended theories of gravity; these models change both the expansion trend of the Universe and the evolution of its components, in particular of matter overdensities. In this Chapter we describe the main observables that allow to constrain extended theories of gravity from the background expansion point of view, but we introduce also observables related to the evolution of density perturbation that can constrain the modified gravitational interaction.

In Chapter 5 we focus on the Hu and Sawicki model constraints showing both current background results and forecasted perturbations constraints, showing how future experiments can greatly improve the constraints on this model.

In Chapter 6 instead we constrain deviations from General Relativity using the parameterization described in Chapter 3. We use both current and forecasted CMB data, highlighting the importance of the better sensitivity of future experiments. Moreover we use also weak lensing constrain showing how this observables is important to constrain theories that modify the evolution of matter perturbations.

Finally in Chapter 7 we don't focus anymore the nature of mechanism that produces the accelerated expansion, but we study the possibility that the two dark fluids (dark matter and dark energy) interact with each other. We introduce a model that consider this coupling between the two fluids and we explain how the same perturbation observables introduced in Chapter 4 are able to constrain this model. At the end of the Chapter we show the constraints on the coupling parameter obtained from CMB forecasted data and we also show how future weak lensing missions can greatly improve these constraints.



# Chapter 1

## Cosmological standard model and the cosmological constant problem

Of the four forces existing in nature, gravity is the only dominant one on cosmic scales. The Universe components in fact can only interact through gravity as this is the only forces able to influence bodies at cosmic distances and with no net electric charge.

Therefore, the Universe is described by Einstein's General Relativity and it evolves following Einstein's equations [1]:

$$G_{\mu\nu} = R_{\mu\nu} - \frac{1}{2}g_{\mu\nu}R = \frac{8\pi G}{c^4}T_{\mu\nu} \quad (1.1)$$

where  $G_{\mu\nu}$  is the Einstein tensor,  $R_{\mu\nu}$  the Ricci tensor,  $R$  the Ricci scalar,  $T_{\mu\nu}$  is the global stress-energy tensor of the Universe,  $g_{\mu\nu}$  is the space-time metric and  $g$  its determinant.

Later in this Thesis, we will modify the Einstein's gravity Lagrangian ( $L = \sqrt{-g}R$ ), thus it is useful to introduce how Einstein's equations can be obtained from the Lagrangian through the principle of minimum action.

We start from the Einstein Lagrangian and a matter Lagrangian  $L_m$  and, assuming  $c = 1$ , we write the action

$$S = \frac{1}{16\pi G} \int d^4x \sqrt{-g} (R + 16\pi G L_m) \quad (1.2)$$

We then require the variation of the action  $\delta S$  to vanish, therefore

$$\delta S = \frac{1}{16\pi G} \int d^4x \delta [\sqrt{-g} (R + 16\pi G L_m)] = 0 \quad (1.3)$$

where we are varying the action with respect to  $g_{\mu\nu}$ . We follow the Einstein-Hilbert procedure, where the *connections*  $C_{\mu\nu}^\lambda$ , a geometrical object needed to define the derivatives in a curved space, are identified with the *Christoffel's symbols*

$$\Gamma_{\mu\nu}^\lambda = \frac{1}{2}g^{\lambda\alpha} (g_{\alpha\mu,\nu} + g_{\alpha\nu,\mu} - g_{\mu\nu,\alpha}) \quad (1.4)$$

where the commas denote the ordinary derivative.

Using this method, the Ricci tensor can be thought as a function of the metric and its derivatives; then, also expressing  $R = g^{\mu\nu} R_{\mu\nu}$ , we can rewrite Eq. (1.3) as

$$\begin{aligned} \delta S = \frac{1}{16\pi G} \int d^4x [\delta\sqrt{-g}g^{\mu\nu}R_{\mu\nu} + \sqrt{-g}(\delta g^{\mu\nu}R_{\mu\nu} + g^{\mu\nu}\delta R_{\mu\nu})] + \\ + \int d^4x \delta(\sqrt{-g}L_m) = 0. \end{aligned} \quad (1.5)$$

It is possible to show [2] that

$$\delta\sqrt{-g} = \frac{1}{2}\sqrt{-g}g_{\mu\nu}\delta g^{\mu\nu} \quad (1.6)$$

$$\delta R_{\mu\nu} = \delta\Gamma_{\mu\nu;\lambda}^\lambda - \delta\Gamma_{\mu\lambda;\nu}^\lambda, \quad (1.7)$$

thus the variation of the action can be expressed as

$$\begin{aligned} \delta S = \frac{1}{16\pi G} \int d^4x \left[ \sqrt{-g} \left( R_{\mu\nu} - \frac{1}{2}g_{\mu\nu}R \right) \delta g^{\mu\nu} + \sqrt{-g}g^{\mu\nu} \left( \delta\Gamma_{\mu\nu;\lambda}^\lambda - \delta\Gamma_{\mu\lambda;\nu}^\lambda \right) \right] + \\ + \int d^4x \left( \frac{\delta L_m}{\delta g^{\mu\nu}} - \frac{1}{2}g^{\mu\nu}L_m \right) \delta g^{\mu\nu} \sqrt{-g} = 0. \end{aligned} \quad (1.8)$$

This equation can be further simplified by noticing that the term containing the Christoffel's symbols behaves like a vector's divergence and then vanishes when integrating, while the term containing  $L_m$  can be expressed as

$$\frac{\delta L_m}{\delta g^{\mu\nu}} - \frac{1}{2}g_{\mu\nu}L_m = -\frac{1}{2}T_{\mu\nu}; \quad (1.9)$$

therefore we obtain

$$\delta S = \frac{1}{16\pi G} \int d^4x \sqrt{-g} \delta g^{\mu\nu} \left( R_{\mu\nu} - \frac{1}{2}g_{\mu\nu}R - 8\pi GT_{\mu\nu} \right) = 0. \quad (1.10)$$

This equation must be valid for every  $\delta g^{\mu\nu}$ , thus we obtain the Einstein's equation:

$$G_{\mu\nu} \equiv R_{\mu\nu} - \frac{1}{2}g_{\mu\nu}R = 8\pi GT_{\mu\nu}. \quad (1.11)$$

As said above, these are the equations that rule the evolution of the Universe, therefore we can start to describe quantitatively this evolution, starting with the original model proposed by Einstein, which was based on two main assumptions:

1. the Universe is finite
2. the Universe is static

The first assumption was introduced in order to have a metric completely defined by the stress-energy tensor, while the second one was more than reasonable when Einstein firstly proposed a cosmological solution to his equations; in 1917, in fact, observations only showed stars with small peculiar velocities and only in 1922 nebulae were identified with stellar systems outside our galaxy.

However the two assumptions do not agree with Einstein's equations as gravity

would make a finite and static Universe collapse; thus, Einstein introduced a constant term  $\Lambda$ , in agreement with General Relativity principles and with the Bianchi identity  $\nabla_\nu T^{\mu\nu} = 0$ , obtaining new field equations [3]

$$G_{\mu\nu} = 8\pi GT_{\mu\nu} + \Lambda g_{\mu\nu} \quad (1.12)$$

that in the static Einstein's Universe imply

$$8\pi G\rho = \frac{1}{r^2} = \Lambda \quad (1.13)$$

where  $\rho$  is the matter density of the Universe, made up of matter only, and  $r$  is its curvature radius.

The cosmological constant  $\Lambda$  works as a repulsive force opposed to the collapse of the Universe. However this solution is unstable as changing the value of  $\Lambda$  of Eq. (1.13), the Universe will expand or collapse and the staticity assumption would fail. In 1922 Friedmann proposed a new cosmological model where the staticity assumption was eliminated; he proposed that the Universe was homogeneous, isotropic and expanding. This model was rejected at the beginning as observations suggested a static Universe, but later, in 1929, Hubble discovered the recession of galaxies; these new observations supported the expansion of the Universe, therefore the cosmological constant, needed to obtain a static Universe, was abandoned.

## 1.1 Friedmann's equations

As said above the Friedmann's cosmological model is based on the assumptions of homogeneity and isotropy; observing the Universe close to us these assumptions can seem unrealistic, but if we observe the Universe on bigger scales we notice that anisotropies and dishomogeneities gets very small, thus these assumptions are a good approximation on cosmic scales.

We describe the Universe expressing the distance  $ds$  between two space-time points using the general relativistic formalism:

$$ds^2 = g_{\mu\nu} dx^\mu dx^\nu \quad (1.14)$$

This metric for an expanding, homogeneous and isotropic Universe can be expressed as

$$ds^2 = dt^2 - R^2(t) d\sigma^2 \quad (1.15)$$

with  $t$  the time coordinate,  $R(t)$  is a function describing the variation of spatial distances due to the expansion and  $d\sigma^2$  the spatial part of the line element  $ds^2$

$$d\sigma^2 = \gamma_{ij}(u) du^i du^j \quad (1.16)$$

where  $u^i$  are the three spatial coordinates and  $\gamma_{ij}$  is the 3-dimensional metric.

We are using a coordinate system where no mixed terms ( $g_{0i}$ ) appear in the metric; this is the *comoving coordinate* system where the coordinates follow the isotropic expansion of the Universe. If we use polar coordinates,  $d\sigma$  can be expressed as

$$d\sigma^2 = \frac{d\bar{r}^2}{1 - \bar{k}\bar{r}^2} + \bar{r}^2 d\Omega^2 \quad (1.17)$$

where  $\bar{r}$  is the radial coordinate and  $d\Omega^2 = d\theta^2 + \sin^2\theta d\phi^2$ , while  $\bar{k}$  is connected with curvature by the equation

$$\bar{k} = \frac{{}^3R}{6} \quad (1.18)$$

with  ${}^3R$  the 3-dimensional Ricci scalar. Usually  $\bar{k}$  is normalized in order to assume the value of  $-1$  for an *open Universe*, where the 3-dimensional space curvature is negative,  $0$  for a *flat Universe* and  $+1$  for positive curvature, i.e. a *closed Universe*. In order to better show the different behaviour of the metric with different  $\bar{k}$  values, it is possible to rewrite Eq. (1.17) as

$$d\sigma^2 = d\chi^2 + S_k^2(\chi)d\Omega^2 \quad (1.19)$$

where  $d\chi^2 = d\bar{r}^2/(1 - \bar{k}\bar{r}^2)$  and

$$S_k^2(\chi) \equiv \begin{cases} \sin(\chi), & \text{if } \bar{k} = +1 \\ \chi, & \text{if } \bar{k} = 0 \\ \sinh(\chi), & \text{if } \bar{k} = -1 \end{cases} \quad (1.20)$$

Going back to the Eq. (1.17) expression, we can rewrite  $ds$  as

$$ds^2 = dt^2 - R^2(t) \left[ \frac{d\bar{r}^2}{1 - \bar{k}\bar{r}^2} + \bar{r}^2 d\Omega^2 \right] \quad (1.21)$$

where all the dimensions of the spatial part are in  $R(t)$ . We can now define the dimensionless *scale factor*  $a$  as

$$a(t) \equiv \frac{R(t)}{R_0}, \quad (1.22)$$

where  $R_0$  is  $R(t)$  at present time, and change to coordinates  $r = R_0\bar{r}$  and  $k = \bar{k}/R_0^2$ , obtaining the Friedmann-Robertson-Walker (FRW) expression of the metric for an expanding, homogeneous and isotropic Universe:

$$ds^2 = dt^2 - a^2(t) \left[ \frac{dr^2}{1 - kr^2} + r^2 d\Omega^2 \right]. \quad (1.23)$$

### 1.1.1 First Friedmann equation

We can now solve the Einstein's equations in this metric in order to obtain the evolution of the scale factor  $a$  that describe how the Universe expand.

If we assume that the Universe is flat, we will see later on that cosmological data agree with this assumption,  $ds$  can be written as

$$ds^2 = dt^2 - a^2(t) (dx^2 + dy^2 + dz^2); \quad (1.24)$$

thus in a flat Universe, the Friedmann metric is similar to Minkowski metric where the spatial coordinates, comoving with the expansion, are multiplied for the scale factor which contains all the information about the evolution of the Universe. We can now write the first Einstein equation  $G_{00} = 8\pi GT_{00}$ , computing  $G_{00}$  in the flat Friedmann metric [4], obtaining the *first Friedmann equation*:

$$3 \left( \frac{\dot{a}}{a} \right)^2 = 8\pi GT_{00} \quad (1.25)$$

In order to solve this equation we need the stress-energy tensor for the homogeneous and isotropic Universe; if we consider it as a perfect fluid with energy density  $\rho(t)$  and pressure  $p(t)$ , we have

$$T_{\mu\nu} = \begin{pmatrix} \rho & 0 & 0 & 0 \\ 0 & -p & 0 & 0 \\ 0 & 0 & -p & 0 \\ 0 & 0 & 0 & -p \end{pmatrix}, \quad (1.26)$$

then we can rewrite Eq. (1.25) as

$$3 \left( \frac{\dot{a}}{a} \right)^2 = 8\pi G \rho(t) \quad (1.27)$$

Therefore, we need to know the components of the Universe and how their energy densities  $\rho$  evolve with the scale factor. The Universe is surely composed by matter and radiation, i.e. non-relativistic and relativistic particles; the former's energy density is  $\rho_m = \rho_0^m/a^3$  while for the latter  $\rho_r = \rho_0^r/a^4$  where  $\rho_0^i$  is the energy density at the present time and therefore an observable quantity.

These relations between the energy densities and the scale factor can be explained considering the two components nature: non-relativistic matter has an energy density given by the rest mass of particles multiplied by their number density which is in inverse proportion to the volume, so  $\rho_m \propto a^{-3}$ . Relativistic particles instead have an additional  $1/a$  term due to the fact that their energy is in inverse proportion to their wavelength which is stretched by the Universe expansion; thus  $\rho_r \propto a^{-4}$ .

We can now solve the Friedmann equation for the different kinds of energy density; using the expression for  $\rho_m$  in Eq. (1.27) we get

$$a(t) \propto t^{\frac{2}{3}}. \quad (1.28)$$

What we obtain is that, once the staticity assumption is removed, the Universe expansion is a result of the Einstein equations solution in the Friedmann metric, without any need for further assumptions.

If we use the expression for  $\rho_r$  we get

$$a(t) \propto \sqrt{t}, \quad (1.29)$$

so the difference between the two components is the expansion rate they produce. Through the Friedmann equation we can study how the cosmological constant would affect the expansion rate of the Universe. We don't consider it as a term introduced to obtain a static Universe, but as a new energy component. As said above the modified Einstein equations are

$$G_{\mu\nu} = 8\pi G T_{\mu\nu} + \Lambda g_{\mu\nu}, \quad (1.30)$$

so  $\Lambda$  behaves like a fluid which energy density is constant during the expansion of the Universe. If we solve Eq. (1.27) assuming  $\Lambda$  is the only component of the Universe, we obtain

$$\left( \frac{\dot{a}}{a} \right)^2 = \frac{\Lambda}{3} \Rightarrow a(t) = e^{\sqrt{\frac{\Lambda}{3}}t}. \quad (1.31)$$

In order to better understand the evolution of the Universe, we can rewrite the Friedmann equation when these three components are co-existent:

$$\left(\frac{\dot{a}}{a}\right)^2 = \frac{8\pi G}{3} \left[ \frac{\rho_r}{a^4} + \frac{\rho_m}{a^3} + \frac{\Lambda}{8\pi G} \right] \quad (1.32)$$

From this equation we can see that the Universe has three different phases of evolution; for instance radiation will be dominant for small values of the scale factor (at the beginning of the Universe) and it will determine the expansion rate, while it will be sub-dominant at more recent times. The only assumption behind Eq. (1.32) is that the interaction between the energy components is small; if this does not apply the interactions must be taken into account.

Introducing the *Hubble parameter*  $H = \dot{a}/a$ , connected with the expansion rate, the critical density  $\rho_c = 3H_0^2/8\pi G$ , where  $H_0$  is the *Hubble constant* (the present value of the Hubble parameter), and  $\Omega_i = \rho_i/\rho_c$ , Eq. (1.32) can be also expressed as

$$\left(\frac{H}{H_0}\right)^2 = \frac{\Omega_r}{a^4} + \frac{\Omega_m}{a^3} + \Omega_\Lambda. \quad (1.33)$$

If we now relax the assumption of flat Universe, we have to use the more general line element

$$ds^2 = dt^2 - a(t)^2 \left[ \frac{dr^2}{1 - kr^2} + r^2 d\Omega^2 \right] \quad (1.34)$$

and we must include the effect of space-time curvature, which behaves in the Friedmann equation as an additional component of the Universe

$$\frac{H^2}{H_0^2} = \frac{\Omega_r}{a^4} + \frac{\Omega_m}{a^3} + \Omega_\Lambda - \frac{k}{H_0^2 a^2} = \frac{\Omega_r}{a^4} + \frac{\Omega_m}{a^3} + \Omega_\Lambda - \frac{\Omega_k}{a^2} \quad (1.35)$$

where  $\Omega_k = k/H_0^2$ . If we consider this equation at present time, where  $H = H_0$  and  $a = 1$ , we obtain

$$1 - \Omega_k = \Omega_r + \Omega_m + \Omega_\Lambda. \quad (1.36)$$

Therefore is possible to infer the curvature sign and value from the total energy density of the Universe at present time  $\rho_T^0 = \rho_r^0 + \rho_m^0 + \rho_\Lambda^0$ :

- $\rho_T^0 > \rho_c \Rightarrow \Omega_k < 0$  closed Universe
- $\rho_T^0 < \rho_c \Rightarrow \Omega_k > 0$  open Universe
- $\rho_T^0 = \rho_c \Rightarrow \Omega_k = 0$  flat Universe

Thus, the Universe total energy density is an observable that can be used to understand how the curvature of space-time affects the expansion of the Universe.

### 1.1.2 Second Friedmann equation

The results obtained above come only from the first Einstein equation; we can therefore consider the spatial part of Einstein equations  $G_j^i = 8\pi G T_j^i$  obtaining

$$\frac{\ddot{a}}{a} + 2 \left(\frac{\dot{a}}{a}\right)^2 + 2 \frac{k}{a^2} = 4\pi G (\rho - p). \quad (1.37)$$

The  $k$  term can be eliminated using Eq. (1.35), obtaining the second Friedmann equation:

$$\frac{\ddot{a}}{a} = -\frac{4\pi G}{3}(\rho + 3p). \quad (1.38)$$

This equation gives us informations on the second derivative of the scale factor, allowing us to know the acceleration of the expansion of the Universe; however to solve this equation we need an equation of state  $p = p(\rho)$  for every component of the Universe. In order to do this, we can derive Eq. (1.27) and, using Eq. (1.38), we obtain the continuity equation

$$\frac{d\rho}{dt} = -3(\rho + p)\frac{1}{a}\frac{da}{dt} \quad (1.39)$$

that, when using the perfect fluid equation of state  $p = w\rho$ , leads to

$$\frac{d\rho}{dt} = -3\rho(1+w)\frac{1}{a}\frac{da}{dt} \Rightarrow \rho = \begin{cases} \frac{\rho^0}{a^{3(1+w)}}, & \text{if } w = \text{const} \\ \rho^0 e^{\int_a^1 \frac{3[1+w(a)]}{a} da}, & \text{if } w = w(a) \end{cases} \quad (1.40)$$

This equation allows to analytically study how energy density goes with the scale factor, obtaining what we said above for the different component of the Universe; in fact if we take the perfect fluid equation of state  $p = \rho kT/\mu c^2 = \rho \langle v^2 \rangle / 3\mu c^2$ , we obtain  $w \approx 0$  for non relativistic matter and  $w \approx 1/3$  for relativistic particles, thus for these component we have  $\rho_m \propto a^{-3}$  and  $\rho_r \propto a^{-4}$ . Therefore, from Eq. (1.40) we can obtain also the equation of state for the cosmological constant component; in fact, in order to have a constant  $\rho_\Lambda$ , we need  $w = -1$ , thus  $p_\Lambda = -\rho_\Lambda$ . We can now see how the different components affect the second derivative of the scale factor:

- Matter dominance,  $p = 0 \Rightarrow \ddot{a} < 0$ . Decelerated expansion
- Radiation dominance,  $p = \rho/3 \Rightarrow \ddot{a} < 0$ . Decelerated expansion
- $\Lambda$  dominance,  $p = -\rho \Rightarrow \ddot{a} > 0$ . Accelerated expansion

In order to better understand the effect of the components on the acceleration of the Universe, we can define the *deceleration parameter* ( $q_0$ ) that is negative for an accelerated expansion and positive for a decelerated one:

$$q_0 = -\frac{1}{H_0^2} \left( \frac{\ddot{a}}{a} \right)_{t=t_0}. \quad (1.41)$$

This parameter can be expressed in terms of the  $\Omega_i$  as

$$q_0 = \frac{\Omega_m}{2} + \Omega_r - \Omega_\Lambda; \quad (1.42)$$

therefore, if observations agree with an accelerated expansion, the standard cosmological model with only matter and radiation can not explain it, but a cosmological constant or a different component with a similar equation of state would be needed to produce a  $q_0 < 0$ .

## 1.2 Redshift and luminosity distance

In order to obtain observables to test the cosmological standard model, we need to define distances in the FRW metric. We can calculate the infinitesimal distance that a photon ( $ds^2 = 0$ ) travel in the comoving reference frame as

$$d\tau = \frac{cdt}{a(t)} = \frac{cda}{a^2 H}. \quad (1.43)$$

Let us consider a photon emitted at time  $t_e$ ; the distance travelled by it can be computed integrating  $d\tau$  from the emission time to the present time  $t_0$ . The following wave front will be emitted at  $t_e + \lambda_e/c$  and observed at  $t_0 + \lambda_0/c$ , thus

$$\tau = \int_{t_e + \lambda_e/c}^{t_0 + \lambda_0/c} \frac{cdt}{a(t)} = \int_{t_e}^{t_0} \frac{cdt}{a(t)}; \quad (1.44)$$

this relation can be also expressed as

$$\int_{t_e}^{t_e + \lambda_e/c} \frac{cdt}{a(t)} = \int_{t_0}^{t_0 + \lambda_0/c} \frac{cdt}{a(t)}. \quad (1.45)$$

We will later see that the life time of the Universe is proportional to  $H_0^{-1}$ , a quantity that is much larger than  $\lambda_0/c$  or  $\lambda_e/c$ ; therefore we can think of  $a(t)$  as constant during the integration time, obtaining

$$\frac{\lambda_e}{a(t_e)} = \frac{\lambda_0}{a(t_0)}. \quad (1.46)$$

Using a generic emission time  $t$  and the identity  $a(t_0) = 1$  we can define the *redshift*  $z$

$$z \equiv \frac{\lambda_0 - \lambda_e}{\lambda_e} \Rightarrow 1 + z = \frac{a(t_0)}{a(t)} = \frac{1}{a(t)} \quad (1.47)$$

that can be seen, at first approximation, as the Doppler shift on wavelengths produced by the recession of light sources due to the expansion of the Universe.

This redshift can be connected to the *proper distance*  $d(z)$ , which is the distance in the comoving reference frame:

$$d(z) = c \int_a^1 \frac{da}{a^2 H(a)}. \quad (1.48)$$

However, this distance is not directly observable, but can be connected to the *luminosity distance*  $d_L$ . This distance is connected to the observation of radiation flux ( $F$ ) from astrophysical sources; in a flat Universe the flux of a source, on a sphere with radius the distance between the source itself and the observer, it's related to the luminosity ( $L$ ) of the source by the equation  $F = L/4\pi d_L^2$ , while in the comoving refence frame this equation become  $F = a^2(t)L/4\pi d^2$ , where the scale factor takes into account the photons' energy loss and the decrease of their number due to the expansion. Therefore, we can relate the two distances as  $d_L(z) = d(z)/a(t) = (1+z)d(z)$ , obtaining

$$d_L(a) = \frac{1}{a} \int_a^1 \frac{cda}{a^2 H(a)}. \quad (1.49)$$



Through the Friedmann equations, we can approximate the scale factor as  $a \approx 1 + H_0(t - t_0) - q_0 H_0^2(t - t_0)^2/2$ , obtaining

$$d_L(z) = \frac{cz}{H_0} \left[ 1 + \frac{1}{2} (1 - q_0) z \right] + O(z^3). \quad (1.50)$$

When  $z \ll 1$  we have  $d_L = czH_0^{-1}$  which is the *Hubble law* that shows how more distance sources moves away from us faster; as said before, it was the observation of this collective recession motion that prompted to abandon the static Universe and to accept the expanding universe suggested by Friedmann.

Moreover, in Eq.(1.50) we can see that at larger redshifts we will have deviations from the Hubble law and that these are connected with the deceleration parameter; if the Universe expansion is accelerated, in fact, the luminosity distance will be larger than in a decelerated Universe.

### 1.3 Observations in agreement with the standard cosmological model

In this Section we want to analyze the observations that support the cosmological standard model described above. As we previously said one of the main feature of the model is the expansion of space-time; the Friedmann metric introduces the expansion of spatial coordinates and this can be described, at low redshifts, by the Hubble law, thus, measuring the luminosity distance at different redshifts it is possible to test the expansion. Moreover, the assumption of an expanding Universe brings to the fact that the Universe was much more dense and hot at past times; this implies that at some point the Universe was fully ionized and therefore it was opaque to photons. When the temperature became low enough for the recombination of free electrons with atomic nuclei, the photons started to travel freely forming a background radiation that we must see now. Furthermore the evolution of temperature can be calculated and through this property is possible to compute the theoretical abundances of light elements formed during the cooling of the Universe.

#### 1.3.1 Hubble Law

First of all we should verify that the Universe is expanding, as this is one of the main assumption done to build the FRW metric. As said before, if  $z \ll 1$ , the expansion is described by the law  $d_L = czH_0^{-1}$ , pointing out that more a source is far from us the higher its velocity of recession will be. In 1929, Hubble analyzed the relation between the redshift of some galaxies and their distance from us, finding out that the more redshifted galaxies are the more distant ones; assuming that the Earth is not in a peculiar position in the Universe and therefore that the same behaviour could be observed from everywhere, this means that the Universe is expanding. As said before it was this discovery that confuted Einstein's static Universe, as it is in agreement with Friedmann's expanding Universe.

These observations are performed using galaxies as *standard candles*, i.e. sources with a known luminosity, through the Tulley-Fisher relation [5]; knowing the intrinsic luminosity of the sources allows to calculate the observational luminosity

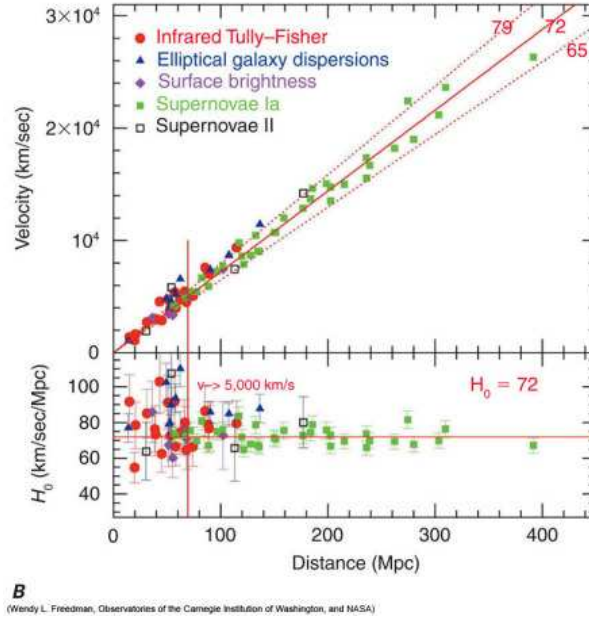


**Figure 1.1.** Hubble law for different values of  $H_0$  plotted alongside experimental data.

distance and, observing the redshift of wavelength of the galaxies, to obtain the reduced Hubble parameter

$$h_0 = \frac{H_0}{100 \text{ km s}^{-1} \text{ Mpc}^{-1}} \quad (1.51)$$

that was measured as  $h_0 = 0.71 \pm 0.025$  by WMAP7 [6].

We will later see how, going to higher redshifts, the luminosity distance will depart from the Hubble law and we will have to take into account the other terms of Eq.(1.50). This departure from the low redshift behaviour will show that the Universe is in an accelerated expansion phase and that we need an additional energy component alongside matter and radiation.

### 1.3.2 Nucleosynthesis

We explained above that in an expanding Universe the scale factor increases with time. This means that in the past the scale factor was lower than at present time, implying that density was higher; inevitably this brings to the fact that the temperature  $T$  of the Universe was higher and that, if we go back enough in time, the Universe was completely ionized. Thus, the primordial fluid was composed of protons, neutrons, electrons and photons in equilibrium through the reactions

$$\gamma + \gamma \rightleftharpoons e^+ + e^-$$

$$n + \nu_e \rightleftharpoons p + e^-$$

$$n + e^+ \rightleftharpoons p + \bar{\nu}_e$$

The temperature will decrease with time and it will become lower than the binding energy of the lightest nuclei; when this happens light nuclei will form starting the process known as *primordial nucleosynthesis*.

We can write the distribution function of the species at the thermodynamic equilibrium as

$$f = \left( e^{E/kT} \pm 1 \right)^{-1}, \quad (1.52)$$

where we have a positive sign for bosons, the negative one for fermions and  $k$  is the Boltzmann constant; using this function we can determine the number density  $n$ , the energy density  $\rho$  and pressure  $P$  of the different species:

$$n = \frac{g}{(2\pi\hbar)^3} \int_0^\infty \frac{4\pi p^2}{e^{E/kT} \pm 1} dp \quad (1.53)$$

$$\rho = \frac{g}{(2\pi\hbar)^3} \int_0^\infty E \frac{4\pi p^2}{e^{E/kT} \pm 1} dp \quad (1.54)$$

$$P = \frac{g}{(2\pi\hbar)^3} \int_0^\infty \frac{p^2}{E} \frac{4\pi p^2}{e^{E/kT} \pm 1} dp \quad (1.55)$$

where  $g$  is the number of degrees of freedom of the considered species and  $p$  is the momentum.

We can now obtain the numerical density of an element with mass number  $A$  through the Saha equation in the non-relativistic limit

$$n_A = g_A \left( \frac{m_A T}{2\pi} \right)^{3/2} e^{-\frac{m_A - \mu_A}{T}}; \quad (1.56)$$

if at equilibrium, the chemical potential of a nucleus is the sum of the chemical potentials of its components, therefore it is possible to show that, expressing  $\mu_p$  and  $\mu_n$  as  $n_p$  and  $n_n$ , we obtain:

$$n_A = g_A 2^{-A} \left( \frac{m_A}{m_p^Z m_n^{A-Z}} \right)^{3/2} \left( \frac{2\pi\hbar}{kT} \right)^{3(A-1)/2} n_p^Z n_n^{A-Z} e^{\frac{B_A}{kT}} \quad (1.57)$$

where  $B_A$  is the binding energy of the nucleus. According to this equation, the number density  $n_A$  should increase rapidly once  $kT < B_A$ ; however we must consider that the baryon density is much smaller than the photon density, therefore, in order to form nuclei, temperature must be much lower than the binding energy. We introduce the  $\eta$  parameter, defined as the ratio of this two densities and measured as [9]

$$\eta = \frac{n_b}{n_\gamma} = (5.5 \pm 0.5) \times 10^{-10}. \quad (1.58)$$

The mass fraction of the element  $A$  can now be expressed as

$$X_A = A \frac{n_A}{n_b} = A \frac{n_A}{n_\gamma} \eta^{-1} \quad (1.59)$$

and, substituting the relation for  $n_A$ , we obtain

$$X_A \propto \eta^{A-1} e^{\frac{B_A}{kT}}. \quad (1.60)$$

Another important parameter needed to calculate elements abundance is the ratio between the number of protons and neutrons. Defining  $Q = m_n - m_p \approx 1.29 \text{ MeV}$ , we have that until  $kT \gg Q$  the number of neutrons and protons is approximately the same, as the reaction that connects the two species is efficient in both ways. When  $kT \ll Q$ , instead, the number of neutrons drops and the ratio between  $n_n$  and  $n_p$  will keep constant as soon as the two species are no more in thermodynamical equilibrium.

In particular, this ratio strongly affects the abundance of primordial helium; this element is composed by two protons and two neutrons, thus  $n_{He} \approx n_n/2$  and its abundance can be wrote as

$$Y = A \frac{n_{He}}{n_b} = \frac{4(n_n/2n_p)}{1 + (n_n/n_p)} \approx 0.25. \quad (1.61)$$

This value is in good agreement with the helium abundance measured in the Universe [9], therefore we can conclude that primordial nucleosynthesis is another observational evidence of the expanding Universe model.

### 1.3.3 Cosmic Microwave Background

As said above, the expansion model predicts an Universe which is much hotter in the past and, therefore, filled with ionized matter. This means that matter and photons are in the past a single fluid, interacting through Thomson scattering, at thermal equilibrium. Thomson scattering has an interaction rate given by

$$\Gamma = n_e \sigma_e c, \quad (1.62)$$

where  $n_e$  is the electrons numerical density and  $\sigma_e = 6.65 \times 10^{-29} \text{ m}^2$  is the cross Section. In order to maintain the equilibrium, the Thomson scattering timescale  $\tau = 1/\Gamma$  has to be smaller than the timescale of the expansion, thus  $\tau < 1/H$ . This condition is satisfied throughout the radiation dominated phase of the expansion ( $\Omega_r(1+z)^4 \gg \Omega_m(1+z)^3$ ), where  $\tau \propto t^{3/2}$  and  $1/H = 2t$ . After the matter-radiation equivalence,  $1/H = 3t/2$  and  $\tau \propto t^2$  and therefore the  $\tau < 1/H$  condition will be violated at some point, in particular at  $z \approx 1100$  [10]. At this point the Universe become transparent to photons and they will propagate freely; however they will keep memory of their thermal equilibrium showing a black body spectrum. The maximum of this spectrum will be in the microwaves because the expansion decreases the photons' energy density

$$\rho_\gamma = \sigma T^4 \propto \frac{1}{a^4}. \quad (1.63)$$

Therefore the expansion model predicts that the primordial Universe is opaque to photons and that a black body background radiation must be now observable at the microwave wavelengths; this radiation is called *Cosmic Microwave Background* (CMB).

In 1964, an isotropic microwave radiation was discovered and through further experiments [7, 8] it was possible to observe that this radiation has a black body spectrum (see Fig.1.2) with a temperature of  $T_0 = (2.725 \pm 0.004) \text{ K}$ , therefore obtaining another observational evidence of the expanding Universe model.

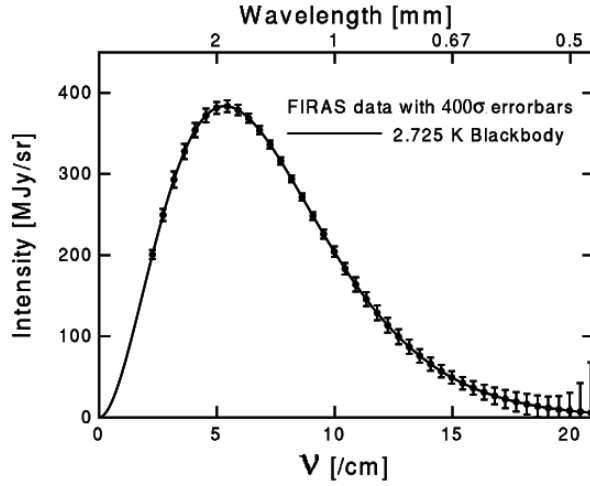


**Figure 1.2.** Black body spectrum of the CMB as detected by COBE satellite [7]

The measure of CMB temperature shows that radiation is no more important in the Universe energetic budget as  $T \approx 2.725$  brings to  $\Omega_r \approx 8.4 \times 10^{-5}$ . Moreover, the CMB allows to analyze the isotropy and homogeneity of the Universe at very high redshift, probing distances much larger than the ones allowed by galaxies observations. In fact, it is possible to map the CMB observing temperature fluctuation around the mean value  $T_0 = \langle T \rangle$ ,

$$\frac{\delta T}{T}(\theta, \phi) = \frac{T(\theta, \phi) - \langle T \rangle}{\langle T \rangle}; \quad (1.64)$$

it was measured [10] that the root mean square temperature fluctuation are very small

$$\sqrt{\left(\frac{\delta T}{T}\right)^2} \approx 10^{-5} \quad (1.65)$$

supporting the approximation of homogeneous and isotropic Universe.

The small temperature fluctuations can be connected to the presence of matter over and subdensities, as the presence of more or less deep gravitational potential wells affects the redshift of CMB photons and thus their temperature. These perturbations on matter density will evolve because of gravity and will form the structures existing today; therefore the initial conditions for structures evolution are imprinted on the CMB radiation.

In Chapter 4 we will see in detail how CMB power spectra are produced and how these can be used to constrain cosmological parameters; these can in fact be used to understand how the initial perturbations evolve before the recombination of protons and electrons. Moreover we will see that a particular perturbation scale is imprinted in the CMB; this particular scale is connected to the Baryon Acoustic Oscillations (BAO), an effect due to the fact that perturbations of the photo-baryonic fluid oscillate under contrasting actions of gravity and radiation pressure.

## 1.4 Beyond the homogeneous model: growth of perturbations

Introducing the CMB we explained that the homogeneity and isotropy of the Universe are true only at first approximation; small fluctuations can be observed in the microwave background and, as said above, can be connected to density perturbations that will grow because gravitational interaction.

In this Section we will introduce the equations that rule this growth, but we will not cover in detail the statistical properties of density perturbations (see [11] for details).

### 1.4.1 Jeans theory

We can study the Newtonian evolution of matter fluctuations if these have a scale smaller than the horizon radius, otherwise we must consider general relativistic effects. In the first case, the equations that rule the growth of perturbations are the continuity equation, the Euler equation, the Poisson equation and the entropy conservation:

$$\frac{\partial \rho}{\partial t} + \nabla \cdot \rho \mathbf{v} = 0 \quad (1.66)$$

$$\frac{\partial \mathbf{v}}{\partial t} + (\mathbf{v} \cdot \nabla) \mathbf{v} + \frac{1}{\rho} \nabla P + \nabla \Psi = 0 \quad (1.67)$$

$$\nabla^2 \Psi = 4\pi G \rho \quad (1.68)$$

$$\frac{\partial s}{\partial t} + \mathbf{v} \cdot \nabla s = 0 \quad (1.69)$$

where  $\rho$  is the density,  $P$  the pressure,  $\mathbf{v}$  the local velocity of the considered fluid,  $\Psi$  the gravitational potential and  $s$  the entropy density.

These equations have a static solution  $\rho = \rho_0$ ,  $\mathbf{v} = \mathbf{0}$ ,  $s = s_0$ ,  $P = P_0$ ,  $\nabla \Psi = 0$ ; it is also possible to see that if  $\rho_0 \neq 0$  the potential must vary in space, therefore an homogeneous density distribution can not be stationary, but has to collapse or expand.

What we want to find is a solution that is a small perturbation of the static solution:  $\rho = \rho_0 + \delta\rho$ ,  $\mathbf{v} = \delta\mathbf{v}$ ,  $s = s_0 + \delta s$ ,  $P = P_0 + \delta P$ ,  $\Psi = \Psi_0 + \delta\Psi$ . Substituting these expression in the previous equations and stopping at first perturbative order, we obtain

$$\frac{\partial \delta\rho}{\partial t} + \rho_0 \nabla \cdot \delta\mathbf{v} = 0 \quad (1.70)$$

$$\frac{\partial \delta\mathbf{v}}{\partial t} + \frac{c_s^2}{\rho_0} \nabla \delta\rho + \frac{1}{\rho_0} \left( \frac{\partial P}{\partial s} \right)_\rho \nabla \delta s + \nabla \delta\Psi = 0 \quad (1.71)$$

$$\nabla^2 \delta\Psi = 4\pi G \delta\rho \quad (1.72)$$

$$\frac{\partial \delta s}{\partial t} = 0 \quad (1.73)$$

where we introduced the sound speed  $c_s^2 = (\partial P / \partial \rho)_s$ .

These equations will have a superposition of plane waves as solutions

$$\delta u(\mathbf{r}, t) = \sum_{\mathbf{k}} \delta u_{\mathbf{k}} \exp(i\mathbf{k} \cdot \mathbf{r} + i\omega t) \quad (1.74)$$

where  $\mathbf{r}$  is the position vector,  $\mathbf{k}$  the wave vector and  $\omega$  the frequency. This formalism can be applied to all the variables of the previous equations that, therefore, can be wrote in Fourier space as

$$\omega \delta_k + \mathbf{k} \cdot \delta \mathbf{v}_k = 0 \quad (1.75)$$

$$\omega \delta \mathbf{v}_k = -\mathbf{k} \left[ c_s^2 \delta_k + \frac{1}{\rho_0} \left( \frac{\partial P}{\partial s} \right)_\rho \delta s_k + \delta \Psi_k \right] \quad (1.76)$$

$$-k^2 \delta \Psi_k = 4\pi G \delta \rho_k \quad (1.77)$$

$$\omega \delta s_k = 0 \quad (1.78)$$

where  $\delta_k = \delta \rho_k / \rho_0$ .

In order to not have a vanishing solution, the frequency  $\omega$  must satisfy the equation

$$\omega^2 - c_s^2 k^2 + 4\pi G \rho_0 = 0. \quad (1.79)$$

Considering only density fluctuations  $\delta \rho$  we will have a gravitational instability when the wavelenght  $\lambda$  of the fluctuation is greater than the *Jeans wavelenght*

$$\lambda_J = c_s^2 \sqrt{\frac{\pi}{G \rho_0}}; \quad (1.80)$$

in fact when  $\lambda > \lambda_J$ , the solution for  $\delta \rho$  is

$$\delta \rho(\mathbf{r}, t) = \delta \rho_k \exp \left\{ i \mathbf{k} \cdot \mathbf{r} \pm i \sqrt{4\pi G \rho_0 \left[ 1 - \left( \frac{\lambda_J}{\lambda} \right)^2 \right]} t \right\} \quad (1.81)$$

which describes a stationary wave with increasing or decreasing amplitude.

These considerations were done without considering the expansion of the Universe; in order to include this effect we need to modify the equations. If we define  $\mathbf{r}$  as the physical distance, the solution for an homogeneous and isotropic matter distribution is

$$\rho = \rho_0 a^{-3} \quad (1.82)$$

$$\mathbf{v} = \frac{\dot{a}}{a} \mathbf{r} \quad (1.83)$$

$$\Psi = \frac{2}{3} \pi G \rho r^2 \quad (1.84)$$

$$P = P(\rho, s) \quad (1.85)$$

$$s = \text{const.} \quad (1.86)$$

where the dot is the derivative with respect to time.

As we did before, we consider a small perturbation to this solution stopping at first order

$$\dot{\delta \rho} + 3 \frac{\dot{a}}{a} \delta \rho + \frac{\dot{a}}{a} (\mathbf{r} \cdot \nabla) \delta \rho + \rho (\nabla \cdot \delta \mathbf{v}) = 0 \quad (1.87)$$

$$\dot{\delta \mathbf{v}} + \frac{\dot{a}}{a} \delta \mathbf{v} + \frac{\dot{a}}{a} (\mathbf{r} \cdot \nabla) \delta \mathbf{v} = -\frac{1}{\rho} \nabla \delta P - \nabla \delta \Psi \quad (1.88)$$

$$\nabla^2 \delta \Psi = 4\pi G \delta \rho \quad (1.89)$$

$$\dot{\delta}s + \frac{\dot{a}}{a}(\mathbf{r} \cdot \nabla)\delta s = 0 \quad (1.90)$$

We look again for solution as superposition of plane waves and, for example looking at the density field, we obtain:

$$\ddot{\delta}_k + 2\frac{\dot{a}}{a}\dot{\delta}_k + \left(c_s^2 k^2 - 4\pi G\rho\right)\delta_k = 0. \quad (1.91)$$

The solution of this equation depends on the properties of the medium in which matter is embedded; if we assume a flat, matter dominated Universe ( $\Omega_m = 1$ ), also known as *Einstein-De Sitter*, which is characterised by  $\rho = 1/6\pi G t^2$ ,  $a = a_0(t/t_0)^2/3$  and  $\dot{a}/a = 2/3t$ , we obtain

$$\ddot{\delta}_k + \frac{4}{3}\frac{\dot{\delta}_k}{t} - \frac{2}{3t^2}\left(1 - \frac{c_s^2 k^2}{4\pi G\rho}\right)\delta_k = 0. \quad (1.92)$$

We can look for a solution as a power law,  $\delta \propto t^n$ , obtaining a dispersion relation expressed as

$$3n^2 + n + 2\left(\frac{c_s^2 k^2}{4\pi G\rho} - 1\right) = 0; \quad (1.93)$$

we will obtain an oscillating solution if  $n$  has imaginary value, while if  $n$  is real we will get a perturbation with a varying amplitude. These two regimes can be discriminated through the Jeans length

$$\lambda_J(t) = \frac{c_s}{5}\sqrt{\frac{24\pi}{G\rho_0(t)}}. \quad (1.94)$$

If  $\lambda < \lambda_J$  we obtain acoustic waves with a slightly decreasing amplitude, while if  $\lambda > \lambda_J$  we have two solutions, one increasing and one decreasing

$$\delta_{\pm}(\mathbf{r}, t) = e^{i\mathbf{k} \cdot \mathbf{r}} t^{-\frac{1}{6} \pm \frac{5i}{6}\sqrt{1-(\lambda_J/\lambda)^2}} \quad (1.95)$$

that for  $\lambda \gg \lambda_J$  can be expressed as

$$\delta_+(\mathbf{r}, t) \propto t^{\frac{2}{3}} \propto a \quad (1.96)$$

$$\delta_-(\mathbf{r}, t) \propto t^{-1} \propto a^{-\frac{2}{3}}. \quad (1.97)$$

These solutions were obtained in a matter dominated Universe, but it's possible to show that solving Eq.(1.91) in a radiation dominated Universe leads to the solutions

$$\delta_+(\mathbf{r}, t) \propto a^2 \quad (1.98)$$

$$\delta_-(\mathbf{r}, t) \propto a^{-2}, \quad (1.99)$$

while if we assume that  $\Lambda$  is the dominant component, we obtain  $\delta \approx \text{const.}$  Moreover, at primordial times, the wavelengths of every perturbation is bigger than the causal horizon dimension. Therefore every perturbation with  $\lambda \ll r_H$  today, has entered the horizon at a time  $t_{in}$  in the past. Thus, the newtonian approximation that we used only holds for  $t \gg t_{in}$ , while the primordial evolution must be calculated considering also relativistic effects.



### 1.4.2 Matter perturbations growth

In a Universe with more than one component, the evolution of an overdensity will depend on the component that we are perturbing, that is if we are considering an overdensity of dark matter or barionic matter, and on the component that dominates the expansion of the Universe at the considered time.

If we study only scales much greater than the Jeans length, the differential equation that rules the evolution of perturbations can be expressed as

$$\ddot{\delta} + 2H\dot{\delta} = 4\pi G\rho\delta. \quad (1.100)$$

In this equation we will have to replace to  $\delta$  the density contrast of the considered component, to  $\rho$  the energy density of the gravitationally dominant component and to  $H$  the respective Hubble parameter. Therefore, we will have three different equation to solve in order to study the evolution of radiation, dark matter or bayons overdensities.

The Jeans condition can be also thought as condition requiring that the time scale needed by pressure to re-establish the equilibrium is lower than the free fall time scale. If we consider scales that are bigger than the Hubble radius  $r_H$ , pressure is not able oppose the gravitational collapse, thus the perturbation will evolve as described by the growing solution found in the previous Section.

In fact, let us now consider a small spherical overdensity embedded in a flat Universe; if the sorrounding matter does not affect the sphere, this can be described as a small Friedmann Universe with a density greater than the critical one, for example with  $k = 1$ . Defining  $\rho_0$  and  $a_0$  as the density and scale factor of the surrounding Universe and  $\rho_1$  and  $a_1$  as the density and scale factor of the perturbation, the Friedmann equations describing the two regions are

$$H_1 + \frac{1}{a_1^2} = \frac{8\pi G}{3}\rho_1, \quad (1.101)$$

$$H_0 = \frac{8\pi G}{3}\rho_0, \quad (1.102)$$

and, comparing the densities when the expansion rates are equal, we obtain

$$\frac{\rho_1 - \rho_0}{\rho} \equiv \frac{\delta\rho}{\rho_0} = \frac{3}{8\pi G\rho_0 a_1^2} \quad (1.103)$$

which becomes, if the perturbation is very small ( $a_1 \approx a_0$ ):

$$\delta \propto \frac{1}{\rho_0 a_0^2}. \quad (1.104)$$

Therefore, using the  $\rho$  and  $a$  of matter and radiation, we obtain again the two increasing solutions  $\delta_+$ .

We verified then, that a perturbation with a length scale bigger than the horizon will always grow, but every perturbation has a time  $t_{in}$  when it will enter the horizon, as the length scale decreases with the scale factor. Defining  $a_{eq}$  as the instant of equality between matter and radiation, length scales lower than  $\lambda_{eq}$  will enter the horizon during the radiation epoch at

$$a_{ent} = a_{eq} \frac{\lambda}{\lambda_{eq}}. \quad (1.105)$$

We will not study in details the evolution of sub- and super-horizon perturbations, but it can be summarized as:

1. Before entering the horizon, all the perturbations grow as  $a^2$  during the radiation epoch. If a perturbation will enter the horizon after  $a_{eq}$  then it will have a super-horizon growth proportional to  $a$  during the matter epoch.
2. During the radiation epoch, the perturbations whose lengthscale is lower than the horizon scale will have a gravitational collapse strongly opposed by cosmic expansion; even those perturbations with  $\lambda < \lambda_J$  can grow at most as  $\ln(a)$ .
3. Since  $a = a_{eq}$ , dark matter becomes the dominant component and its perturbations can grow again proportionally to the scale factor. The barionic component instead will still be coupled with photons and its perturbations will not grow. In fact, until the recombination  $a = a_{ric}$ , perturbations in the photo-barionic fluid will oscillate and decrease in amplitude because of a damping effect.
4. Since the decoupling between photons and baryons, the latter will fall in the gravitational potential wells already produced by dark matter perturbations. From now on the matter component (baryons and dark matter) will be free to grow until the dark energy dominated epoch.

For further informations and detailed calculations we refer to [11, 12]

## Chapter 2

# Beyond the standard cosmological model

In the first Chapter we introduced the cosmological standard model and described how many cosmological observations agree with this model. Nevertheless, several theoretical issues are present; here we will not review all of them, but we will focus on the two *unknown* fluids needed to explain the observed evolution of the Universe after recombination. These two fluids, *Dark Matter* and *Dark Energy* are in fact needed to explain many cosmological and astrophysical observation and to account for the Universe total energy budget.

### 2.1 Dark Matter

As we explained in the first Chapter, it is possible to measure the values of cosmological parameters through cosmological observations as the  $\Omega_i$  parameters enter all expression for theoretical predictions. One of these parameters, the matter density  $\Omega_m$ , has been measured as  $\Omega_m \approx 0.25$  by many different observations, such as luminosity distance [13] and CMB anisotropies measures [6]. Nevertheless visible matter, that is present in stars and gas throughout Universe, is not enough to account for this value.

One possibility to explain this phenomenon is to suppose the existence of a different kind of matter that does not interact electromagnetically, and thus is not visible, but whose gravitational interaction can account for the total matter density of the Universe; this new kind of matter is called *Dark Matter*.

As said above it is not possible to directly observe Dark Matter, but we can find signatures of its presence in astrophysical observations through gravitational effects. The first evidence of Dark Matter was provided by observations of galaxy clusters, in particular by measures of their mass  $M_c$ ; as an example, it is possible to measure the Mass of the Coma cluster, containing hundreds of galaxies, measuring its total luminosity. It is possible to convert the luminosity into mass through the mass-luminosity ratio obtaining  $M_c = 3 \cdot 10^{13} M_\odot$ . The cluster's mass can also be estimated through dynamical considerations; the cluster can be considered as a self gravitating system in a stationary state and, therefore, it is possible to use the Virial Theorem

$$K + 2W = 0, \tag{2.1}$$

where  $K$  and  $W$  are the kinetic and gravitational energy of the system. From this relation we obtain

$$K = -\frac{W}{2} \Rightarrow \frac{1}{2}M_c\langle v^2 \rangle = \frac{\alpha}{2} \frac{GM_c^2}{r_h}, \quad (2.2)$$

where  $\alpha$  is a parameter connected to the cluster luminosity profile,  $\langle v^2 \rangle$  is the mean square velocity and  $r_h$  is the radius of a sphere with the same center of the cluster and containing half of its mass.  $\langle v^2 \rangle$  can be measured through the squared radial velocity dispersion  $\sigma_r^2$ , while  $r_h$  can be obtained from the cluster profile, thus obtaining

$$M_c \approx 2 \cdot 10^{15} M_\odot. \quad (2.3)$$

Therefore almost all the cluster's matter is not in the form of visible matter (stars and gas), but it is in the form of Dark Matter that completely determines the dynamical properties.

Another signature of Dark Matter can be observed in galaxy rotation curves; stars orbit the galactic center because of a gravitational acceleration that depends on distance. This acceleration can be expressed, assuming that matter is spherically distributed, as

$$a = \frac{GM(r)}{r^2}, \quad (2.4)$$

where  $M(r)$  is the mass contained up to distance  $r$ . Expressing the acceleration as  $a = v^2/r$ , we can relate star velocities to the mass contained within their distance  $r$  from the galactic center:

$$v = \sqrt{\frac{GM(r)}{r}}. \quad (2.5)$$

In a spherical system  $M(r) \propto r^3$  and, therefore, we can compute how velocity vary with distance from center:

$$v \propto r. \quad (2.6)$$

However star distribution is connected with the luminosity profile of the galaxy that, typically, behaves as

$$I(r) = I_0 e^{\frac{r}{r_s}} \quad (2.7)$$

where  $r_s$  is a characteristic radius, typically of a few  $Kpc$ , that contains most of the galaxy mass. Therefore, at first approximation, stars that are at larger distances ( $r > r_s$ ) will all be attracted by the same mass, thus the velocity will decrease with radius as

$$v \propto \frac{1}{\sqrt{r}}. \quad (2.8)$$

However, the observed galaxy rotation curves (see Fig.2.1) show this behaviour only for  $r \approx r_s$ , while for larger radii, stars velocities take a constant value.

This phenomenon can be explained if galaxies are embedded in a Dark Matter halo as this invisible matter can provide mass outside  $r_s$  and produce the observed velocity trend.

However this Dark Matter can not be ordinary matter, or *baryonic matter* as it is known in cosmology, that is cold enough to be not observable. In fact, the ratio between the numerical densities of baryons and photons is tightly constrained [9]:

$$\eta = (5.5 \pm 0.05) \cdot 10^{-10}. \quad (2.9)$$

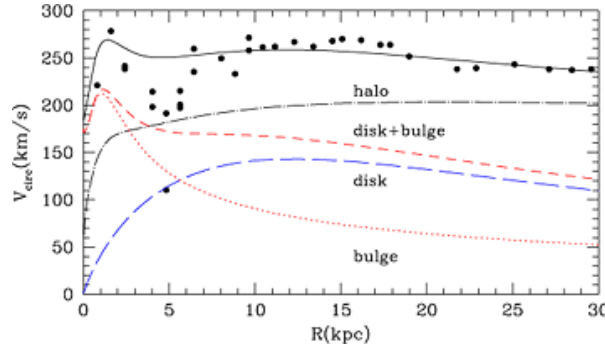


**Figure 2.1.** Observed rotation curve for M31 galaxy and theoretical models with and without the inclusion of a dark matter halo [14]

As this value is connected to the baryons numerical density, we can use it to determine the total contribution of baryons ( $\Omega_b$ ) to the energy density of non relativistic matter:

$$\eta = 2.74 \cdot 10^{-8} \left( \frac{2.73 \text{ K}}{T} \right)^3 \Omega_b h^2. \quad (2.10)$$

Thus, measuring the values of  $\eta$  and of the reduced Hubble constant  $h_0 = H_0/100$ , we obtain [10]

$$\Omega_b = 0.04 \pm 0.01 \quad (2.11)$$

To obtain this value we used nucleosynthesis predictions that is in very good agreement with observational data. Moreover, the total matter energy density  $\Omega_m \approx 0.25$  is confirmed by many different observations. Therefore we must conclude that matter in the Universe is made up of non baryonic matter for almost 80% as  $\Omega_{dm} \approx 0.21$ .

## 2.2 Dark Energy

In the first Chapter we introduced the cosmological constant  $\Lambda$  alongside the other components, matter and radiation, suggesting that this component would introduce an accelerated phase in the expansion of the Universe. We now want to analyze in more details the evidences that prompt to introduce this component, whose existence can be only inferred indirectly through its effects on cosmological evolution, as it happens for Dark Matter. In order to find observables that can verify the existence of this component, we can study Friedmann equations, as the first one allows to calculate the age of the universe as a function of  $\Omega_i$  and to compare the predicted value with observations, while the second one allows to analyze the effect of an accelerated expansion on the luminosity distance and to compare the theoretical calculations with data.

An inferior limit to the age of the Universe can be placed dating the oldest known stars; these are the low metallicity stars that are inside globular clusters and, studying their evolution stage, the age of Universe must be [15]

$$t_u > 13.5 \pm 2 \text{ Gyr} \quad (2.12)$$

Now we want to calculate theoretically the time  $t_0$  from the *Big Bang* (when  $a = 0$ ) to present time; this will vary as a function of the cosmological parameters  $\Omega_i$ . If

we consider a flat Universe composed by matter only,  $\Omega_m = 1$ , the first Friedmann equation becomes

$$\left(\frac{H}{H_0}\right)^2 = \frac{1}{a^3} \implies \sqrt{a} da = H_0 dt \quad (2.13)$$

Integrating with  $0 < t < t_0$  and  $0 < a < 1$ , assuming  $h_0 = 0.7$ , we obtain

$$t_0 = \frac{2}{3} H_0^{-1} \approx 9.3 \text{ Gyr} \quad (2.14)$$

Therefore if matter is the only component of the universe, the predicted age is not in agreement with observational data. Considering a Universe composed only by radiation, we would obtain a lower age,  $t_0 = (2H_0)^{-1}$ , thus it is not possible to account for the observed age of the Universe with only matter and radiation.

Through the same procedure, it is possible to calculate the age of an empty Universe were all the energy density is brought by curvature or by a cosmological constant; in the first case  $t_0 = H_0^{-1}$ , while in the second  $t_0 = +\infty$  and there would be no Big Bang. Therefore these two components can be introduced in a model containing matter and radiation in order to increase the theoretical age of the Universe.

In fact, if we assume a flat Universe composed by matter and cosmological constant ( $\Omega_\Lambda = 1 - \Omega_m$ ),

$$t_0 = \frac{2}{3} \frac{H_0^{-1}}{\sqrt{1 - \Omega_m}} \ln \left[ \frac{\sqrt{1 - \Omega_m} + 1}{\sqrt{\Omega_m}} \right], \quad (2.15)$$

and, choosing  $\Omega_m = 0.25$  and  $h_0 = 0.7$ , we obtain

$$t_0 \approx 14.2 \text{ Gyr}. \quad (2.16)$$

Therefore a model with matter and cosmological constant, whose energy densities are comparable, is in agreement with the inferior age limit obtained with globular clusters.

An even more crucial signature of dark energy is the observed deviation from the luminosity distance calculated with only matter and radiation. As we said previously, the Hubble law  $d_L = czH_0^{-1}$  is only valid if  $z \ll 1$ , while for larger redshifts we have to take into account higher orders in Eq.(1.50); these departures from Hubble law will give a lot of information on the Universe composition as they are connected with the deceleration parameter  $q_0$ , which is, in turn, linked to cosmological parameters by Eq.(1.42).

It is therefore possible to compare observational data with theoretical models produced with different values of  $q_0$ . As we can see from Fig.2.2, supernova data agree with a negative  $q_0$ ; this means that the Universe is now in an accelerated expansion phase that can not be explained by matter and radiation. In fact, these two components contribute in a positive way to the deceleration parameter; therefore, we need a dark energy fluid able to bring a negative contribution to  $q_0$  such as, for example, a cosmological constant.

### 2.2.1 The cosmological constant

A good candidate to explain this accelerated expansion phase is the Cosmological Constant. In fact as we said above, the equation of state parameter for this

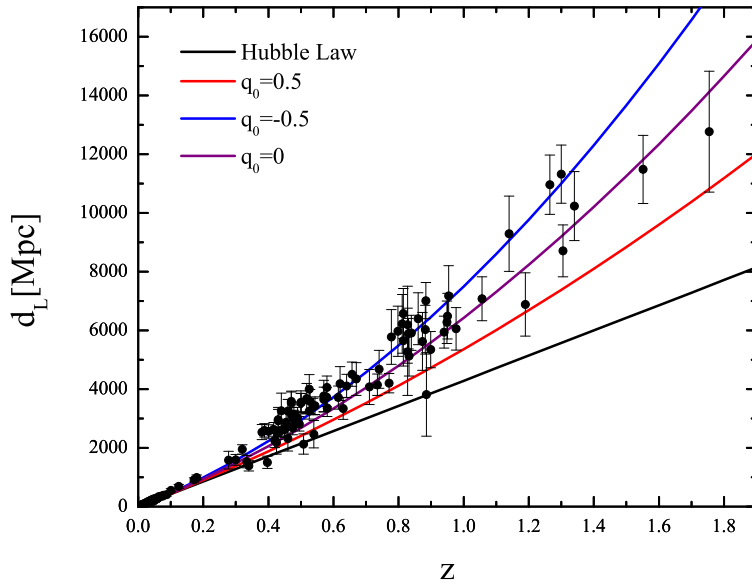


**Figure 2.2.** Luminosity distance with  $q_0 = 0.5$  (red line),  $q_0 = 0$  (purple line) and  $q_0 = -0.5$  (blue line). The black line is the low redshift Hubble law. Dots and error bars are SNIa data obtained by [13]

component is  $w = -1$  and this brings to a negative contribution to  $q_0$ :

$$q_0 = \frac{\Omega_m}{2} + \Omega_r - \Omega_\Lambda. \quad (2.17)$$

Therefore it is possible to constrain  $\Omega_\Lambda$  using luminosity distance data that, as we saw previously, are particularly sensitive to dark energy. In Fig.2.3 we can see constraints on  $\Omega_\Lambda$  and  $\Omega_m$  from the *Union2* supernova compilation [16]; the value of energy density arising from cosmological constant is constrained to be non vanishing in order to account for luminosity distance observational data. As we can see, the constraints on  $\Omega_\Lambda$  become tighter if other probes are considered, as both CMB and *Baryon Acoustic Oscillations* (BAO) are both sensitive to Dark Energy, as we will later see in detail.

Nevertheless, the cosmological constant suffers a few theoretical problems, mainly the *coincidence* and *fine tuning* problems.

The first problem arise from the fact that the energy densities of matter and cosmological constant are comparable at present time, even if their ratio changes quickly with time:

$$\frac{\rho_\Lambda}{\rho_m} = a^3. \quad (2.18)$$

At past times in fact, matter energy density was strongly dominant with respect to the cosmological constant, for example at Planck time,  $t_p = \sqrt{\hbar G/c^5} = 5.3906 \times 10^{-44} s$  after the Big Bang, their ratio was  $\rho_\Lambda/\rho_m \approx 10^{-123}$ .

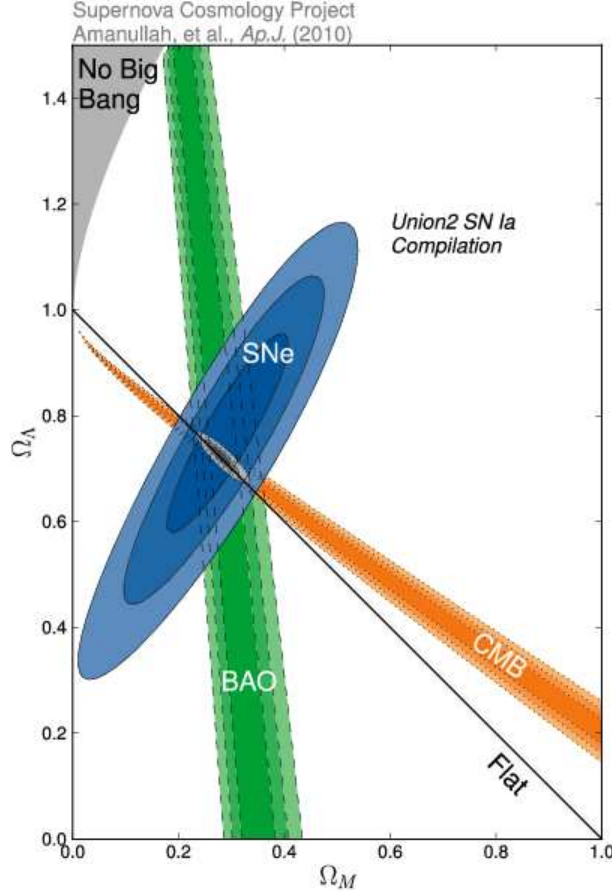


**Figure 2.3.** Observational constraints on  $\Omega_\Lambda$  and  $\Omega_m$ .

Knowing how the two components evolve with redshift, we can calculate the redshift  $z_T$  where the contributions of matter and cosmological constant were equivalent

$$(1 + z_T) = \left( \frac{\Omega_\Lambda}{\Omega_m} \right)^{\frac{1}{3}} \implies z_T \approx 0.3. \quad (2.19)$$

Thus, the equivalence happened really close to present time from the cosmological point of view, but there is no physical mechanism that can predict the transition from matter to cosmological constant, as the latter has a constant energy density. Therefore the value of the cosmological constant is exactly the one needed to switch at present time from the past matter dominance to the future cosmological constant prevailing, but there is no way to explain why we are living in such a special moment of the life of the Universe.

Another issue concerning the cosmological constant arises from its physical interpretation; this component in fact behaves like a fluid whose energy density keeps constant as the Universe expands, thus we can think that the cosmological constant is connected with vacuum energy which owns the same property.

It is possible to show that vacuum energy behaves like a cosmological constant, as taking the mean value of the stress-energy tensor on the vacuum state in Minkowski



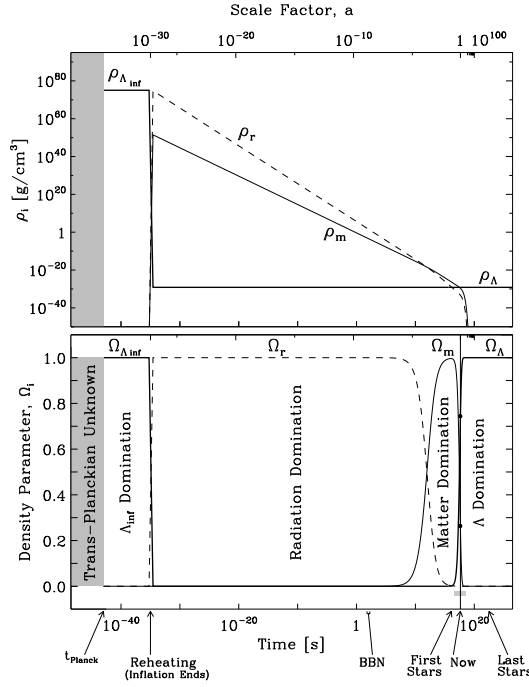


**Figure 2.4.** Plot illustrating the *coincidence* problem [17]

space-time, we obtain an invariant symmetric tensor, thus proportional to the metric. This apply also in curved space-time if we neglect higher order terms, therefore

$$\langle T_{\mu\nu} \rangle_{vac} = \rho_{vac} g_{\mu\nu}. \quad (2.20)$$

The effective cosmological constant which enters the Friedmann equations is given by [18]

$$\Lambda = 8\pi G \rho_{vac} + \Lambda_0 \quad (2.21)$$

where  $\Lambda_0$  is a constant.

We know that, as the Universe is flat ( $\rho_{tot} = \rho_c$ ), that  $\rho_\Lambda \equiv \Lambda/8\pi G$  cannot exceed the critical energy density

$$\rho_c = \frac{3H_0^2}{8\pi G} = 8 \cdot 10^{-47} h_0^2 \text{ GeV}^4. \quad (2.22)$$

We can calculate the vacuum energy using quantum field theory as

$$\langle T_{00} \rangle = \int_0^\infty \sqrt{k^2 + m^2} k dk = \infty, \quad (2.23)$$

therefore the theoretical vacuum energy must be normalized to a smaller, non-vanishing value.

Quantum field theory neglects the gravitational interaction, thus this theory will

apply only up to a cut off energy where gravity is no more negligible; this energy is given by *Planck mass* ( $M_P = \sqrt{\hbar c/G} = 2.1767 \cdot 10^{-8} \text{ kg}$ ) and we can use it as the cut off scale:

$$\rho_{vac} = \int_0^{M_P} \sqrt{k^2 + m^2} k dk \approx 10^{76} \text{ GeV}^4. \quad (2.24)$$

Therefore we can see how  $\rho_\Lambda$  and  $\rho_{vac}$  differs by many orders of magnitude,

$$\frac{\rho_\Lambda}{\rho_{vac}} \approx 10^{-123}. \quad (2.25)$$

Hence in order to explain the cosmological constant as a vacuum energy, we need to balance the term  $8\pi G \rho_{vac}$  tuning the value  $\Lambda_0$  in order to obtain a really small, but not vanishing, value of  $\Lambda$ .

### 2.2.2 Alternatives to the cosmological constant

These theoretical problems prompted cosmologists to find alternative models able to produce all the observational signatures of an accelerating Universe without the need of cosmological constant.

It's possible to replace the cosmological constant with an unknown component whose equation of state is  $P_x = w_x \rho_x$  and to calculate which values of  $w_x$  are able to produce a negative deceleration parameter  $q_0$ . In a Universe with  $\Omega_m \approx 0.25$  and  $\Omega_x \approx 0.75$  we have:

$$q_0 = \frac{1}{2}(1 + 3w_x)\Omega_x + \frac{\Omega_m}{2} \leq 0 \implies w_x \lesssim -\frac{1}{2} \quad (2.26)$$

The equation of state parameter  $w_x$  can be measured determining  $q_0$  through luminosity distance observations. This way is in fact possible to constrain  $w_x$  and therefore to both understand the equation of state of the unknown component and check if the cosmological constant  $w_x = -1$  agrees with observational data; current supernova observations [16], also combined with CMB and BAO data agree with a cosmological constant equation of state, but do not exclude values of  $w_x$  different from  $-1$ , as we can see in Fig.2.5.

The equation of state parameter of this new component can be also redshift dependent; in such a way the coincidence problem can be mitigated as the energy density of dark energy will now change with time. The redshift variation of  $w_x$  can be parameterized in many different way, such as

$$w_x(z) = w_0 + w_a z \quad (2.27)$$

if we assume a linear behaviour. Moreover, it's crucial to test the redshift dependence as detecting  $w_a \neq 0$  would rule out the cosmological constant model.

As we can see in Fig.2.6, the cosmological constant ( $w_0 = -1$  and  $w_a = 0$ ) is still in good agreement with data, but other possibilities are still plausible. For example is possible to modify the stress-energy tensor replacing the cosmological constant with a scalar field  $\phi$  and many different models can be constructed using different Lagrangians and exploiting various mechanisms to produce the accelerated phase (see [19] and [20]).

As an example we briefly discuss Quintessence models [21], i.e. models where alongside matter and radiation, an additional scalar field, minimally coupled with gravity,

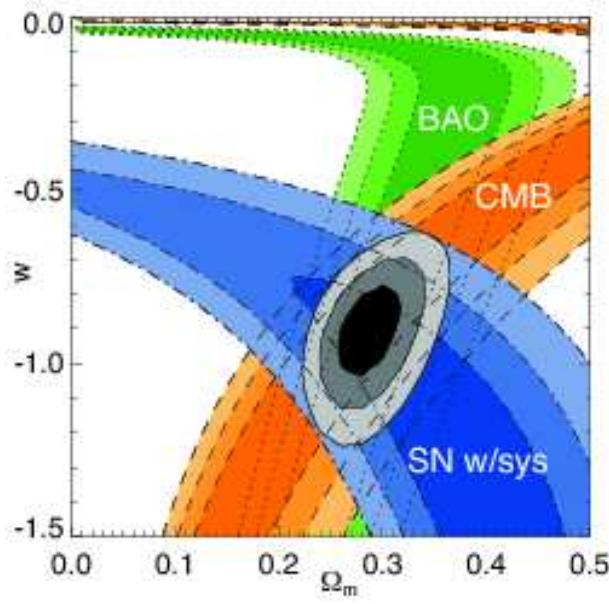


**Figure 2.5.** Constraints on  $w$  and  $\Omega_m$  from Union2 dataset, also in combination with CMB and BAO datasets. These results were taken from **sito Union**.

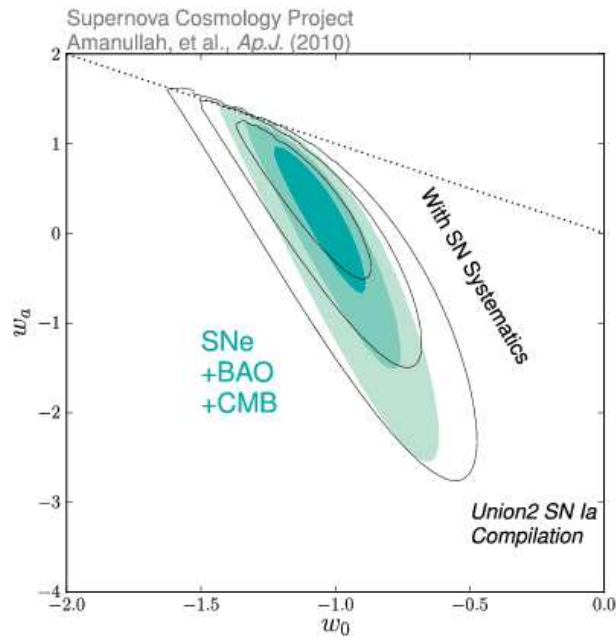


**Figure 2.6.** Constraints on  $w_0$  and  $w_a$  from Union2, CMB and BAO datasets.

is introduced. This fields have a redshift dependent equation of state similarly to matter and radiation fluids and this properties can, as previously said, mitigate the cosmological constant issues.

This new scalar field  $\phi$  is described by the action

$$S = \int d^4x \sqrt{-g} \left[ -\frac{1}{2} (g^{\mu\nu} \partial_\mu \phi \partial_\nu \phi)^2 - V(\phi) \right], \quad (2.28)$$

where  $V(\phi)$ , the field potential, will determine how the scalar field affects the expansion of the Universe.

In fact the contribution of the scalar field to the total stress-energy tensor is given by

$$T_{\mu\nu}^\phi = -\frac{2}{\sqrt{-g}} \frac{\delta S}{\delta g^{\mu\nu}} = \partial_\mu \phi \partial_\nu \phi - g_{\mu\nu} \left[ \frac{1}{2} g^{\alpha\beta} \partial_\alpha \phi \partial_\beta \phi + V(\phi) \right] \quad (2.29)$$

and, in the flat Friedmann metric, we can obtain the field's energy density and pressure:

$$\rho_\phi = T_0^0 = \frac{1}{2} \dot{\phi}^2 + V(\phi), \quad (2.30)$$

$$P_\phi = T_i^i = \frac{1}{2} \dot{\phi}^2 - V(\phi). \quad (2.31)$$

Thus, in a Universe composed only by this scalar field, the Friedmann equations become:

$$H^2 = \frac{8\pi G}{3} \left[ \frac{1}{2} \dot{\phi}^2 + V(\phi) \right], \quad (2.32)$$

$$\frac{\ddot{a}}{a} = -\frac{8\pi G}{3} \left[ \dot{\phi}^2 - V(\phi) \right]. \quad (2.33)$$

As we can see from Eq.(2.33), the field contributes in a negative way to the deceleration parameter if  $\dot{\phi}^2 < V(\phi)$ ; therefore, in order to explain the accelerated phase without a cosmological constant, the scalar field must be constructed in such a way to satisfy this condition.

In order to observationally test these models, it is useful to theoretically calculate the equation of state parameter

$$w_\phi = \frac{P_\phi}{\rho_\phi} = \frac{\frac{1}{2} \dot{\phi}^2 - V(\phi)}{\frac{1}{2} \dot{\phi}^2 + V(\phi)}, \quad (2.34)$$

if we assume a Universe whose energy density arises from  $\rho_k$ , where we account for matter and radiation, and  $\rho_\phi$ , the first Friedmann equation can be expressed as

$$\frac{8\pi G}{3} \rho_\phi(a) = H^2(a) [1 - Q(a)], \quad (2.35)$$

where  $Q(a)$  is defined as

$$Q(a) \equiv \frac{8\pi G \rho_k(a)}{3H^2(a)}. \quad (2.36)$$

Therefore, we can connect the equation of state parameters  $w_\phi$  to known quantities [22]:

$$w_\phi = -\frac{1}{3} \frac{d}{d \ln a} \ln \left[ (1 - Q) H^2 a^3 \right]. \quad (2.37)$$

Hence, theoretically, it is possible to obtain  $w_\phi$  by measuring  $H(a)$  and  $\rho_k(a)$ ; moreover, if  $H(a)$  is known, it is also possible to construct the field Lagrangian in such a way to reproduce the observed expansion history [22]:

$$\dot{\phi}^2(a) = \frac{3H^2(a)}{8\pi G} (1 - Q)(1 + w_\phi), \quad (2.38)$$

$$2V(a) = \frac{3H^2(a)}{8\pi G}(1-Q)(1-w_\phi). \quad (2.39)$$

A sub-class of quintessence models is the one of *tracker models*; these theories exhibit a particular evolution of the energy density  $\rho_\phi$  as it tracks the dominant component of the Universe. This way the coincidence problem is mitigated as the evolution of  $\rho_\phi$  is determined by the other components.

A potential that produces a field of this kind is [19]

$$V(\phi) = \frac{V_0}{\phi^\alpha}; \quad (2.40)$$

$\rho_\phi$  will be connected to the dominant background energy density  $\rho_B$  in such a way that  $\rho_\phi/\rho_B \propto t^{4/(2+\alpha)}$ , while the equation of state parameter will be

$$w_\phi = \frac{\alpha w_B - 2}{\alpha + 2}. \quad (2.41)$$

Applying to equations (2.34) and (2.41) the acceleration condition (2.26) we obtain:

$$\dot{\phi}^2 < \frac{2}{3}V(\phi) \quad (2.42)$$

$$\alpha < \frac{2}{2w_B + 1}. \quad (2.43)$$

Therefore, when the dominant component is matter,  $w_B = w_m = 0$  and the condition to obtain an accelerated expansion is  $\alpha < 2$ .

Nevertheless, the introduction of a new scalar field coupled with ordinary matter cause a fifth force [23]; in order to agree with experimental tests, the scalar field must have a very small mass,  $m_\phi \approx 10^{-33} \text{ eV}$ . However with such a small mass it is not simple to test the existence of this kind of scalar fields.

Many other models can be constructed with the introduction of scalar fields or with other modifications of the stress-energy tensor  $T_{\mu\nu}$ . However it is not in the purpose of this Thesis to describe them; further informations can be found in reviews such as [24] and [25].



## Chapter 3

# Extended Theories of Gravity

At the end of the previous Chapter we explained cosmological models able to produce an accelerated expansion phase without a cosmological constant and briefly described Quintessence models. These are part of *Modified Matter* theories, constructed modifying the right side of Einstein equations

$$G_{\mu\nu} = 8\pi GT_{\mu\nu} \implies 8\pi GT_{\mu\nu}^{mod}. \quad (3.1)$$

These models produce the acceleration introducing new energy components alongside matter and radiation in  $T_{\mu\nu}$ ; also the cosmological constant can be thought as a modified matter theory, as it can be thought as an addition to the stress-energy tensor:

$$G_{\mu\nu} = 8\pi GT_{\mu\nu} + \Lambda g_{\mu\nu} \implies 8\pi GT_{\mu\nu}^{mod}. \quad (3.2)$$

Nevertheless the cosmological constant can be also introduced as a modification to Einstein's General Relativity Lagrangian, thus it enters the equations as a modification of the Einstein tensor  $G_{\mu\nu}$ . Therefore another possible way to produce an accelerated expansion phase is to modify the gravity theory:

$$G_{\mu\nu}^{mod} = 8\pi GT_{\mu\nu}. \quad (3.3)$$

Theories that modify the Einstein tensor are known as *Extended Theories of Gravity* and at first they were formulated for completely different purpose; in fact the first modifications to General Relativity were proposed by Weyl in 1919 [26] and Eddington in 1923 [27], as they included higher order invariant terms in the Lagrangian in order to build a gravity theory alternative to the one formulated by Einstein.

During the 60s there were the first theoretical indications that a modification of Einstein's Lagrangian was needed; in these years, in fact, the quantum gravity problem was posed, that is the problem of how to combine gravity with the other forces (electromagnetic, weak and strong) described by quantum mechanics and field theory. One of the issues in this combination is that Einstein's theory is not renormalizable and, in order to mitigate this problem, it is possible to modify Einstein's Lagrangian including higher order of the Ricci scalar [28].

Nevertheless these modifications arise from quantum considerations and, therefore, the corrections must be important only at very high energies and curvature that is, from the cosmological point of view, during the first instants after the Big Bang. Instead, if we want to modify gravity in order to produce the cosmic acceleration

without a cosmological constant, we have to work on completely opposite energy scales, as the modifications have to be relevant at present time when energy and curvature are low.

Nevertheless it is possible to build modified gravity models motivated by quantum gravity theories; many of these assume the existence of additional dimensions and this idea was exploited by Dvali, Gabadadze and Porrati (DGP) [29] who proposed a 5 dimensional model where strong, weak and electromagnetic forces are confined to 4 dimensions, while gravity acts on 5 dimensions. In this DGP model, Newton gravity is recovered at small scales, while the effect of the fifth dimension is important at large scales leading to an acceleration of the Universe expansion, produced without the introduction of any additional component [30].

Other modified gravity models can be built replacing in the Lagrangian the Ricci scalar  $R$ , with other scalar quantities coming from the Ricci tensor  $R_{\mu\nu}$ ; a possible scalar is obtained by the Gauss-Bonnet combination

$$G \equiv R^2 - 4R_{\mu\nu}R^{\mu\nu} + R_{\mu\nu\alpha\beta}R^{\mu\nu\alpha\beta} \quad (3.4)$$

and can be used to build a Lagrangian leading to the present cosmic acceleration [31]

$$S = \int d^4x \sqrt{-g} \left[ \frac{1}{2}R - \frac{1}{2}(\nabla\phi)^2 - V(\phi) - f(\phi)G \right] + \int d^4x L_M, \quad (3.5)$$

where  $V(\phi)$  and  $f(\phi)$  are functions of a scalar field  $\phi$ .

Another class of modified gravity model is the one of scalar-tensor theories; these theories produce the cosmic acceleration through a coupling between the Ricci scalar  $R$  and a scalar field  $\varphi$ . The general action for scalar-tensor theories can be written as [32]

$$S = \int d^4x \sqrt{-g} \left[ \frac{1}{2}f(\varphi, R) - \frac{1}{2}\zeta(\varphi)(\nabla\varphi)^2 \right] + \int d^4x L_M(g_{\mu\nu}, \Psi_M), \quad (3.6)$$

where  $f$  depends on the scalar field  $\varphi$  and the Ricci scalar  $R$ ,  $\zeta$  is a function of  $\varphi$ . These and other modified gravity models are well described in the Review [33]

In this Thesis we will not describe deeply these models (useful details can be found in [32]), but we will focus on  $f(R)$ -gravity, a subclass of scalar-tensor theories obtained choosing  $f(\varphi, R) = f(R)$  and  $\zeta(\varphi) = 0$  in Eq.(3.6). Moreover we will study a general parameterization that allows to constraints deviation from standard General Relativity without the assumption of a theoretical model.

### 3.1 $f(R)$ -theories and the Hu and Sawicki model

One of the simplest ways to modify the General Relativity Lagrangian is to replace the Ricci scalar with a general function of itself, without the introduction of other scalar quantities:

$$S = \frac{1}{2k^2} \int d^4x \sqrt{-g} f(R), \quad (3.7)$$

where  $k^2 = 8\pi G$ . Theories with this kind of action are known as  $f(R)$  theories [34]. The choice to use higher orders of the scalar  $R$  instead of other scalar quantities (such as in Gauss-Bonnet theories) is mainly due to two reasons:



- $f(R)$  theories are general enough, in fact if we choose a power series

$$f(R) = \dots + \frac{\alpha_2}{R^2} + \frac{\alpha_1}{R} - 2\Lambda + R + \frac{R^2}{\beta_2} + \frac{R^3}{\beta_3} + \dots \quad (3.8)$$

where the  $\alpha_i$  and  $\beta_i$  coefficients have the appropriate dimensions, it is possible to introduce terms that affects gravity both at low and high curvature.

- **it is possible to show [35] that, given some conditions,  $f(R)$  theories are stable, while it is more difficult to achieve stability if other scalar quantities are introduced in the action.**

Using  $L = \sqrt{-g}f(R)$  as the new Lagrangian obviously affects the cosmic expansion as the Einstein equations in a void Universe now become

$$f_R R_{\mu\nu} - \frac{1}{2}f(R)g_{\mu\nu} - \nabla_\mu \nabla_\nu f_R + g_{\mu\nu} \square f_R = 0, \quad (3.9)$$

where  $f_R \equiv df/dR$  and  $\square \equiv g^{\mu\nu} \nabla_\mu \nabla_\nu$ . It is possible to show [36] that the modifications introduced with the new Lagrangian are physically equivalent to a theory where a scalar field is introduced in the standard Einstein-Hilbert Lagrangian<sup>1</sup>; we can in fact perform a *conformal transformation* of the metric [36, 38], where the new variables  $(p, \tilde{g}_{\mu\nu})$  are related to the old metric  $g_{\mu\nu}$  by

$$p = f_R, \quad \tilde{g}_{\mu\nu} = p g_{\mu\nu} \quad (3.10)$$

where we assume  $p > 0$  in such a way that  $\tilde{g}_{\mu\nu}$  does not change sign with respect to  $g_{\mu\nu}$ . Defining a scalar field  $\phi$  in such a way that  $p = \exp[\sqrt{2/3}\phi]$ , we obtain the Lagrangian in the *Einstein frame*, i.e. expressed with the standard dependence on the Ricci scalar and with the addition of a scalar field,

$$\tilde{L} = \sqrt{-\tilde{g}} \left[ \tilde{R} - \tilde{g}^{\mu\nu} \phi_{,\mu} \phi_{,\nu} - 2V(\phi) \right], \quad (3.11)$$

where the potential  $V$  depends on the function  $f(R)$  of Eq.(3.7), that is the action in the *Jordan frame*.

Gravity is therefore described by  $g_{\mu\nu}$  alone in the Jordan frame, while in the Einstein frame a scalar field appears; we didn't introduce any matter field yet, thus the scalar field must be interpreted as a non-metric property of the extended theory of gravity. We can therefore think of the  $f(R)$  theory in the Jordan frame as a “unified” theory that includes a non-metric degree of freedom that explicitly appears only in the Einstein frame. Therefore, if we have an “empty”  $f(R)$  theory, i.e. without any explicit matter field, it is not possible to choose which one of the two frames is the physical one. However if we include matter this ambiguity is lost as the two metrics  $g_{\mu\nu}$  and  $\tilde{g}_{\mu\nu}$  couple in different ways with the external fields and therefore produce different geodesic for test particles.

Another difference between the two frame lies also in the conserved quantities [36]:

<sup>1</sup>The physical equivalence between the scalar field and the  $f(R)$  Lagrangians has been recently put in doubt for a specific  $f(R)$  model [37]. Therefore there is a necessity to understand whether this is a particular model or if the two Lagrangians are only mathematically equivalent.

- The physical metric is  $g_{\mu\nu}$ .

In this case the Lagrangian for gravity and matter is

$$L = \sqrt{-g} [f(R) + 2L_m(\Psi, g)], \quad (3.12)$$

where  $\Psi$  represents the matter fields described by  $L_m$ . Through a variation of the action we obtain the field equations

$$f_R R_{\mu\nu} - \frac{1}{2}f(R)g_{\mu\nu} - \nabla_\mu \nabla_\nu f_R + g_{\mu\nu} \square f_R = T_{\mu\nu}(\Psi, g), \quad (3.13)$$

where  $T_{\mu\nu} = -2/\sqrt{-g} \delta/\delta g^{\mu\nu}(\sqrt{-g}L_m)$  and, because of the Bianchi identity,  $\nabla_\nu T^{\mu\nu} = 0$ . If we switch to the Einstein frame, the Lagrangian can be re-expressed as

$$\tilde{L} = \sqrt{-g} \left[ \tilde{R}(\tilde{g}) - \tilde{g}^{\mu\nu} \phi_{,\mu} \phi_{,\nu} - 2V(\phi) + 2e^{-2\sqrt{\frac{2}{3}}\phi} L_m \left( \Psi, e^{-\sqrt{\frac{2}{3}}\phi} \tilde{g} \right) \right], \quad (3.14)$$

that leads to the field equations

$$\tilde{G}_{\mu\nu} = t_{\mu\nu}(\phi, \tilde{g}) + e^{-\sqrt{\frac{2}{3}}\phi} T_{\mu\nu} \left( \Psi, e^{-\sqrt{\frac{2}{3}}\phi} \tilde{g} \right), \quad (3.15)$$

where  $\tilde{G}$  is the standard Einstein tensor computed in the metric  $\tilde{g}_{\mu\nu}$  and  $t_{\mu\nu}$ , the stress-energy tensor of the field  $\phi$ , is given by

$$t_{\mu\nu} = \phi_{,\mu} \phi_{,\nu} - \frac{1}{2} \tilde{g}_{\mu\nu} \tilde{g}^{\alpha\beta} \phi_{,\alpha} \phi_{,\beta} - V(\phi) \tilde{g}_{\mu\nu}. \quad (3.16)$$

The Bianchi identity becomes

$$\tilde{\nabla}^\nu \left[ t_{\mu\nu}(\phi, \tilde{g}) + e^{-\sqrt{\frac{2}{3}}\phi} T_{\mu\nu} \left( \Psi, e^{-\sqrt{\frac{2}{3}}\phi} \tilde{g} \right) \right] = 0 \quad (3.17)$$

and, therefore, the two stress-energy tensors are not conserved one by one in the Einstein frame.

- The physical metric is  $\tilde{g}_{\mu\nu}$

In this case, the field  $\phi$  is not coupled with matter because this time it is not a non-metric aspect of gravity. The Lagrangian in the Einstein frame is

$$\tilde{L} = \sqrt{-\tilde{g}} \left[ \tilde{R} - \tilde{g}^{\mu\nu} \phi_{,\mu} \phi_{,\nu} - 2V(\phi) + 2L_m(\Psi, \tilde{g}) \right], \quad (3.18)$$

leading to the field equations

$$\tilde{G}_{\mu\nu} = t_{\mu\nu}(\phi, \tilde{g}) + T_{\mu\nu}(\Psi, \tilde{g}) \quad (3.19)$$

$$\tilde{\square} \phi = \frac{dV}{d\phi} \quad (3.20)$$

$$\frac{\delta}{\delta \Psi} (L_m \sqrt{-g}) = 0 \quad (3.21)$$

and, as there is no interaction between matter and  $\phi$ , in this case the conserved quantities are the total stress-energy tensor  $t_{\mu\nu} + T_{\mu\nu}$  and the two tensors  $t_{\mu\nu}$  and  $T_{\mu\nu}$ .

In this Thesis we are interested in explaining everything that is not radiation or matter as a modification to gravity that drives the accelerated expansion of the Universe. Therefore we use the Jordan frame as the starting point to describe  $f(R)$  theories as in this frame all the additional components are unified in a modification of gravity.

### 3.1.1 Cosmological Viability

Introducing  $f(R)$  models we did not worry of their cosmological viability, but if we want to explain the present time accelerated expansion using these theories, we have to verify that the model we use produces an acceptable cosmological expansion.

What we want to do is to build an  $f(R)$  model able to produce an accelerated phase after the epochs of matter and radiation; however, many  $f(R)$  theories modify also the behaviour of the scale factor during the matter dominated epoch, when the cosmological constant model ( $a \propto t^{2/3}$ ) is in good agreement with the data. Therefore we need to find the conditions that the  $f(R)$  function must satisfy in order to produce a viable expansion history.

We define the parameters:

$$m(r) \equiv \frac{R f_{RR}}{f_R} \quad (3.22)$$

$$r \equiv -\frac{R f_R}{f} \quad (3.23)$$

where  $f_R = df/dR$  and  $f_{RR} = d^2f/dR^2$ . It is possible to show that for several  $f(R)$  theories, the following conditions apply [39]:

- a  $f(R)$  model has a standard matter epoch if

$$m(r) \approx 0 \text{ and } m'(r) > -1 \text{ when } r \approx -1 \quad (3.24)$$

where the second condition is needed in order to exit the matter epoch and start the accelerated phase.

- the matter epoch is followed by an accelerated phase where  $w_{eff}$ , the global equation of state parameter, goes asymptotically to  $-1$  when

$$0 \leq m(r) \leq 1 \text{ when } r = -2 \quad (3.25)$$

- the acceleration is non-phantom ( $w_{eff} \geq -1$ ) only if

$$m = -1 - r \quad (3.26)$$

Therefore, it is possible to visualize the viability of a model with a plot of  $m(r)$  parameter; in the fourth quadrant, this parameter must be between the  $r$  axis and the line  $-1 - r$ .

These conditions rule out many  $f(R)$  model, as the simple

$$f(R) = R - \alpha R^{-n}; \quad (3.27)$$

this model seem to have good properties, such as the importance of the modification at low curvatures. However, it is possible to show that during the matter epoch, the scale factor evolves as  $t^{1/2}$  instead of  $t^{2/3}$  [39]. If we calculate the  $m(r)$  parameter, we obtain

$$m(r) = -\frac{n(n+1)}{n + \frac{r-n}{r+n}} \quad (3.28)$$

and we can see in Fig.3.1 that the  $m(r)$  line is not inside the region between the  $r$  axis and the  $-1-r$  line in the fourth quadrant, therefore tis model must be discarded as it doesn't produce a viable cosmological expansion.

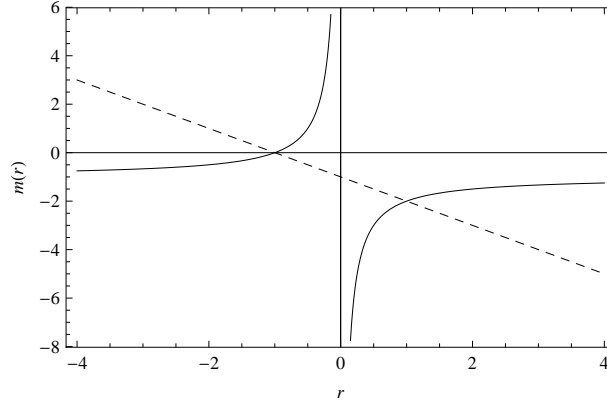


**Figure 3.1.** Plot of the  $m(r)$  parameter (solid line) and of  $-1-r$  (dashed line) for  $f(R) = R - R^{-n}$

### 3.1.2 The Hu and Sawicki model

We focus now on a particular  $f(R)$  model proposed by Hu and Sawicky (from now on HS) in 2007 [40]. We choose to analyze this model as it is viable both on cosmological and local scales. In fact, we will see further in this Section how the HS model satisfies the cosmological viability conditions previously introduced; moreover we will highlight that this model satisfies also solar system tests that usually constrain extended theory of gravity to be almost identical to General Relativity [40, 41, 42].

In the HS model, the modified gravity action is

$$S = \int d^4x \sqrt{-g} \left[ \frac{R + f(R)}{2k^2} + L_m \right], \quad (3.29)$$

where the function  $f(R)$  is chosen as

$$f(R) = -m^2 \frac{c_1 \left( \frac{R}{m^2} \right)^n}{1 + c_1 \left( \frac{R}{m^2} \right)^n}, \quad (3.30)$$

with  $m^2 = k^2 \bar{\rho}/3$ ,  $\bar{\rho}$  mean density of the Universe and  $c_1$  and  $c_2$  constants.

We can use the conditions explained above to check whether this model is cosmologically viable or not; calculating  $m(r)$ , with  $n = 1$  for simplicity, we obtain two solutions

$$m_1(r) = \frac{4(1+r)^2}{c_1 r^2 - \sqrt{c_1 r} \sqrt{4 + 4r + c_1 r^2}} \quad (3.31)$$

$$m_2(r) = \frac{4(1+r)^2}{c_1 r^2 + \sqrt{c_1 r} \sqrt{4 + 4r + c_1 r^2}} \quad (3.32)$$

As we will later see, the constants  $c_1$  and  $c_2$  are connected with the effective cosmological parameters  $\tilde{\Omega}_m$  and  $\tilde{\Omega}_x$  and choosing these as  $\tilde{\Omega}_m = 0.3$  and  $\tilde{\Omega}_x = 0.7$  we obtain the two solutions in Fig. 3.2. As we can see the solution  $m_2(r)$  is not acceptable, while  $m_1(r)$  is inside the allowed region.

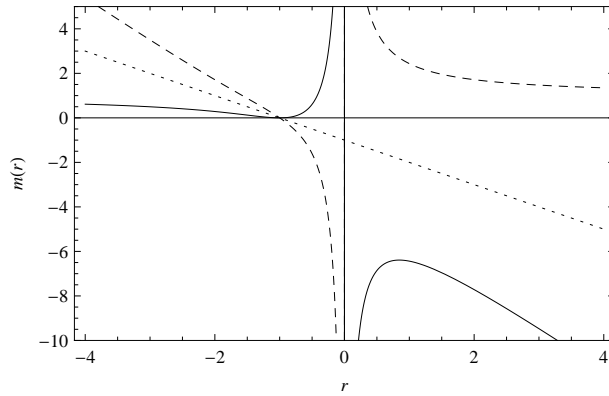


**Figure 3.2.** Plot of the  $m_1(r)$  parameter (solid line),  $m_2(r)$  (dashed line) and of  $-1 - r$  (dotted line) for the HS model.

The asymptotic  $m_1(r)$  behaviour for  $r \rightarrow \infty$  points out that the model evolves toward a cosmological constant acceleration ( $w = -1$ ) [39]; this seems to be in contrast with the  $f(R)$  function as we can see that

$$f(R) \rightarrow 0 \text{ when } R \rightarrow 0, \quad (3.33)$$

therefore the new Lagrangian would not become the cosmological constant one ( $L = \sqrt{-g}(R - \Lambda)$ ), but it will become the classical General Relativity Lagrangian ( $L = \sqrt{-g}R$ ). However, it is possible to show [40], that for viable values of  $c_1$  and  $c_2$  constants, the Ricci scalar  $R$  does not decrease indefinitely, but it rather freezes at a fixed value leading the model to become, asymptotically, similar to the cosmological constant one.

Therefore, the HS model is viable from the cosmological point of view, but we still have to check whether this model satisfies local gravity test. As we said above, in the Einstein frame all the modifications to gravity are encoded in a scalar field  $\phi$  which is coupled to matter, thus introducing a fifth force whose interaction range can be described with a Yukawa potential, therefore depending on the mass  $m_\phi$ ; as this force is not detected in solar system tests, we need to produce a range short enough to avoid our detection, thus the scalar field must be heavy enough. Nevertheless, the scalar field must affect the evolution of the Universe as a whole and therefore

the mass should be low in order to allow the modified force to act on the expansion. Some modified gravity models, such as the HS, solve this contrast thanks to the *Chameleon Mechanism* [43, 44] that produces a short range fifth force in dense environments, where tests are performed, while at cosmological density the mass of the scalar field becomes low.

The HS model exhibits this mechanism [40] and this allows to evade the solar system tests without tight constraints on the model parameters; in particular, solar system tests obtained in [45] can be passed by the HS model with the only constraint

$$|f_{R0}| \leq 0.1. \quad (3.34)$$

Therefore the HS model is viable both from the cosmological and local point of view; thus we can now study the Universe expansion that this theory produces starting from the action

$$S = \int d^4x \sqrt{-x} \left[ \frac{R + f(R)}{2k^2} + L_m \right]. \quad (3.35)$$

Varying this action we obtain the modified Einstein equations

$$G_{\mu\nu} + f_R R_{\mu\nu} - \left( \frac{f}{2} - \square f_R \right) g_{\mu\nu} - \nabla_\mu \nabla_\nu f_R = k^2 T_{\mu\nu}, \quad (3.36)$$

where the stress-energy tensor contains only matter contribution as radiation is negligible at low redshifts where modified gravity is supposed to be important. If we assume to be in a Friedmann metric we can write

$$R = 12H^2 + 6HH', \quad (3.37)$$

where  $H = H(\ln a)$  and  $' \equiv d/d \ln a$ ; replacing this in Eq.(3.36) we obtain the modified Friedmann equation

$$H^2 - f_R (HH' + H^2) + \frac{f}{6} + H^2 f_{RR} R' = \frac{k^2 \bar{\rho}}{3}. \quad (3.38)$$

It is useful to introduce the new variables

$$y_H \equiv \frac{H^2}{m^2} - a^{-3}, \quad (3.39)$$

$$y_R \equiv \frac{R}{m^2} - 3a^{-3}, \quad (3.40)$$

where  $m^2 = k^2 \bar{\rho}/3$ , obtaining the differential equation system

$$\begin{cases} y_H' = \frac{y_R}{3} - 4y_H \\ y_R' = 9a^{-3} - \frac{1}{y_H + a^3} \frac{1}{m^2 f_{RR}} \left[ y_H - f_R \left( \frac{y_R}{6} - y_H - \frac{1}{2a^3} \right) + \frac{f}{6m^2} \right] \end{cases} \quad (3.41)$$

Moreover, it is possible to encode all the modifications to the Friedmann equation in a virtual dark energy fluid  $\tilde{\rho}_x$  which will evolve as

$$\tilde{\rho}_x = \tilde{\rho}_x^0 e^{\int_a^1 \frac{3(1+w_x)}{a} da} \quad (3.42)$$

where  $w_x = w_x(a)$  is the equation of state parameter; therefore we can write the Friedmann equation in the standard form

$$\frac{H^2}{H_0^2} = \frac{\tilde{\Omega}_m}{a^3} + \tilde{\Omega}_x e^{\int_a^1 \frac{3(1+w)}{a} da}. \quad (3.43)$$

Using Eq.(3.39) and being  $m^2 = \tilde{\Omega}_m H_0^2$ , we obtain

$$y_H + a^{-3} = \frac{H^2}{m^2} = a^{-3} + \frac{\tilde{\Omega}_x}{\tilde{\Omega}_m} e^{\int_a^1 \frac{3(1+w)}{a} da} \implies y_H = \frac{\tilde{\Omega}_x}{\tilde{\Omega}_m} e^{\int_a^1 \frac{3(1+w)}{a} da}, \quad (3.44)$$

and, taking the logarithmic derivative of this equation with respect to the scale factor, we get

$$y'_H = -3(1 + w_x) \frac{\tilde{\Omega}_x}{\tilde{\Omega}_m} e^{\int_a^1 \frac{3(1+w)}{a} da}. \quad (3.45)$$

Therefore solving the differential equations of Eq.(3.41) we can obtain the equation of state parameter of the new dark energy fluid as

$$w_x = -1 - \frac{y'_H}{y_H}. \quad (3.46)$$

In order to solve the differential equation system, we need to express the  $c_1$  and  $c_2$  constant of Eq.(3.30) in terms of the real parameters of the theory, which are  $n$  and  $f_{R0}$ , the first derivative of the  $f(R)$  at present time; this is done in [40], obtaining

$$\frac{c_1}{c_2} \approx 6 \frac{\tilde{\Omega}_x}{\tilde{\Omega}_m}, \quad (3.47)$$

$$\frac{c_1}{c_2^2} \approx -\frac{\left(\frac{12}{\tilde{\Omega}_m} - 9\right)^{n+1}}{n} f_{R0}. \quad (3.48)$$

Therefore the only two parameters that control the theory are  $n$  and  $f_{R0}$  and, in order to solve the system, we now need only the initial conditions for  $y_H$  and  $y_R$ . These two variables, are defined in such a way to vanish in a pure matter phase. And we can consider as the starting point for this system an epoch which is matter dominated, but which contains a sub-dominant dark energy fluid. As we said previously, the  $\Lambda$ CDM model is in good agreement with observational data that refers to the pre-acceleration phase; therefore, we assume that our model in the matter dominated phase behaves like a cosmological constant. Thus, we can compute the initial Hubble parameter  $H_{in}$  from Eq.(3.43) using  $w_x = -1$

$$H_{in}^2 = m^2 \left( a^{-3} + \frac{\tilde{\Omega}_x}{\tilde{\Omega}_m} \right) \quad (3.49)$$

and, replacing this in Eq.(3.39), we obtain

$$y_H^{in} = \frac{\tilde{\Omega}_x}{\tilde{\Omega}_m}. \quad (3.50)$$

In order to obtain  $y_R^{in}$ , we need to use Eq.(3.37) and to define the logarithmic derivative of the Hubble parameter from Eq.(3.43)

$$2HH' = -3m^2a^{-3} \implies R_{in} = m^2 \left( 3a^{-3} + \frac{\tilde{\Omega}_x}{\tilde{\Omega}_m} \right) \quad (3.51)$$

and replacing this into Eq.(3.40) we obtain

$$y_R^{in} = 12 \frac{\tilde{\Omega}_x}{\tilde{\Omega}_m}. \quad (3.52)$$

We can now numerically solve the system and obtain  $y_H$  and  $y_R$ ; thus it is now possible to calculate the equation of state parameter ( $w_x$ ) of the virtual dark energy fluid which mimics the effects of gravity modifications.

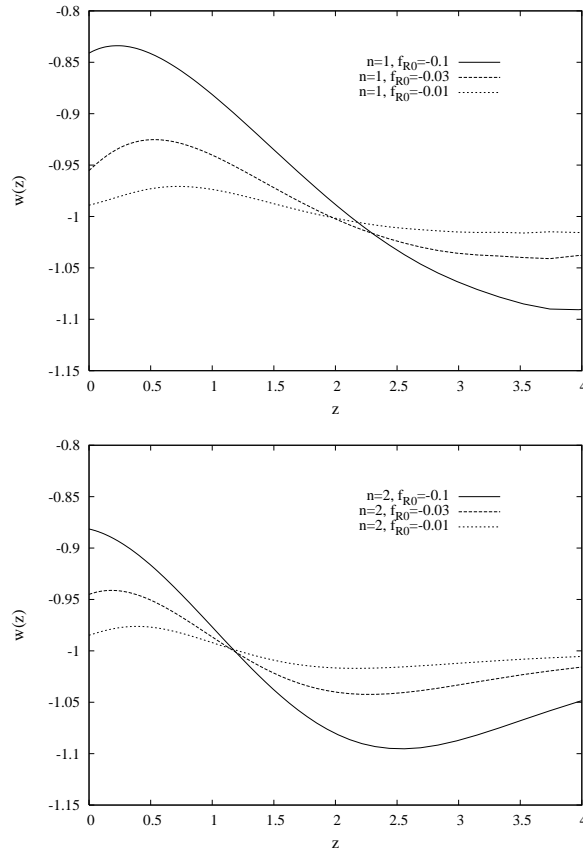


**Figure 3.3.** The equation of state parameter  $w$  for  $f_{R0} = -0.1, -0.03$  and  $-0.01$  (solid, dashed and dotted lines) with  $n = 1$  (top panel) and  $n = 2$  (bottom panel).  $\tilde{\Omega}_m$  is set to 0.24.

We can see in Fig.3.3 the peculiar trend of  $w_x$  as it starts from a value higher than  $-1$  when  $z = 0$  and decreases going into the *phantom region*  $w < -1$ . At higher redshifts it goes to the cosmological constant value of  $-1$ . this behaviour is the same for every value of  $n$  and  $f_{R0}$ ; raising the value of the first we can decrease the redshift value at which the phantom crossing happens, while decreasing the



absolute value of  $f_{R0}$  we decrease the difference between  $w_x$  and  $-1$ .

It is also useful to compute the growth of structure predicted by the HS model. We follow the method used in [46, 47] where linear perturbation of the flat Friedmann metric are considered in the *Newtonian gauge*

$$ds^2 = -(1 + 2\Psi) dt^2 + a^2(t) (1 - 2\Phi) d\vec{x}^2 \quad (3.53)$$

where the Newtonian potential  $\Psi$  and the perturbation to the spatial curvature  $\Phi$  are the perturbations to the metric. Since we are working in the Jordan frame, in which matter is minimally coupled, the conservation equations for the cold dark matter component have the same form than in General Relativity; thus at first order the conservation equations is

$$\dot{\delta} = -3\dot{\Phi} - \theta \quad (3.54)$$

$$\dot{\theta} = -H\theta + \left(\frac{k}{a}\right)^2 \Psi \quad (3.55)$$

where  $\dot{\phantom{x}} = d/dt$ ,  $\delta$  is the cold dark matter overdensity and  $\theta$  is the comoving dark matter peculiar velocity divergence. For sub-horizon modes ( $k > aH$ ) and in the quasi-static limit where time derivatives are negligible with respect to spatial ones, the  $0-0$  and  $i-j$  components of Einstein equations becomes

$$2\left(\frac{k}{a}\right)^2 \left[ \Phi(1 + f_R) - f_{RR} \left(\frac{k}{a}\right)^2 (\Psi + 2\Phi) \right] = -8\pi G \rho \delta \quad (3.56)$$

$$\Psi = -\left(\frac{1 - 2Q}{1 - Q}\right) \Phi \quad (3.57)$$

where the anisotropic stress of cold dark matter has been set to zero,  $\rho$  is the cold dark matter energy density, the radiation contribution has been neglected and the factor  $Q$  is defined as

$$Q(k, a) \equiv -2 \left(\frac{k}{a}\right)^2 \frac{f_{RR}}{1 + f_R}. \quad (3.58)$$

Combining Eq.(3.56) and Eq.(3.57) we obtain the modified Poisson equation

$$\Phi = \frac{8\pi G}{\left(\frac{k}{a}\right)^2 (1 + f_R)} \rho \delta \frac{1 - Q}{2 - 3Q} \quad (3.59)$$

which goes back to the standard one when  $f_R = 0$ . Combining now Eq.(3.54) and Eq.(3.59) we get the growth factor equation

$$\delta'' + \delta' \left( \frac{3}{a} + \frac{H'}{H} \right) - \frac{3\Omega_m a^{-3}}{\left(\frac{H}{H_0}\right)^2 (1 + f_R)} \frac{1 - 2Q}{2 - 3Q} \frac{\delta}{a^2} = 0 \quad (3.60)$$

where in this case  $' \equiv d/da$  and  $\delta$  is normalized in such a way that  $\delta \rightarrow a$  when  $a \rightarrow 0$ . In General Relativity, the factor  $Q$  given by Eq.(3.58) is zero and therefore the linear density growth is scale independent for all dark energy models. However, for  $f(R)$  models, the non-vanishing  $Q$  contains a scale dependence that is induced on  $\delta$ .

### 3.2 General Parameterization of Extended Theories of Gravity

In the last Section we introduced the HS model which is a particular model of the  $f(R)$  subclass of extended theories of gravity. In order to study these theories in a more general way, we would like to have the possibility to focus on theoretical prediction without having to specify the model we are using. This can be done introducing a parametrization encoding departures from General Relativity, as done in [48].

Taking the perturbed flat Friedmann metric in the conformal Newtonian gauge

$$ds^2 = -a^2(\eta) \left[ (1 + 2\Psi(\vec{x}, \eta)) d\eta^2 - (1 - 2\Phi(\vec{x}, \eta)) d\vec{x}^2 \right], \quad (3.61)$$

where  $\eta$  is the conformal time and  $\Psi$  and  $\Phi$  are the two potential describing the scalar metric perturbations; in the  $\Lambda$ CDM model, these two potentials are equal during the epoch of structure formation while this is not generally true in extended theories of gravity, where also the time dependency of these potentials is modified. In General Relativity, the Einstein equations provide two independent equations connecting these potential with matter perturbations, the Poisson and anisotropy equations:

$$k^2\Phi = -\frac{a^2}{2M_P^2}\rho\Delta, \quad (3.62)$$

$$k^2(\Phi - \Psi) = \frac{3a^2}{2M_P^2}(\rho + P)\sigma, \quad (3.63)$$

where  $\rho\Delta \equiv \rho\delta + 3aH/k(\rho + P)v$  is the comoving density perturbation and  $\sigma$ , the anisotropic stress, is connected to the traceless part of the stress-energy tensor.

In extended theories of gravity, as also in exotic dark energy models, the relations between potentials and matter perturbations can be different, thus we can parameterize the deviations from the General Relativity behaviour as [48]

$$k^2\Psi = -\frac{a^2}{2M_P^2}\mu(a, k)\rho\Delta, \quad (3.64)$$

$$\frac{\Phi}{\Psi} = \gamma(a, k), \quad (3.65)$$

where  $\mu(a, k)$  and  $\gamma(a, k)$  are two time and scale dependent functions encoding the gravity modifications. In order to have a useful parameterization, in [48] the authors express  $\mu$  and  $\gamma$  in such away to explicit the time and scale dependency:

$$\mu(a, k) = \frac{1 + \beta_1\lambda_1^2k^2a^s}{1 + \lambda_1^2k^2a^s} \quad (3.66)$$

$$\gamma(a, k) = \frac{1 + \beta_2\lambda_2^2k^2a^s}{1 + \lambda_2^2k^2a^s} \quad (3.67)$$

where the parameters  $\lambda_i^2$  have dimensions of length squared and are connected with the lengthscale of the modified force, the  $\beta_i$  represent dimensionless couplings with matter and  $s$  determines the time evolution of the theory.

In this parametrization, the background is fixed to that of the  $\Lambda$ CDM model of cosmology. The reasons for this choice are multiple; as we will later see in detail  $\Lambda$ CDM is currently the bestfit to available data and popular models of modified gravity, e.g.  $f(R)$ , closely mimic  $\Lambda$ CDM at the background level with differences which are typically smaller than the precision achievable with geometric tests [40]. The most significant departures happen at the level of growth of structure and, by restricting ourselves to  $\Lambda$ CDM backgrounds, we can isolate them.

Moreover as shown in [48], in the case of scalar-tensor theories the parameters  $\{\beta_i, \lambda_i^2\}$  are related in the following way

$$\beta_1 = \frac{\lambda_2^2}{\lambda_1^2} = 2 - \beta_2 \frac{\lambda_2^2}{\lambda_1^2} \quad (3.68)$$

and  $1 \lesssim s \lesssim 4$ . In the specific case of  $f(R)$  theories we can additionally reduce the number of free parameters. Indeed,  $f(R)$  theories correspond to a fixed coupling  $\beta_1 = 4/3$  [36]; moreover, models that closely mimic  $\Lambda$ CDM correspond to  $s \sim 4$  [48]. As pointed out in [49], the parametrisation in Eq.(3.66) effectively neglects a factor representing the rescaling of the Newton's constant already at the background level due to the modifications (e.g.  $(1+f_R)^{-1}$  in  $f(R)$  theories). Such a factor, calculated in [49], is very close to unity in models that satisfy local tests of gravity [40] and, as such, it can be neglected. However, when studying the  $f(R)$  case, we need to include it to get a more precise analysis.

Even with this extended parametrisation, we are left with a single free parameter, the lengthscale  $\lambda_1$ . Therefore it is possible to theoretically calculate the evolution of primordial perturbations produced by modified gravity without having to assume a specific model. In particular, a public code available at [50] and based on this parameterization allows to calculate the different CMB spectra produced by different combination of the modified gravity parameters. As we will see in the next Chapters, this will allow us to constrain modified gravity theory without having to assume a model, but only constraining the deviation produced with respect to General Relativity.

This is just one of many possible parameterization for extended theories of gravity. As an example  $f(R)$  theories can also be parameterized through the derivatives of the function of the Ricci scalar a parameterization that is used in *cosmography* [51].



## Chapter 4

# Observational signatures of Extended Theories of Gravity

As we explained in the previous Chapter, changing the laws of gravity on cosmological scales will affect both background observables, such as luminosity and angular distances through modifications of the equation of state parameter  $w$ , and observables connected with the evolution of perturbations through the modified Poisson and anisotropy equations.

In this Chapter we will focus on the observables that are useful to test extended theories of gravity. In particular we will introduce the astrophysical sources that are needed to calculate luminosity and angular distances thus allowing to test the background expansion produced by modified gravity models. Moreover we will explain how accurate measurements of the CMB and galaxies' distribution and gravitational lensing allow to test the evolution of density perturbations.

### 4.1 Background Observables

As we saw in the first Chapter, the expansion rate and acceleration is encoded in the behaviour of the scale factor  $a$  with time. This means that, in order to reconstruct the expansion of the Universe, we need to measure the luminosity and angular distances, which are connected to the scale factor. It would be also useful to measure the Hubble parameter  $H = \dot{a}/a$ , but as we will see this is a more complicated measurement.

#### 4.1.1 Standard Candles

First of all we want to measure the luminosity distance  $d_L$  as this can give us useful informations on the acceleration of the Universe; in fact, this quantity is connected to the deceleration parameter  $q_0$  through Eq.(1.50).

The luminosity distance can be obtained measuring the difference between the apparent and absolute magnitude of a given source, two quantities connected respectively to the observed and intrinsic luminosity;

$$\mu = m - M = 5 \log_{10}(d_L) + 25. \quad (4.1)$$

Therefore in order to obtain  $d_L$  we need to find astrophysical sources whose intrinsic luminosity and thus the absolute magnitude  $M$  is theoretically known; this kind of sources are known as *Standard Candles*.

Many variables stars can be used as standard candles, but for cosmological purposes the most useful are Supernovae<sup>1</sup>; these are *explosive variables*. i.e. stars whose observed luminosity raises suddenly, reaches a maximum and then decreases slowly, as we can see in Fig.4.1.

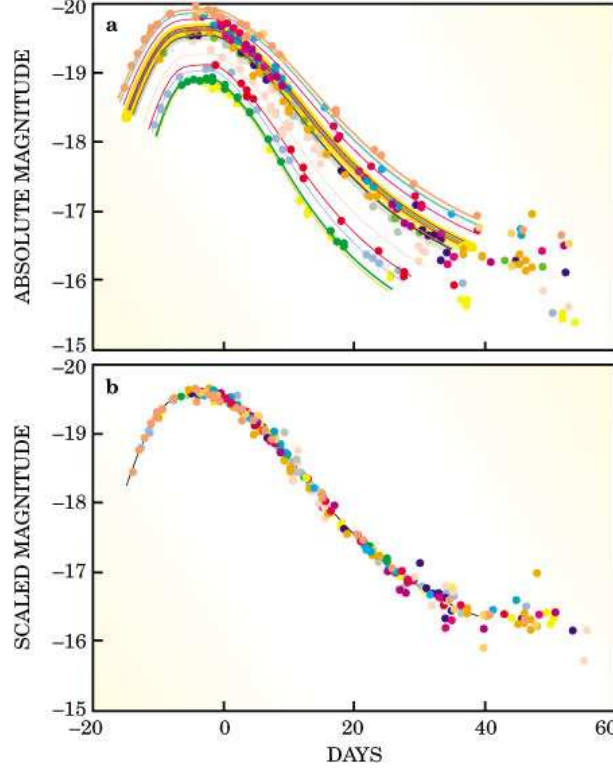


**Figure 4.1.** Plot of supernovae absolute magnitudes and of their reduced magnitude through Phillips law [53]

Supernovae observed luminosity can change of about 20 magnitude values, corresponding to energy emission of  $10^{49} - 10^{51}$  erg; this allows to detect this kind of stars at very big distances. Moreover it is possible to distinguish between two different kind of supernovae (SnI and SnII) studying the behaviour of luminosity with time (the *light curve*) and the emission spectrum. There is also a more refined classification of these two kind of supernovae, where we can identify the subclasses Ia, Ib, Ic from the differences in their emission spectra and in their light curves and the subclasses IIL and IIP, where the decrease of the light curve is linear (IIL) or exhibits a plateau (IIP).

The SnIa subclass is the one containing the most luminous supernovae and also the

<sup>1</sup>Another class of standard candles which recently are being used are Gamma Ray Bursts, very energetic bursts of gamma rays [52]. These GRBs are very useful as they can be detected at distances bigger than Supernovae, but the physical mechanism that produces this phenomenon is not yet understood, thus it is not sure if they can be used as standard candles.

most useful as standard candles. These in fact are the result of the explosion of a *white dwarf*, a star in an advanced phase of life that is a degenerate gas of electrons. This kind of stars can exist only if their mass does not exceed the Chandrasekhar mass  $M_C = 1.44 M_\odot$ ; therefore all the white dwarves that exist in the Universe are below that mass. If a white dwarf lives in a binary system with a less evolved companion star, when the youngest star evolves into a red giant, its mass can start to flow on the white dwarf and when this reaches  $M_C$  it explodes becoming a SnIa. Thus, all this SnIa explode starting from the same initial condition and therefore we can assume that the produced luminosity is always the same. From the spectroscopic point of view, SnIa are characterized by a strong absorption at  $615 \text{ nm}$  because of SiII and by strong absorption lines of CaII and MgII, while hydrogen lines are faint or totally absent as the white dwarf is a star that has already depleted all its hydrogen.

Thanks to the uniformity of SnIa light curves, it has been possible to calibrate the maximum intrinsic magnitude through cepheids, variable stars that allow to calculate the distance of nearby galaxies where the nearest SnIa can be observed. This way, the peak magnitude in the B band has been measured as  $M = -19.48 \pm 0.07$ . In order to obtain this calibration, it is necessary to remove some systematic effects such as the fading due to interstellar dust, possible gravitational lensing that can bring a magnification of the image and therefore an increase in the apparent magnitude and selection effects, as more luminous supernovae are detected more easily than the more faint, thus a mean magnitude calculated without corrections would be more brilliant than the real mean (Malmquist effect).

Nevertheless the error on the peak intrinsic magnitude is quite small allowing to use SnIa as standard candles.

When a SnIa is observed, we need to study the dependency of its luminosity on time to obtain the light curve; this curve allow us to calculate the apparent magnitude ( $m$ ) and, through the empirical *Phillips Law* [54], its absolute magnitude ( $M$ ); thus, through Eq.(4.1) we can obtain the luminosity distance  $d_L$ .

Moreover we need to acquire also the emission spectrum of the SnIa, which allows us, once we identified the absorption lines, to obtain the redshift  $z$  of the observed supernova. Therefore, with a survey of SnIa, we can sample the function  $d_L(z)$ , that as we saw previously allows us to obtain useful cosmological informations.

Currently the most sensitive SnIa catalogue is the Union2 survey [16], but future improved surveys, such as SNAP [55], are currently being proposed in order to improve the ability to constrain the expansion history of the Universe through this observable.

### 4.1.2 Standard Rulers

Previously we explained how the primordial plasma was composed by coupled baryons and photons, and we said that in this fluid there were inhomogeneities that in the end have evolved into the cosmological structures we see today; therefore the statistical properties of this inhomogeneities must be encoded in these structures (such as galaxies and clusters of galaxies).

As we described in Section (1.3), these inhomogeneities evolve through gravitational instability; in that Section we studied in detail the evolution of dark matter

perturbations, but baryons evolve in a different way. While dark matter behaves in a collisionless way, baryons, as we said interact with photons which produce a pressure; therefore in the photo-baryonic fluid acoustic waves are formed and their oscillations are freezed when photons decouple from baryons, thus at the Last Scattering Surface. This brings to the fact that a peculiar angular scale is imprinted in the temperature anisotropy of the CMB, corresponding to the sound horizon at recombination, while in galaxies distribution is possible to detect an *acoustic peak*, i.e. a preferred scale determined by the dimension of the horizon at the *drag epoch* when baryons' gravitational instability starts to dominate with respect to photon's pressure. These two scales can be detected observing the CMB and galaxies distribution and can be used as *standard rulers* as both of them are determined by linear perturbations physics; therefore, it is possible to calculate the true dimension of these scales and, through the observed dimensions, to reconstruct distances such as  $D_A$ .

### Baryon Acoustic Oscillations

As we previously said, in the photo-baryonic fluid, the competition between gravity and radiation pressure brings to oscillations in the fluid which propagate as sound waves, thus with a velocity  $c_s$  that can be calculated as

$$c_s = \frac{\delta p}{\delta \rho} \approx \frac{c^2 \delta \rho_\gamma / 3}{\delta \rho_\gamma \delta \rho_b} = \frac{c^2}{3(1 + R)} \quad (4.2)$$

where  $R \equiv 3\rho_b/4\rho_\gamma$ .

If we assume adiabatic initial conditions, when we have an overdensity in the primordial fluid, these will be the same for all the components of the fluid, thus photons, baryon, neutrinos and dark matter. While dark matter simply falls in the overdensity, radiation pressure makes the photo-baryon overdensity expands in order to balance density and pressure. Afterwards, when recombination starts, radiation pressure can not balance anymore the baryons' gravitational instability and the density profile of these will show a peak at the sound horizon scale during recombination ( $\sim 150 \text{ Mpc}$ ); when photons are completely decoupled, baryons will fall in the gravitational potential wells already formed by dark matter, but the combined distribution of baryons and dark matter will anyway show a bump at the sound horizon scale, and this can be detected through galaxies surveys.

This effect can be observed both as a bump in the *two point galaxy correlation function*  $\xi(r)$ , a quantity connected with the excess of galaxies at a given scale with respect to a mean distribution, and as oscillations (BAO) in the *matter power spectrum*  $P(k)$  which is the Fourier couple of  $\xi(r)$

$$P(k) = \int_{-\infty}^{+\infty} \xi(r) e^{-ikr} r^2 dr \quad (4.3)$$

Through these two functions it is theoretically possible to measure two different quantities corresponding to the oscillations parallel and perpendicular to the line of sight

$$\theta_s(z) = \frac{r_s(z_d)}{(1+z)D_A(z)} \quad (4.4)$$



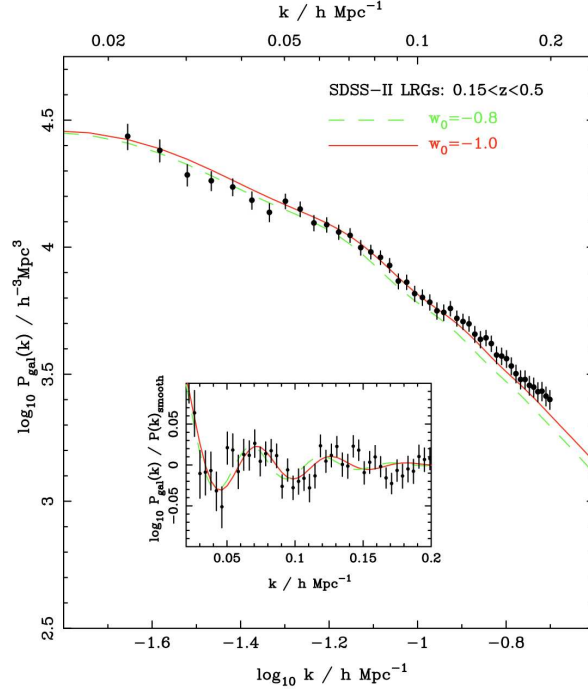


**Figure 4.2.** Baryon acoustic oscillations as can be seen through the galaxy power spectrum.

$$\delta z_s = \frac{r_s(z_d)H(z)}{c} \quad (4.5)$$

where  $r_s(z_d)$  is the sound horizon dimension at the drag epoch

$$r_s(z_d) = c \int_0^{t_d} \frac{c_s(t)dt}{a} = c \int_0^{a_d} \frac{c_s da}{a^2 H(a)}. \quad (4.6)$$

Nevertheless, current BAO data are not sensitive enough to allow a distinct measurement of these two quantities [56], but it is possible to measure a combination of the two

$$\left[ \theta_s(z)^2 \delta z_s \right]^{1/3} \equiv \frac{r_s(z_d)}{[(1+z)^2 D_A^2(z) c / H(z)]^{1/3}} \quad (4.7)$$

or an effective distance

$$D_V(z) \equiv \left[ (1+z)^2 D_A^2(z) \frac{cz}{H(z)} \right]^{1/3}. \quad (4.8)$$

Usually BAO measurements are given in terms of the relative distance

$$r_{BAO} \equiv \frac{r_s(z_d)}{D_V(z)}. \quad (4.9)$$

Currently two different measures of  $r_{BAO}$  are available, from the Sloan Digital Sky survey [57] and from the 2-Degree Field (2dF) Galaxy Redshift Survey [58].

As we will later see these measurements can be used to constrain the background expansion produced by modified gravity theories.

### Shift parameter

In the next Section, we will describe the CMB angular power spectrum, which has a behaviour that we can see in Fig.4.3

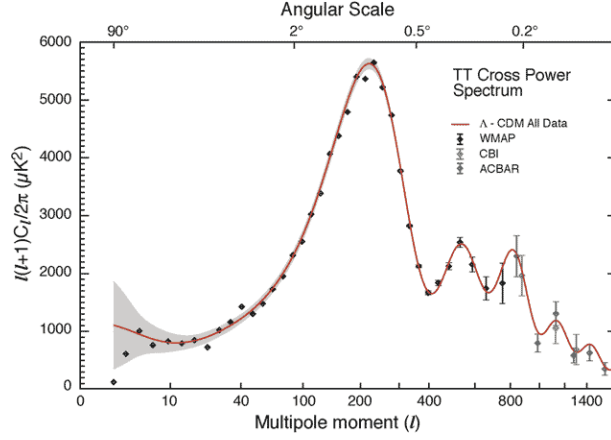


**Figure 4.3.** Angular power spectrum of temperature anisotropies as detected by WMAP [6]

As we will later see in detail, this power spectrum shows some acoustic peaks where the first one is dominant and it can be found at  $\theta_1 \approx 1$  corresponding to a multipole  $\ell_1 = \pi/\theta_1 \approx 220$ . As the comoving wavelength corresponding to the  $m$ -th peak can be expressed as  $\lambda_c = 2\pi/k = 2r_s(z_r)/m$  [59], where  $r_s(z_m)$  is the sound horizon dimension at recombination, it is possible to define a characteristic angle  $\theta_A$  connected with the position of the first peak

$$\theta_A \equiv \frac{r_s(z_r)}{d_A^c(z_r)}, \quad (4.10)$$

where  $d_A^c(z) \equiv (1+z)D_A(z)$  is the comoving angular distance. It is possible to connect a multipole  $\ell_A$  to the angle  $\theta_A$ , but it must pay attention to the fact that  $\ell_A$  is just approximately the multipole position of the first peak

$$\ell_A \equiv \frac{\pi}{\theta_A} = \pi \frac{d_A^c(z_r)}{r_s(z_r)}. \quad (4.11)$$

$\ell_A$ , also known as acoustic scale, can be used to obtain informations on the scale factor  $a$  as it depends on the angular distance  $D_A$  which is the integration of the expansion history of the Universe from  $z = 0$  to  $z = z_r$ , thus giving us an integrate information on the equation of state parameter  $w$  over this time range, while SNIa can only give us informations at recent times.

Nevertheless, in order to use  $\ell_A$  to constrain expansion models, it is useful to combine this with the *Shift parameter*  $R_{sh}$  that in a flat Universe can be expressed as [60]

$$R_{sh} = \sqrt{\Omega_m} \int_0^{z_r} \frac{dz}{E(z)}, \quad (4.12)$$

where  $E(z) \equiv H(z)/H_0$ , and Eq.(4.11) can be expressed as

$$\ell_A = \frac{\pi}{r_s(z_r)\sqrt{\Omega_m}}. \quad (4.13)$$

Therefore  $\ell_A$  is a combination of the shift parameter with the sound horizon at recombination, thus, in order to break the degeneracy and to obtain informations on the expansion history we need to measure both  $\ell_A$  and  $R_{sh}$  [61].

### 4.1.3 Hubble Parameter

As shown in [62] it is also possible to measure directly  $H(z)$  through the differential ages of *passively evolving galaxies*. This way it is possible to determine the expansion history of the Universe without having to assume a cosmological model as for standard rulers, or a particular astrophysical mechanism as for standard candles. Measuring  $H(z)$  in fact, as we can see in Fig.4.4, we are able to distinguish between the cosmological constant model and extended theories of gravity that modify the background expansion, such as the HS model.

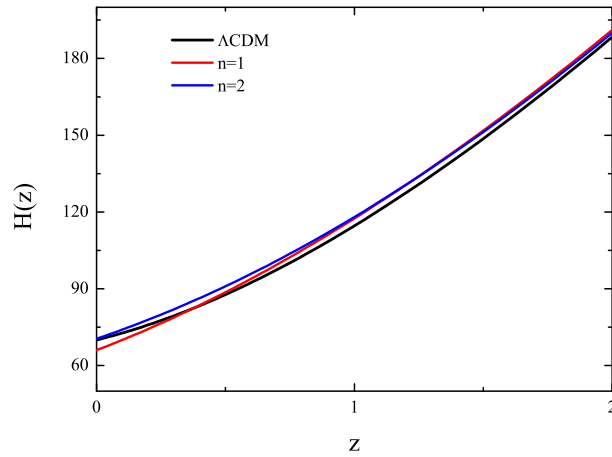


**Figure 4.4.**  $H(z)$  for  $\Lambda$ CDM model and for the HS model with  $f_{R_0} = -0.1$  and  $n = 1$  and  $n = 2$ .

$H(z)$  is connected to redshift as

$$H(z) \equiv \frac{\dot{a}}{a} = \frac{1}{1+z} \frac{dz}{dt}, \quad (4.14)$$

therefore if we can measure the variation of redshift with time for an astrophysical source, we obtain  $H(z)$ .

This can be done using galaxy surveys, firstly selecting galaxy samples of passively evolving galaxies with high-quality spectroscopy. Secondly, using synthetic stellar population models to constrain the age of the oldest stars in the galaxy [63], and then computing the differential ages, using them as an estimator for  $dz/dt$ , as explained in detail in [64] for the  $z = 0$  case.

## 4.2 Perturbations Observables

In the previous Chapter, we showed how extended theories of gravity do not change only the equation of state parameter and therefore the background expansion history of the Universe, but we explained that also the gravitational interactions are affected. Changing the gravitational Lagrangian in fact brings to a different Poisson equation and makes it possible to have an anisotropic stress different; thus, also the evolution of density perturbations will be modified with respect to the cosmological constant model. Therefore we need to find probes of these modifications that can allow us to constrain deviations from the General Relativity evolution of density perturbations.

### 4.2.1 CMB spectrum

As we explained in the first Chapter, matter density perturbations evolve with time, but dark matter and baryonic matter evolution is different, as the latter is tightly coupled with photons until recombination, when the Universe is no more ionized. At this point photons decouple from baryons and travel freely towards us from every directions; nevertheless these photons will keep memory of the anisotropies where they come from, as from the last scattering surface to us, they are affected only by secondary effects.

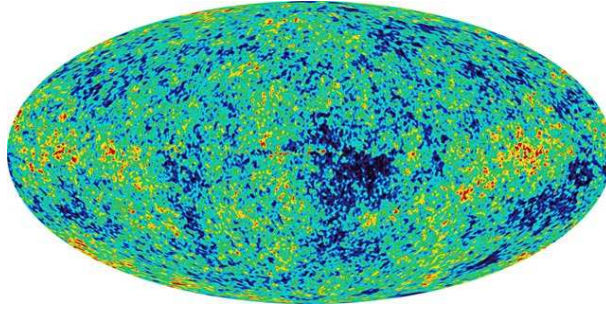


**Figure 4.5.** CMB map as reconstructed by WMAP [6]

It is possible to calculate [10] the evolution of the photo-baryonic fluid perturbations before recombination and therefore to calculate the temperature anisotropies  $\Theta \equiv (T - T_0)/T_0$  at the last scattering surface. Thus, observing these anisotropies in the CMB it is possible to understand how the Universe evolved before recombination.

In order to better describe temperature anisotropies it is useful to use spherical harmonics  $Y_{lm}(\hat{p})$

$$\Theta(\vec{x}, \eta, \hat{p}) = \sum_{\ell=1}^{\infty} \sum_{m=-\ell}^{\ell} a_{\ell m}(\vec{x}, \eta) Y_{\ell m}(\hat{p}) \quad (4.15)$$

where  $\hat{p}$  defines the direction in the sky  $(\theta_{sky}, \phi_{sky})$  and the coefficients  $a_{\ell m}(\vec{x}, \eta)$  contains all the informations about the temperature perturbations.

The monopole  $\ell = 0$  corresponds to the deviations from the mean temperature  $T_0$

all over the sky, thus,  $a_{00}$  vanishes by definition, while the dipole  $\ell = 1$  is dominated by the peculiar motion of the Earth with respect to the CMB [10]. Thus we can find cosmological information in the higher multipoles.

Thanks to the orthogonality of spherical harmonics

$$\int d\Omega Y_{\ell'm'}^*(\hat{p}) Y_{\ell m}(\hat{p}) = \delta_{\ell\ell'} \delta_{mm'}, \quad (4.16)$$

where  $Y^*$  is the complex conjugate of  $Y$  and  $d\Omega = d\cos\theta_{sky} d\phi_{sky}$ , we can obtain the equation for the coefficients

$$a_{\ell m}(\vec{x}, \eta) = \int \frac{d^3k}{(2\pi)^3} e^{i\vec{k}\cdot\vec{x}} \int_{\Omega=4\pi} d\Omega Y_{\ell m}^*(\hat{p}) \Theta(\vec{k}, \eta, \hat{p}) \quad (4.17)$$

Assuming that the perturbations arise from a gaussian distribution, as predicted by many simple primordial Universe models, we then expect that the ensemble average of the  $a_{\ell m}$  over many realizations of the universe is zero, and that all the information is contained in their variance, that can be expressed as

$$\langle a_{\ell m} a_{\ell' m'} \rangle = \delta_{\ell\ell'} \delta_{mm'} C_\ell \quad (4.18)$$

where the average is over infinite realizations of the Universe. However, as we can only observe one Universe, the ensemble average can be replaced, thanks to the ergodic principle, by an average over the directions of the sky, assuming that the statistical properties of the Universe are all the same in all the directions. This is equivalent, in multipole space, to an average over  $m$ , as all the  $a_{\ell m}$  are expected to have the same variance for each value of  $\ell$ , with  $-\ell < m < +\ell$ . Therefore we can build  $\hat{C}_\ell$ , an estimator of the real  $C_\ell$  as

$$\hat{C}_\ell = \frac{1}{2\ell + 1} \sum_{m=-\ell}^{+\ell} a_{\ell m}^* a_{\ell m}. \quad (4.19)$$

This estimator has a variance, called *cosmic variance*, intrinsic in the definition of the estimator itself and it changes with  $\ell$ , as low  $\ell$  have fewer  $m$  than high  $\ell$  ( $N(m) = 2\ell + 1$ )

$$\frac{\Delta C_\ell}{C_\ell} = \frac{\hat{C}_\ell - C_\ell}{C_\ell} = \sqrt{\frac{2}{2\ell + 1}} \quad (4.20)$$

Now we want to relate  $a_{\ell m}$  to the temperature anisotropies observed today  $\Theta_\ell(\vec{k}, \eta_0)$ ; considering that the temperature perturbation from a single plane wave can be decomposed as

$$\Theta(\vec{k}, \hat{p}, \eta) = \sum_\ell (-i)^\ell (2\ell + 1) \Theta_\ell(\vec{k}, \eta) P_\ell(\hat{p} \cdot \hat{k}), \quad (4.21)$$

where  $P_\ell$  is the Legendre polynomial, connected to the spherical harmonics as

$$P_\ell(\hat{k} \cdot \hat{p}) = \frac{4\pi}{2\ell + 1} \sum_{m=-\ell}^{\ell} Y_{\ell m}(\hat{p}) Y_{\ell m}^*(\hat{k}), \quad (4.22)$$

we can rewrite Eq.(4.17) as

$$a_{\ell m} = 4\pi \int \frac{d^3k}{(2\pi)^3} (-i)^\ell \Theta_\ell(\vec{k}, \eta) Y_{\ell m}^*(\hat{k}). \quad (4.23)$$

It is then possible to show [10] that the variance  $C_\ell = \langle a_{\ell m} a_{\ell' m'} \rangle$  can be related to the anisotropies observed today as

$$C_\ell = \frac{2}{\pi} \int_0^\infty dk k^2 P_\Phi(k, 0) \left| \frac{\Theta_\ell(k, \eta_0)}{\Phi_p(k)} \right|^2 \quad (4.24)$$

where  $\Phi_p$  is connected with the primordial perturbations and  $P_\Phi$  is the primordial power spectrum.

Therefore, measuring CMB temperature power spectrum it is possible to obtain informations on the primordial Universe and on how it evolved before recombination. Moreover CMB photons are also polarized and observing their polarization it is possible to extract more informations on Universe evolution. CMB photons are in fact polarized by temperature quadrupole that can be sourced both by scalar perturbations as well as by tensor perturbations from gravity waves produced by in primordial inflation [10]. Therefore it is possible to describe CMB polarization through *E modes* and *B modes*, distinguished by the polarization pattern around a considered point in the sky. As for temperature, cosmological informations can be obtained from polarization power spectra and also from their cross correlations; we can in fact define the following angular power spectra

$$\begin{aligned} C_\ell^{TT} &= \langle a_{\ell m}^{*T} a_{\ell m}^T \rangle \\ C_\ell^{EE} &= \langle a_{\ell m}^{*E} a_{\ell m}^E \rangle \\ C_\ell^{BB} &= \langle a_{\ell m}^{*B} a_{\ell m}^B \rangle \\ C_\ell^{TE} &= \langle a_{\ell m}^{*T} a_{\ell m}^E \rangle \\ C_\ell^{TB} &= \langle a_{\ell m}^{*T} a_{\ell m}^B \rangle \\ C_\ell^{EB} &= \langle a_{\ell m}^{*E} a_{\ell m}^B \rangle \end{aligned} \quad (4.25)$$

where the cross-correlations *TB* and *EB* are expected to vanish due to the fact that *B* has opposite parity to *T* and *E* and in Fig.4.6 we can see temperature and polarization power spectra as detected by WMAP satellite.

As we said before, primary CMB anisotropies are determined before the recombination phase, thus they bring informations about the primordial Universe. These primary anisotropies are imprinted in the CMB when photons decouple from baryons at redshift  $z \approx 10^3$ , about  $6000h^{-1}$  Mpc from us, and bring 3 different informations about the region where the considered photon had its last scattering, corresponding to the local gravitational potential  $\phi$ , the local peculiar velocity  $v_r$  and the local density fluctuation  $\delta$ . In fact, photons last scattered in a potential well ( $\phi < 0$ ) will be gravitationally redshifted and the same happens to photons last scattered by matter moving away from us ( $v_r > 0$ ). Moreover if a photon is coming from an overdense region ( $\delta > 0$ ) it will have an higher temperature as dense regions are intrinsically hotter.

Therefore the contribution given by primary anisotropies to the relative temperature difference can be written as [65]

$$\frac{\Delta T}{T}(\vec{r}) = \phi(\vec{r}) - \hat{r} \cdot \vec{v}(\vec{r}) + \frac{1}{3}\delta(\vec{r}) \quad (4.26)$$

where the length of the vector ( $\vec{r}$ ) is the comoving distance to the last scattering surface, i.e.  $r \approx 6000h^{-1}\text{Mpc}$ , and the fields  $\phi$ ,  $\vec{v}$  and  $\delta$  are to be evaluated at

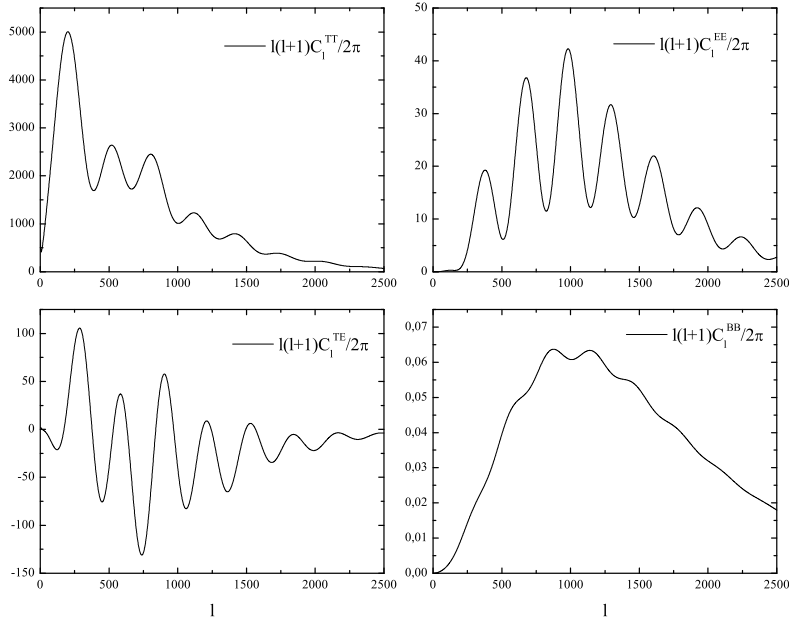


**Figure 4.6.** Plot of temperature and polarization power spectra. In this figure, the  $BB$  spectrum is the one produced by gravitational lensing of the CMB.

the time of recombination. The assumption of adiabatic initial conditions leads to a situation where the locations of the overdensities coincide with those of the potential wells, so that the third term partially cancels the first. On very large scales this leads to  $\delta \approx -2\phi$ , so that these two terms combine to  $\phi/3$  that is the *Sachs-Wolfe effect*, which is responsible for the flat part on the left side in Fig.4.3. On smaller scales, the fluctuations in  $\phi$ ,  $\vec{v}$  and  $\delta$  have time to undergo the acoustic oscillations that we introduced above, before recombination occurs, and this is responsible for the so-called Doppler peaks further to the right in Fig.4.3.

Moreover, since the last scattering surface is not infinitesimally thin, fluctuations on scales below that corresponding to its thickness, which corresponds to about  $\ell \approx 10^3$  ( $\theta \approx 0.1^\circ$ ), are suppressed as the CMB temperature that we measure in a given direction on the sky will in fact be a weighted average, corresponding to a mixture of photons coming from the near and far parts of the last scattering surface.

However, what we are looking for are signatures of extended theories of gravity that are important only at present time. Therefore we need to look at *secondary CMB anisotropies*, identifying the mechanisms that affect CMB anisotropies between the last scattering surface and us. In order to constrain modified gravity the physical mechanisms that interest us are mainly the *Integrated Sachs-Wolfe effect* (ISW) and the *CMB lensing*.

### Integrated Sachs-Wolfe effect

After recombination, photons are no longer interacting with matter through Thomson scattering, but only through gravity. The total sum of gravitational effects can be described [66] by a temporal variation of the potential that brings to the Integrated Sachs-Wolfe effect (ISW):

$$\frac{\Delta T}{T} = \int \dot{\phi}[r(t), T] dt, \quad (4.27)$$

where  $\dot{\phi}$  is the derivative of the gravitational potential with respect to conformal time  $d\tau = dt/a(t)$  at a given position  $r(t)$ .

When a photon enters a potential well it gains energy, and loses it when leaving. If the gravitational potential is static, the net energy balance is zero and the photon comes up with the same energy with which it is entered. But if, while crossing, the potential well changes ( $\dot{\phi} \neq 0$ ), the energy difference no longer vanishes, and the photon can be red or blue-shifted.

When the Universe is matter dominated, but the perturbations are still small enough to be handled as linear, the ISW effect vanishes; in fact, if we look at the Poisson equation

$$\nabla^2 \phi = 4\pi G a^2 \rho_b \delta, \quad (4.28)$$

where  $\rho_b \propto a^{-3}$  and  $\delta \propto a$ , we obtain

$$\nabla^2 \phi \propto a^2 a^{-3} a \propto \text{const.} \quad (4.29)$$

Nevertheless, there are three different situations when the ISW is different from zero. Right after recombination when the Universe is still not completely matter dominated, but there is still an effect given by radiation, the *Early ISW* takes place and as it affects scales of the order of the horizon at recombination, the early ISW produces a peak at  $\ell$  of the order of the first acoustic peak. Moreover, at  $z \ll z_{rec}$ , the photons can enter in a potential well that is growing non-linearly (for example, a galaxy proto-cluster), and it can come out with less energy than the input, and then they undergo a net redshift. If the potential is decreasing (as in a proto-void), there is a net blueshift. This effect, known as *Rees-Sciama effect*, is however much smaller than the primary anisotropies. Finally, still at  $z \ll z_{rec}$  the *Late ISW* takes place; this happens when the cosmological constants or other sources of accelerated expansion dominate. The late ISW affects large angular scales ( $\ell \rightarrow 0$ ) because it refers to the entire universe at low  $z$ .

It is through the late ISW that we can think to constrain extended theories of gravity; as we can see in Fig.4.7 changing the value of  $\lambda_1^2$  in the parameterization that we explained in the previous Chapter, modifies the part of the CMB spectrum affected by the late ISW with respect to the cosmological constant case.

Therefore this effect allow, in principle, to distinguish between the cosmological constant model and modified gravity theories, but as the late ISW falls in the part of the CMB spectrum that is mostly affected by cosmic variance, it is necessary, as we will explain in detail in the next Chapters, to cross-correlate CMB maps with galaxies surveys in order to obtain useful data.



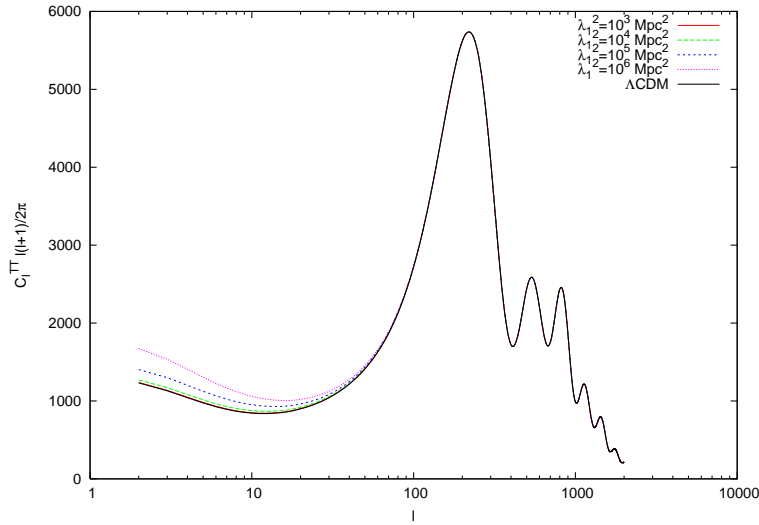


**Figure 4.7.**  $C_\ell^{TT}$  spectra for different values  $\lambda_1^2$

### CMB lensing

CMB photons are affected by gravitational lensing due to the matter that is placed between us and the last scattering surface; therefore CMB photons are deflected from their original positions and it is possible to reconstruct a lensed and an unlensed map of the CMB, as we can see in Fig.4.8

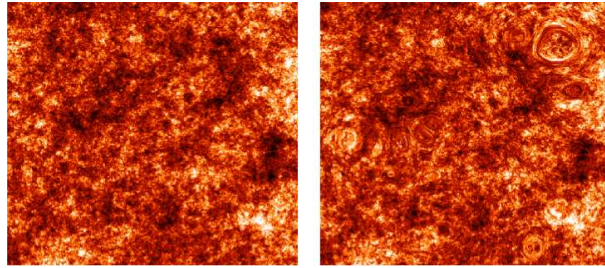


**Figure 4.8.** Distortion introduced by weak lensing on a CMB temperature patch. Taken from <http://www.mpia-hd.mpg.de/>, Max Planck Institute for Astronomy at Heidelberg.

Gravitational CMB lensing, as already shown in [67], can improve significantly the CMB constraints on several cosmological parameters, since it is strongly connected with the growth of perturbations and gravitational potentials at redshifts  $z < 1$  and, therefore, it can break important degeneracies.

Therefore, studying CMB lensing it is possible to reconstruct the evolution of matter perturbations after the last scattering surface; this evolution is changed by modifications of gravity, thus these theories leave an imprint on the lensing of the CMB photons. In particular we can see in Fig.4.9 how extended theories of gravity change the *CMB deflection power spectrum*.

The lensing deflection field  $d$  can be related to the lensing potential  $\phi$  as  $d = \nabla\phi$

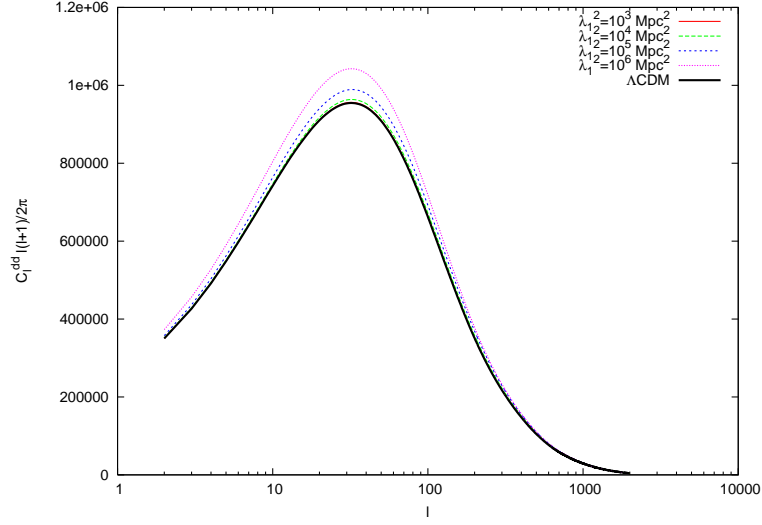


**Figure 4.9.**  $C_\ell^{dd}$  spectra for different values of  $\lambda_1^2$ .

[68]. In harmonic space, the deflection and lensing potential multipoles are related by

$$d_\ell^m = -i\sqrt{\ell(\ell+1)}\phi_\ell^m, \quad (4.30)$$

and therefore, the power spectra  $C_\ell^{dd} \equiv \langle d_\ell^m d_\ell^{m*} \rangle$  and  $C_\ell^{\phi\phi} \equiv \langle \phi_\ell^m \phi_\ell^{m*} \rangle$  are related through:

$$C_\ell^{dd} = \ell(\ell+1)C_\ell^{\phi\phi}. \quad (4.31)$$

Gravitational lensing introduces a correlation between different CMB multipoles (that otherwise would be fully uncorrelated) through the relation:

$$\langle a_\ell^m b_{\ell'}^{m'} \rangle = (-1)^m \delta_m^{m'} \delta_\ell^{\ell'} C_\ell^{ab} + \sum_{LM} \Xi_{\ell\ell'}^{mm'M} \phi_L^M, \quad (4.32)$$

where  $a$  and  $b$  are the  $T, E, B$  modes and  $\Xi$  is a linear combination of the unlensed power spectra  $\tilde{C}_\ell^{ab}$  (see [69] for details).

In order to obtain the deflection power spectrum from the observed  $C_\ell^{ab}$ , we have to invert Eq. (4.32), defining a quadratic estimator for the deflection field given by:

$$d(a, b)_L^M = n_L^{ab} \sum_{\ell\ell'mm'} W(a, b)_{\ell\ell'}^{mm'M} a_\ell^m b_{\ell'}^{m'}, \quad (4.33)$$

where  $n_L^{ab}$  is a normalization factor needed to construct an unbiased estimator ( $d(a, b)$  must satisfy Eq. (4.30)). This estimator has a variance:

$$\langle d(a, b)_L^{M*} d(a', b')_{L'}^{M'} \rangle \equiv \delta_L^{L'} \delta_M^{M'} (C_L^{dd} + N_L^{aa'bb'}) \quad (4.34)$$

that depends on the choice of the weighting factor  $W$  and leads to a noise  $N_L^{aa'bb'}$  on the deflection power spectrum  $C_L^{dd}$  obtained through this method. The choice of  $W$  affect the behaviour of lensing estimator and the reconstruction of the deflection power spectra and its noise starting from a given CMB map.

### 4.2.2 Weak Lensing

As we previously explained, reconstructing the evolution of matter perturbations allows to constrain modified gravity theories as these change the evolution of gravitational potentials during the expansion of the Universe. In order to reconstruct this evolution, it is useful to map the distribution of dark matter; this can be done exploiting the gravitational lensing that dark matter performs on distant light sources. The dark matter present in the Universe is in fact expected to lens by its gravity the image of far galaxies.

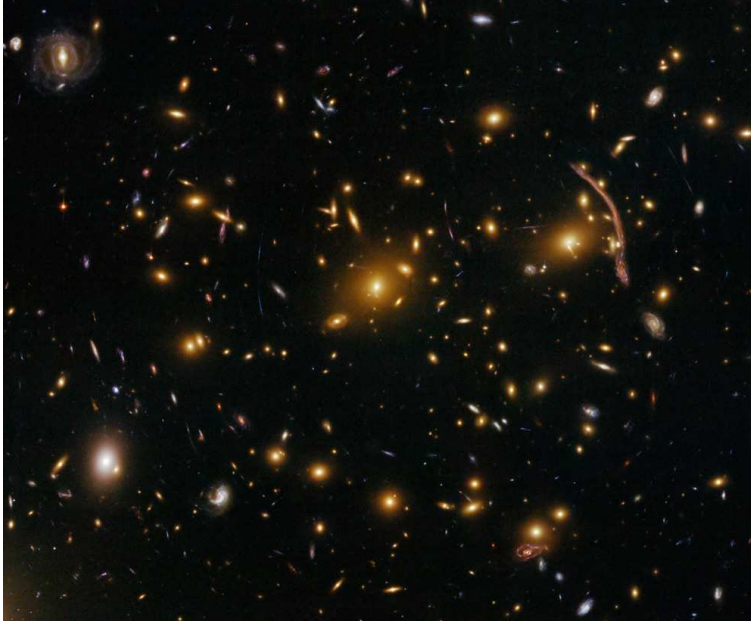


**Figure 4.10.** Image of galaxies distorted by gravitational lensing, taken by the Hubble Space Telescope

By reconstructing the distortion field, it is then possible to determine the dark matter distribution. Defining  $\theta_s$  and  $\theta$  as the angular position of the light ray in the source and lens plane respectively, we can write the *fundamental lensing equation* [70]

$$\alpha = \frac{D_S}{D_{LS}} (\theta - \theta_s) \quad (4.35)$$

where  $\alpha$  is the deflection angle and  $D_S$  and  $D_{LS}$  are respectively the angular diameter distances to the source plane and between the lens and source planes. We can handle the equation in the limit of small deflection angles as this is a common situation in the Universe and it is called the *weak lensing limit*. In this case Eq.(4.35) provides a one-to-one and invertible mapping between the source and lens plane. The effect of weak lensing is to distort the image of distant galaxy; this distortion can be described through the distortion tensor [71]

$$\psi_{ij} \equiv \frac{\partial \theta_s^i}{\partial \theta^j} - \delta_{ij} = \begin{pmatrix} -\kappa - \gamma_1 & -\gamma_2 \\ -\gamma_2 & -\kappa + \gamma_1 \end{pmatrix}, \quad (4.36)$$

where  $\psi_{ij}$  can be decomposed into a convergence term  $\kappa$  and two shear terms ( $\gamma_1$  and  $\gamma_2$ ). The convergence  $\kappa$  represents the magnification of the images, while the shear terms identify the stretching. Since both the convergence and the shear are due to the same gravitational potential, they can be related to each other, thus the cosmological information contained in  $(\gamma_1, \gamma_2)$  and  $\kappa$  is the same. It is sufficient hence to use only one observable, the convergence or the shear, to constrain cosmological parameters.

It is possible to express the convergence term as a weighted projection of the density fluctuation field  $\delta$  along the line of sight. As we assumed small deflection angles we can approximate the photon trajectory as a straight line, thus we can write

$$\kappa(\theta) = \int_0^{\chi_h} d\chi W(\chi) \delta(\chi, \theta), \quad (4.37)$$

where  $\chi = \int_0^z dz/H(z)$  is the radial distance and  $\chi_h$  the distance to the horizon. The weighting function  $W(\chi)$  is given by

$$W(\chi) = \frac{W_0}{\bar{n}_{gal}} \frac{\chi}{a(\chi)} \int_\chi^{\chi_h} d\chi' n_{gal}(\chi') \frac{\chi' - \chi}{\chi'}, \quad (4.38)$$

with  $W_0 = 3\Omega_m H_0^2/2$  and  $n_{gal}(\chi) = H(z)n_{gal}(z)$ , where  $n_{gal}(z)$  is the number of galaxies per redshift interval per steradian and it is normalized so that  $\int_0^\infty dz n_{gal}(z) = \bar{n}_{gal}$ .

the shape of the galaxy distribution can be parameterized as

$$n_{gal}(z) = \bar{n}_{gal} \frac{\beta}{z_0 \Gamma\left(\frac{1+\alpha}{\beta}\right)} \left(\frac{z}{z_0}\right)^\alpha e^{\left(\frac{z}{z_0}\right)^\beta} \quad (4.39)$$

where  $\alpha$ ,  $\beta$  and  $z_0$  are free parameters and they are chosen in order to reflect the observed galaxy redshift distribution of a given experiment, with  $z_0$  being generally a redshift close the median redshift of the survey.

Weak lensing it's a useful probe also because it allows to gain informations on the 3-dimensional distribution of dark matter through *tomographic* reconstruction of the density field [72]. This can be done dividing the galaxy distribution in redshift bins, thus Eq.(4.37) and Eq.(4.38) must be generalized for the generic  $i$ -th bin by replacing

$$\kappa(\theta) \rightarrow \kappa_i(\theta) \text{ and } W(\chi) \rightarrow W_i(\chi) \quad (4.40)$$

and the distribution of galaxies in every redshift bin is obtained binning Eq.(4.39)

$$n_{gal}(z) \rightarrow n_i(z) \text{ and } \bar{n}_{gal} \rightarrow \bar{n}_i \quad (4.41)$$

where  $\bar{n}_i = \int_0^\infty dz n_i(z)$  and  $\sum_i n_i(z) = n_{gal}(z)$ .

Since the lensing signal is generally small, in order to extract cosmological informations from weak lensing it is necessary to determine the statistical properties of the distortion field. The convergence term can be decomposed in the Fourier space:

$$\kappa_j(\theta) = \sum_\ell \tilde{\kappa}_\ell^j e^{i\ell\theta}. \quad (4.42)$$

Therefore it is then possible to define the cross angular power spectrum of the convergence at multipole  $\ell$  between the i-th and j-th tomographic bin as

$$\langle \tilde{\kappa}_\ell^i \tilde{\kappa}_\ell^{j*} \rangle = 4\pi^2 \delta_{\ell\ell'} C_\ell^{ij} \quad (4.43)$$

Since the typical correlation length is generally smaller than the window function used, it is possible to use the *Limber approximation* [73] that allow us to relate the convergence angular power spectrum and the three dimensional matter power spectrum  $P_m$  through the equation

$$C_\ell^{ij} = \int_0^{\chi_h} d\chi \frac{W_i(\chi) W_j(\chi)}{\chi^2} P_m \left( k = \frac{\ell}{\chi}, z \right), \quad (4.44)$$

where a flat Universe is assumed. The matter power spectrum  $P_m$  has to account also for the non linear growth of structure, since the  $C_\ell$  probes also small scales. It is possible to see that cosmological informations are contained in the convergence power spectra through  $W(\chi)$  and  $P_m$ ; introducing gravity modifications we change the evolution of Dark Matter perturbations and therefore the shape of the matter power spectrum. Thus, the convergence power spectrum will change in extended theories of gravity with respect to the one produced by a cosmological constant model, as we can see in Fig.4.12

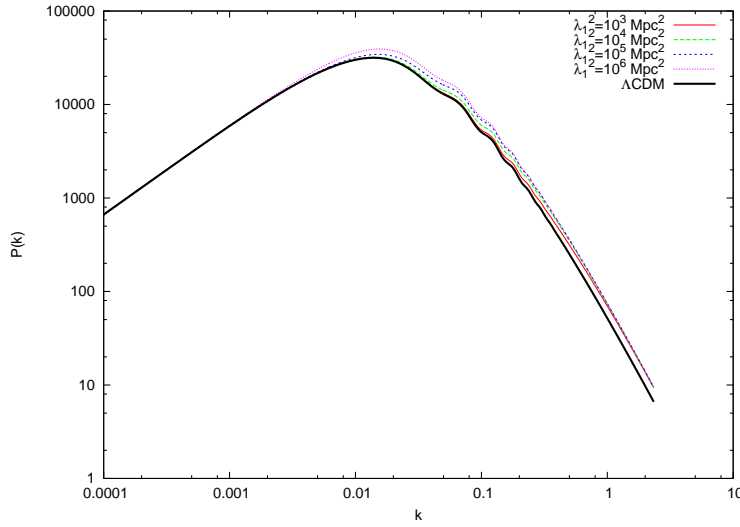


**Figure 4.11.** Matter power spectra  $P(k)$  for different values of  $\lambda_1^2$ .

Therefore, weak lensing is a very powerful probe to constrain extended theories of gravity as we will see further.

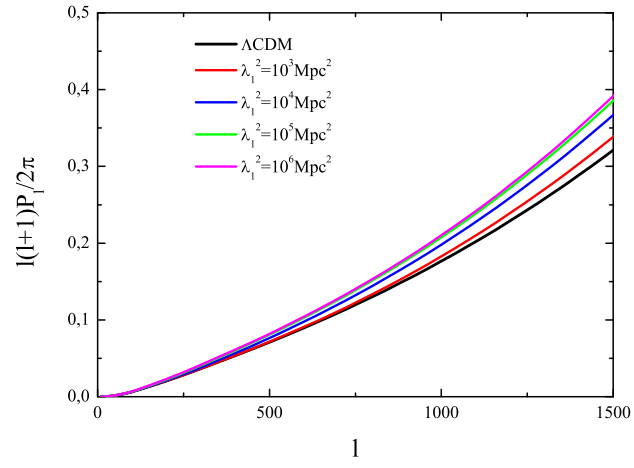


**Figure 4.12.** Convergence power spectra for different values of  $\lambda_1^2$ .

## Chapter 5

# Observational constraints on the Hu and Sawicki Model

In Chapter 3 we described the HS model as a viable gravity modification that can bring to an accelerated expansion without the introduction of a cosmological constant. This model modifies the equation of state parameter as we saw in Fig.3.3 and these modifications are related to the values of the two parameters of the theories  $f_{R0}$  and  $n$ .

As we previously explained,  $f_{R0}$  is constrained to be lower than 0 to have a stable model and to be higher than  $-0.1$  to satisfy solar system constraints, while  $n$  has to be larger than 0.

We want to constrain the values of these two parameters with cosmological data in such a way to restrict the allowed parameter space for this model and to study how much it differs from a cosmological constant, recovered for  $f_{R0} \rightarrow 0$ ,  $n \rightarrow \infty$  or  $f_{R0}$  and  $n$  that vanish at the same time.

### 5.1 Background constraints

As we previously explained, the HS model can be compared to the cosmological constant model through its effects on the expansion history of the Universe. Therefore background expansion observable can be used to constrain the allowed parameter space of the model; in [74] we calculate theoretically some observables for the HS model, such as the luminosity distance

$$d_L = \frac{1}{a} \int_a^1 \frac{da}{a^2 H(a)} = \frac{1}{aH_0} \int_a^1 \frac{da}{a^2 \sqrt{\tilde{\Omega}_m(y_H + a^{-3})}}, \quad (5.1)$$

the Hubble parameter

$$H(a) = \sqrt{\tilde{\Omega}_m H_0^2 (y_H + a^{-3})} \quad (5.2)$$

and the quantity

$$A \equiv \frac{\sqrt{\tilde{\Omega}_m}}{z_*} \left[ z_* \frac{\Gamma(z_*)}{\epsilon(z_*)} \right]^{\frac{1}{3}} \quad (5.3)$$

where  $z_* = 0.35$ ,  $\Gamma(z_*) = \int_0^{z_*} dz/\epsilon(z)$  and  $\epsilon(z) = H(z)/H_0$ . The value of this parameter can be obtained from observations of Baryon Acoustic Oscillations (BAO) [75]. Hence, we have another way to compare model prediction with data.

We used the supernova data from Kowalski et al. [76] to obtain the observational trend of  $d_L(z)$  and we considered  $H(z)$  values obtained by Simon, Verde and Jimenez [77] and a prior on the Hubble parameter  $H_0 = 0.72 \pm 0.08$  derived from measurements from the Hubble Space Telescope (HST, [78]), Finally, we used the value of  $A$  from Eisenstein et al. [79].

We compute a  $\chi^2$  variable for each observational quantity and then combine the results in a single variable  $\chi^2 = \chi_{SN}^2 + \chi_{BAO}^2 + \chi_H^2 + \chi_{HST}^2$ . Once the theoretical evolution of the observational quantities is defined, we can define a likelihood function as a function of  $n$  and  $f_{R_0}$  as

$$L = e^{-\frac{\chi^2 - \chi_{min}^2}{2}} \quad (5.4)$$

where  $\chi_{min}^2$  is the minimum value in the considered range of  $n$  and  $f_{R_0}$ .

Combining the results obtained from the comparison between the experimental data for  $H(z)$ ,  $A$  and  $d_L(z)$  and their theoretical values, we can constrain the free parameters  $n$  and  $f_{R_0}$  for different values of  $\tilde{\Omega}_m$  and  $\tilde{\Omega}_x$ .

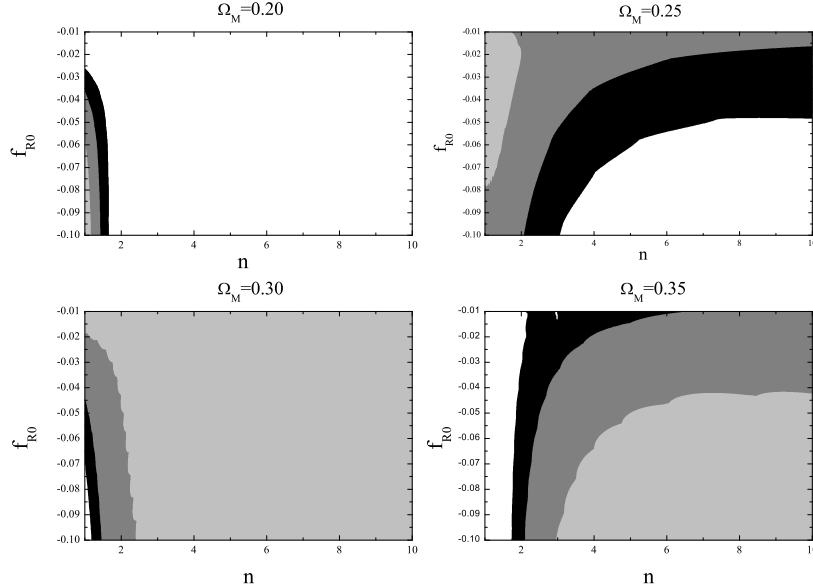


**Figure 5.1.** 68%, 95% and 99% confidence levels in the  $n$ - $f_{R_0}$  plane in function of different values of  $\tilde{\Omega}_m$ .

Setting  $\tilde{\Omega}_m = 0.2$  and  $\tilde{\Omega}_x = 0.8$ , a quite unrealistic Universe as we can see from Fig.2.3, it is possible to find an upper limit on  $n$  and on  $f_{R_0}$ ,  $n < 1.6$  and  $f_{R_0} < -0.03$  at  $2\sigma$ , while, performing the same analysis with different values of  $\tilde{\Omega}_m$



and  $\tilde{\Omega}_\Lambda$ , we can see that raising  $\tilde{\Omega}_m$  brings to more loosely constrained parameters. We can note anyway that for higher values of  $\tilde{\Omega}_m$ , higher  $n$  are preferred, while smaller values of  $n$  are more in agreement with data for smaller  $\tilde{\Omega}_m$ .

As we can see from Figure 5.1, for  $\tilde{\Omega}_m = 0.3$  both parameters are almost totally unconstrained; this points out the need of an independent measurement of the effective matter content ( $\tilde{\Omega}_m$ ) in order to obtain some constraints on  $n$  and  $f_{R_0}$ .

It is interesting to compare the best fit values of  $\chi^2$  obtained in the modified gravity framework with the  $\chi^2$  of a cosmological constant model. In order to quantify the goodness-of-fit of the two models we use the Akaike information criterion (AIC) [80] and the Bayesian information criterion (BIC) [81], defined as

$$AIC = -2 \ln L + 2k$$

$$BIC = -2 \ln L + k \ln N$$

where  $L$  is the maximum likelihood,  $k$  the number of parameters and  $N$  the number of points.

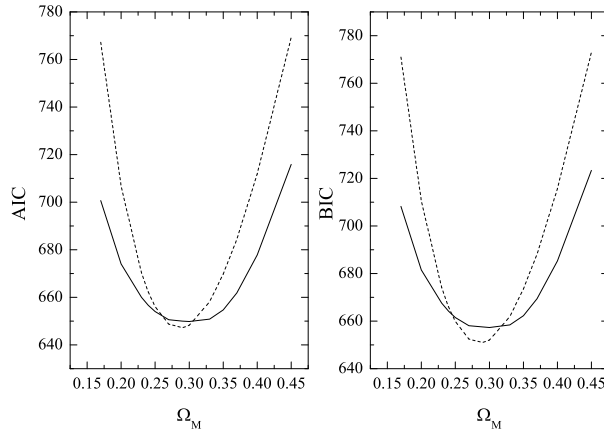


**Figure 5.2.** AIC (left panel) and BIC (right panel) tests in function of  $\Omega_m$  for the standard case of a cosmological constant (dashed line) and for the HS model (solid line).

In Fig. 5.2 we plot the best fit values of the  $AIC$  and  $BIC$  tests in function of  $\tilde{\Omega}_m$  for the standard model based on a cosmological constant and the HS model respectively. As we can see, while the cosmological constant gives slightly better values for the overall best fit, when larger or smaller values of  $\tilde{\Omega}_m$  are considered the  $AIC$  and  $BIC$  tests provide definitely better values for the HS model. In few words, there is a weaker dependence of the observables considered from  $\tilde{\Omega}_m$  in the case of HS scenario.

It is therefore important to quantify the impact of a different choice of the theoretical background model on the derived constraints on  $\tilde{\Omega}_m$ . In Fig. 5.3 we compare constraints on the  $\tilde{\Omega}_m$  parameter derived under the assumption of the HS scenario with the constraints obtained assuming General Relativity and a cosmological constant. As we can see the  $\tilde{\Omega}_m$  parameter is less constrained respect to the  $\Lambda$ CDM

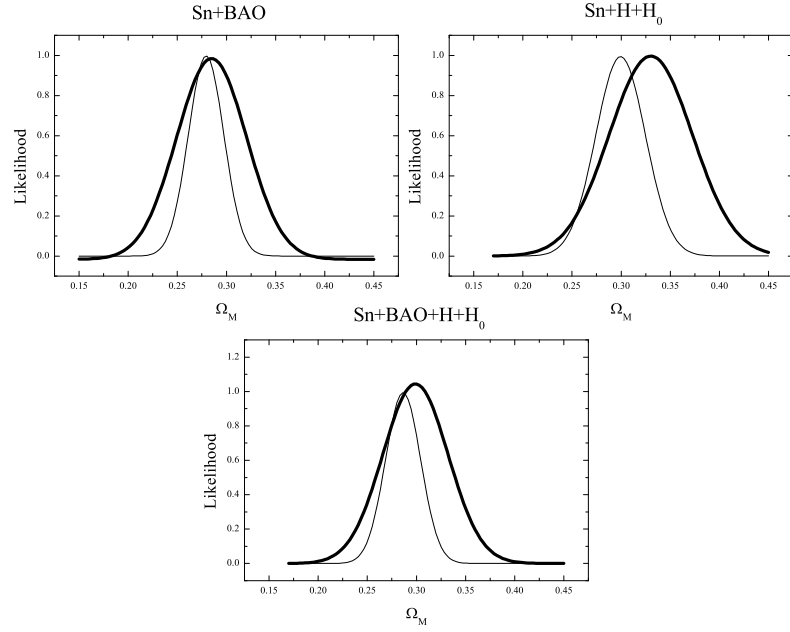


**Figure 5.3.** The likelihood function  $L(\tilde{\Omega}_m)$  for the Hu and Sawicki model (thicker lines) and  $\Lambda$ CDM model (fainter lines).

scenario. This is certainly due to the larger amount of parameters present in the HS model. In the future, with the increasing experimental accuracy, if a discrepancy between independent constraints on the matter density will be found then a modified gravity scenario could be suggested as possible explanation. This result anyway shows that one should also be extremely careful in considering the current cosmological constraints because of their model dependence.

## 5.2 Forecasted perturbation constraints

In [82] we analyze future structures growth data in order to determine how future experiments able to obtain this kind of data can improve constraints on the HS model. We also analyze a future supernovae survey in order to combine background data with growth of structures.

### SN Luminosity distance data

We exploit future SNIa data on the reduced magnitude

$$\mu = m - M = 5 \log_{10} d_L(z) + 25, \quad (5.5)$$

being  $d_L$  the luminosity distance. We consider here a mock catalog of 2,298 SNIa, with 300 SNIa uniformly distributed out to  $z = 0.1$ , as expected from ground-based low redshift samples, and an additional 1998 SNIa binned in 32 redshift bins in the range  $0.1 < z < 1.7$ , as expected from JDEM or similar future surveys [83]. We have considered both intrinsic and systematic errors on the reduced magnitude.

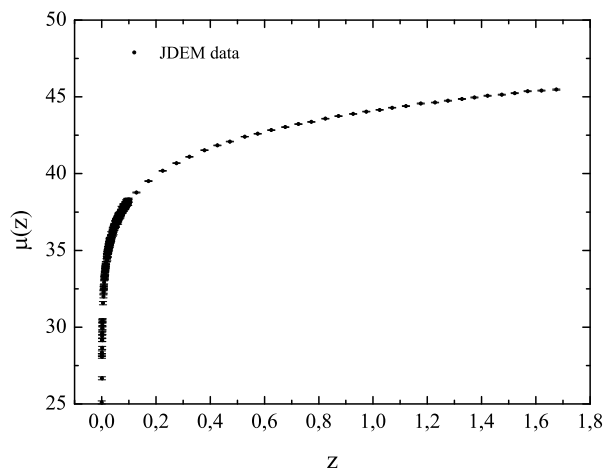


**Figure 5.4.** Forecasted SNIa luminosity distance data for a JDEM-like survey.

To produce mock SNIa luminosity distance and the following mock growth data from BAO surveys we assume a  $\Lambda$ CDM model with the following cosmological parameters:  $\Omega_b h^2 = 0.02258$ ,  $\Omega_c h^2 = 0.1109$ ,  $n_s = 0.963$ ,  $\tau = 0.088$ ,  $A_s = 2.43 \times 10^{-9}$  and  $\Theta = 1.0388$ , which correspond to the best-fit values from the WMAP seven year data analysis, see Ref. [6].

### Growth data

Galaxy surveys measure the redshift of the galaxies, providing, therefore, the redshift space galaxy distributions. From those redshifts the radial position of the galaxies are extracted. However, the inferred galaxy distribution (and, consequently, the power spectrum) is distorted with respect to the true galaxy distribution, because in redshift space one neglects the peculiar velocities of the galaxies. These are the so called *redshift space distortions*.

In linear theory and with a local linear galaxy bias  $b$  the relation between the true spectrum in real space and the spectrum in redshift space reads

$$P_{\text{redshift}}(\mathbf{k}) = \left(1 + \beta \mu_{\mathbf{k}}^2\right)^2 P(\mathbf{k}) , \quad (5.6)$$

where  $\beta \equiv f/b$ , being  $f$  the logarithmic derivative of the linear growth factor  $\delta(a)$  given by Eq. (3.60) and  $\mu_{\mathbf{k}}$  is the cosine of the angle between the line of sight and the wavevector  $\mathbf{k}$ . Notice that perturbations with  $\mathbf{k}$  perpendicular to the line of sight are not distorted. The relation among real space and redshift space overdensities given by Eq. (5.6) was first derived by Kaiser [84] and it arises from the continuity equation, which relates the divergence of the peculiar velocity to the dark matter overdensity  $\delta$ . Redshift space distortions, then, relate peculiar velocities to the logarithmic derivative of the linear growth factor,  $f$ . A measurement of  $\beta \equiv f/b$  will provide information on the growth of structure formation if the galaxy bias  $b$  is known.

In our analysis we have computed the forecasted errors for  $f$  assuming a  $\Lambda$ CDM fiducial model by means of a Fisher matrix analysis, marginalizing over the bias  $b$ . We focus here on the BAO experiments BOSS [85] and Euclid [86]. For the BOSS (Euclid) experiment we assume six (nineteen) redshift bins ranging from  $z = 0.15$  to  $z = 0.65$  ( $z = 0.15$  to  $z = 1.95$ ) and a galaxy survey area of 10000 (20000)  $\text{deg}^2$ . The mean galaxy densities for these two experiments are considered to be constant with values of  $2.66 \times 10^{-4}$  and  $1.56 \times 10^{-3} h \text{ Mpc}^{-3}$  for the BOSS and the Euclid surveys respectively.

We have combined the galaxy survey fisher matrices with the CMB Planck [87] Fisher matrix (see [88]). The expected errors on  $f$  are depicted in Figs. 5.5 and 5.6 and are similar to the ones obtained using the numerical tools of [89].

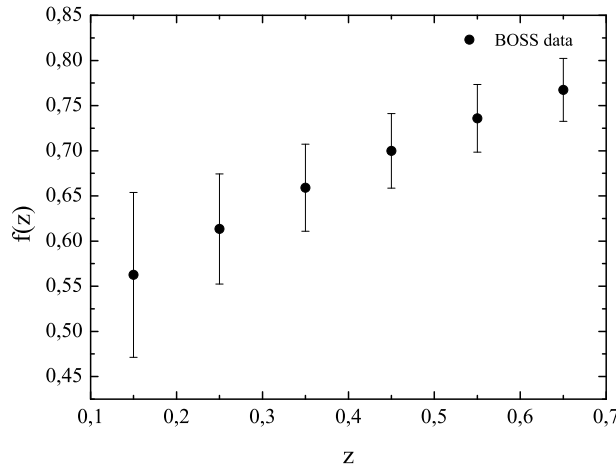
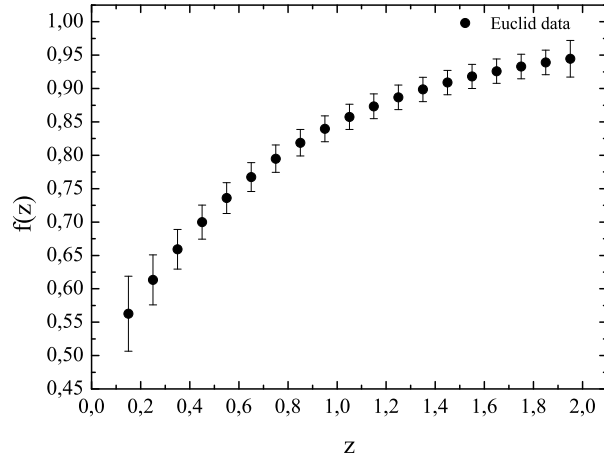


**Figure 5.5.** Forecasted BOSS data for  $f$ , the logarithmic derivative of the linear growth factor, as a function of the redshift.

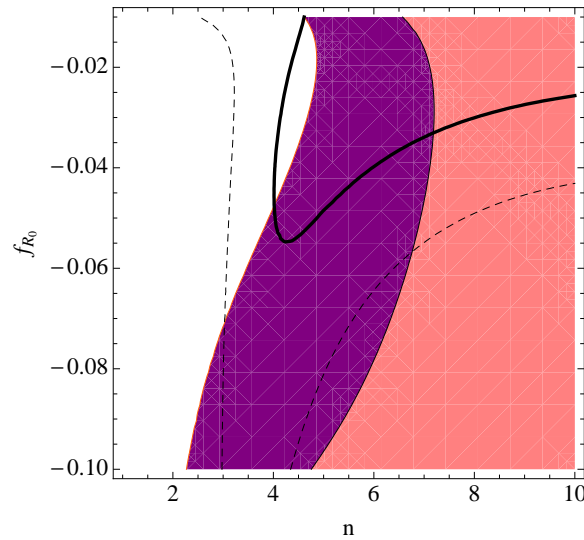
### 5.2.1 Future Data Analysis and Results

In this Section we perform a numerical fit to the HS model using the mock data sets described above by means of a  $\chi^2$  analysis. We compute two different  $\chi^2$  functions, one associated to growth of structure ( $\chi^2_{growth}$ ) and the other related to SNIa luminosity distance data,  $\chi^2_{SN}$ . The final likelihood will exclusively depend on the free parameter of the HS model,  $n$  and  $f_{R_0}$ , thus for the two different  $\chi^2$  analyses ( $\chi^2_{growth}$  and  $\chi^2_{SN}$ ) and well as for the combined one ( $\chi^2_{tot} = \chi^2_{growth} + \chi^2_{SN}$ ) we marginalize over  $\tilde{\Omega}_m$ . For the growth of structure we compute the  $\chi^2_{growth}$  at different scales  $k$  scales and perform a mean over  $k$  from  $k = 0.01h \text{ Mpc}^{-1}$  to  $k = 0.1h \text{ Mpc}^{-1}$ .

Figure 5.7 shows the 1 and 2- $\sigma$  contours on the  $(n, f_{R_0})$  plane arising from the analysis of SNIa luminosity distance data as well as from measurements of the linear growth of structure from the BOSS experiment. The empty regions depicted by the dotted and solid lines show the results from SNIa luminosity distance data, while the filled regions depict the results from the measurements of the linear growth of



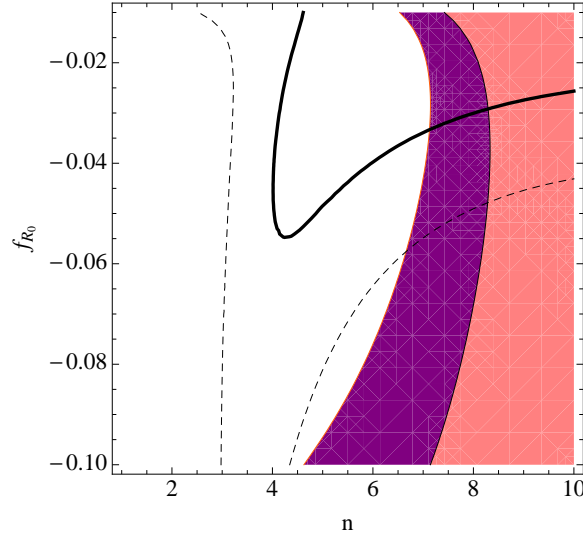
**Figure 5.6.** Forecasted Euclid data for  $f$ , the logarithmic derivative of the linear growth factor, as a function of the redshift.



**Figure 5.7.** 1 and 2- $\sigma$  contours in the  $(n, f_{R0})$  plane arising from SNIa measurements of the luminosity distance (black solid and dashed lines) and those arising from the BOSS measurements of the linear growth of structure (filled regions).

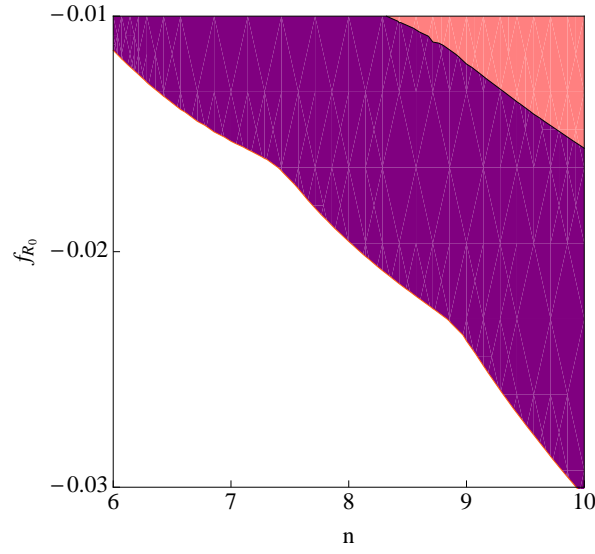
structure. Notice that background and growth measurements are complementary, allowing different regions in the parameter space. The combination of both data sets provide a very powerful tool to severely constrain the HS model.

Figure 5.8 shows the equivalent to Fig. 5.7 but considering measurements of the linear growth of structure from the Euclid galaxy survey. Notice that the currently allowed region will be ruled out if the true cosmology is a  $\Lambda$ CDM scenario. Therefore, the BOSS and Euclid surveys, combined with background SNIa luminosity



**Figure 5.8.** 1 and 2- $\sigma$  contours in the  $(n, f_{R_0})$  plane arising from SNIa measurements of the luminosity distance (black solid and dashed lines) and those arising from the Euclid measurements of the linear growth of structure (filled regions).

distance measurements, will be able to exclude a very large region of the parameter space of the HS model, allowing only for very high values of  $n$  for which  $c_1/c_2^2 \rightarrow 0$ , see Figs. 5.9 and 5.10 in which the combined analyses  $\chi_{tot}^2$  are shown. Figure 5.11 illustrates that, in the limit of  $c_1/c_2^2 \rightarrow 0$ , i.e. for very large values of  $n$ ,  $f(R)$  is equivalent to a cosmological constant. Therefore, future data from the Euclid galaxy survey combined with SNIa measurements will be able to recover the true fiducial cosmology even if the data is fitted to a non constant  $f(R)$ .



**Figure 5.9.** 1 and 2- $\sigma$  contours in the  $(n, f_{R_0})$  plane arising from BOSS measurements of the linear growth of structure combined with SNIa luminosity distance data from the JDEM survey. Note that the axis ranges are different to those of Fig. 5.7.

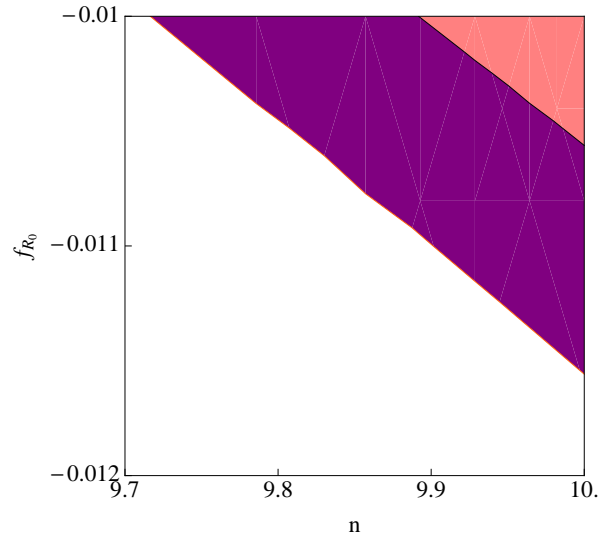


**Figure 5.10.** 1 and 2- $\sigma$  contours in the  $(n, f_{R_0})$  plane arising from Euclid measurements of the linear growth of structure combined with SNIa luminosity distance data from the JDEM survey. Note that the axis ranges are different to those of Figs. 5.7 and 5.9.

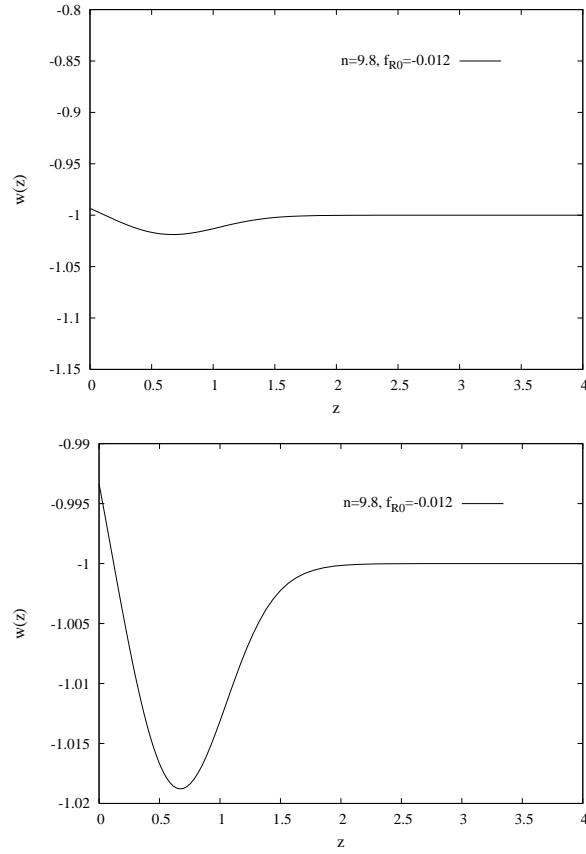


**Figure 5.11.** The top and bottom panels depict the effective equation of state  $w(z)$  for  $n = 9.8$  and  $f_{R_0} = -0.012$ , values that are in agreement with Euclid growth data. The top panel shows  $w(z)$  using the same ranges than those used in Fig.3.3. The bottom panel shows an axes range that allows to appreciate the behaviour of  $w(z)$ .



## Chapter 6

# General Constraints on Extended Theories of Gravity

In this Chapter we want to constrain the parameters used to describe modifications of General Relativity without the assumption of a specific modified gravity model such as HS. In particular we focus on  $f(R)$  theories, thus as we explained in Chapter 3.2 if we choose to keep the cosmological constant model background expansion, we have to add only an additional free parameter,  $\lambda_1^2$ , to the standard set of cosmological parameters: the baryon and cold dark matter densities  $\Omega_b h^2$  and  $\Omega_c h^2$ , the ratio of the sound horizon to the angular diameter distance at decoupling  $\theta_s$ , the scalar spectral index  $n_s$ , the overall normalization of the spectrum  $A_s$  at  $k = 0.002 \text{ Mpc}^{-1}$  and the optical depth to reionization  $\tau$ .

We also study the scalar-tensor theories configuration corresponding to a models where the new gravity theory interacts with matter with a *Yukawa-type* potential, with  $\lambda_1^2$ ,  $\beta_1$  and  $s$  as additional free parameters.

The analysis that we perform is based on the *Maximum Likelihood Principle*, directly connected with the Bayes theorem (see Appendix A for details); in the following Sections we will use different datasets, both current and forecasted, in order to build a multi-parameter likelihood function through Monte Carlo Markov Chain analysis based on the publicly available package `cosmomc` [90].

### 6.1 Current CMB constraints

In [49], in order to study our parameterization modified gravity (MG) models we run five MCMC chains. We use the parameters described in Table 6.1: this is based onto the usual set of  $\Lambda$ CDM parameters. As said above, to account for  $f(R)$  theories we have to add one extra parameter: here we chose to use  $B_0$  as a primary parameter. The other MG parameters are then fixed:  $\lambda_1^2 = c^2 B_0 / (2H_0^2)$ ,  $\lambda_2^2 = \beta_1 \lambda_1^2$ ,  $\beta_1 = 4/3$ ,  $\beta_2 = 1/2$  and  $s = 4$ . In theories with Yukawa-type dark matter interaction we have two additional free parameters, i.e. the coupling  $\beta_1$  and  $s$  as described above.

We shall discuss the effects of the parameter choice on the priors and on the results in more details in Section 6.1.3.

Parameter	Explanation	range (min, max)	
	Primary parameters	$f(R)$	Yukawa-type
$\omega_b$	physical baryon density; $\omega_b = h^2 \Omega_b$	(0.005, 0.100)	
$\omega_c$	physical CDM density; $\omega_c = h^2 \Omega_c$	(0.01, 0.99)	
$\vartheta_*$	sound horizon angle; $\vartheta_* = 100 \cdot r_s(z_*)/D_A(z_*)$	(0.5, 10.0)	
$\tau$	optical depth to reionisation	(0.01, 0.80)	
$\Omega_K$	curvature density; $\Omega_K = 1 - \Omega_{\text{tot}}$	0	
$\ln(10^{10} A_s^2)$	$A_s$ is the scalar primordial amplitude at $k_{\text{pivot}} = 0.05 \text{ Mpc}^{-1}$	(2.7, 4.0)	
$A_{\text{SZ}}$	amplitude of the SZ template for WMAP and ACBAR	(0, 2)	
$n_s$	spectral index of primordial perturbations; $n_s - 1 = d \ln P/d \ln k$	(0.5, 1.5)	
$B_0$	present lengthscale of the theory (in units of the horizon scale)	(0, 6)	(0, 6)
$\beta_1$	coupling	4/3	(0.001, 2)
$s$	time evolution of the scalaron mass	4	(1, 4)
	Derived parameters		
$H_0$	Hubble parameter [km/s/Mpc]; calculated from $\omega_b$ , $\omega_c$ , $\vartheta$ , and $\Omega_K$	tophat (40, 100)	
$h$	$h = H_0/(100 \text{ km/s/Mpc})$	(0.40, 1.00)	
$\Omega_m$	matter density parameter; $\Omega_m = (\omega_b + \omega_c)/h^2$		
$\Omega_\Lambda$	vacuum energy density parameter; $\Omega_\Lambda = 1 - \Omega_K - \Omega_m$		
$\lambda_1^2$	lengthscale of the theory; $\lambda_1^2 = B_0 c^2/(2H_0^2)$	$(0, 5 \cdot 10^7)$	$(0, 5 \cdot 10^7)$
$\lambda_2^2$	second lengthscale of the theory; $\lambda_2^2 = \beta_1 \lambda_1^2$	$(0, 7 \cdot 10^7)$	$(0, 10^8)$
$\beta_2$	anisotropy parameter; $2/\beta_1 - 1$	1/2	(0, 2000)

**Table 6.1.** Our primary MCMC sampling parameters and some important derived parameters. The modified gravity parameters are separated by a horizontal line.

### 6.1.1 Data

#### CMB

For the CMB we use the publicly released WMAP 5 years data [92] for the temperature and polarisation (TT, TE and EE) power spectra of the perturbations. In addition, we used flat top hat priors on the age of the Universe,  $t_0 \in [10, 20]$  Gyrs and on the Hubble parameter today  $H_0 \in [40, 100]$  km/s/Mpc. We include CMB lensing in the analysis.

#### ISW

To break the degeneracy which remains at the background level between GR and MG, we use the ISW data by [93]. These data were obtained by cross-correlating the WMAP maps of the CMB with six galaxy data sets in different bands (2MASS, SDSS main galaxies, LRGs and QSOs, NVSS, HEAO). The data span different redshift ranges from  $\bar{z} = 0.1$  to  $\bar{z} = 1.5$ , thus allowing us to study the evolution of gravity, through the history of the decay of its potentials, in a tomographic way.

There are 78 actual data points, consisting of the angular cross-correlation functions (CCFs) in real space, binned at 12 angles between 0 and 12 deg for each of the catalogues. The full covariance matrix is highly non-diagonal both between the different angular bins and between the catalogues, due to overlaps in redshift and sky coverage. For each MC model, the likelihood contribution due to the ISW data is calculated as follows: first the theoretical matter and matter-temperature power spectra  $C_l^{gg}$ ,  $C_l^{Tg}$  are calculated through a full Boltzmann integration inside CAMB, then a Legendre transformation yields the CCFs and the matter auto-correlation functions (ACFs) at the relevant scales. Finally, the bias parameters, assumed constant for each catalogue, are recalculated for each model by forcing the ACFs to

match the observations.

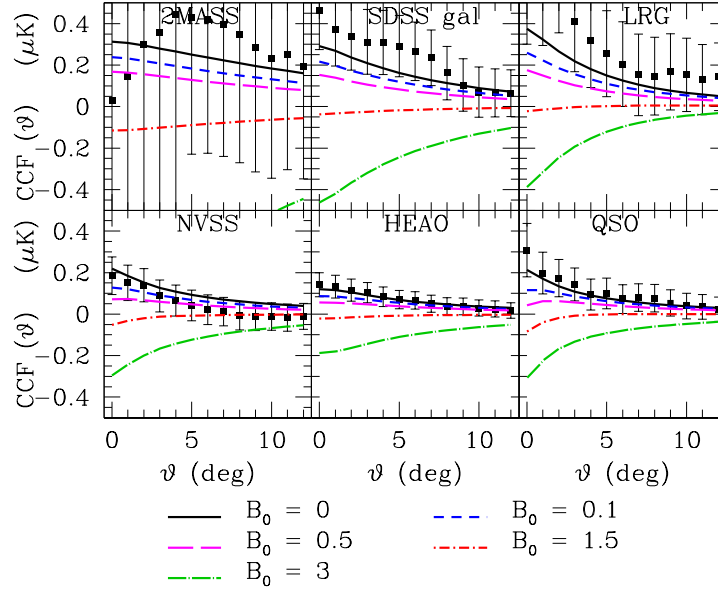


**Figure 6.1.** Theoretical predictions for a family of  $f(R)$  theories compared with our ISW data [93] measuring the angular CCF between the CMB and six galaxy catalogues. The model with  $B_0 = 0$  is equivalent to  $\Lambda$ CDM, while increasing departures from GR produce negative cross-correlations.

We show in Fig.6.1 and Fig.6.2 the CCF data points, overlapped with the theoretical predictions for a family of  $f(R)$  and Yukawa-like theories. We can see that in the first case a departure from GR produces an unobserved negative signal, while in the second a coupling different from unity causes an equally unobserved redshift evolution of the effect.

## Supernovae

To further constrain the background expansion history of the Universe, we study the effect of including the constraints from the Hubble diagram of distant Type Ia Supernovae (SNe). In particular we use the Union SN compilation by [76], which consists of 414 SNe drawn from 13 independent data sets plus 8 newly discovered SNe at low redshift, all reanalysed in a consistent way.

### 6.1.2 Results & constraints

#### $f(R)$ theories

In order to be conservative, we first perform an MCMC analysis using the constraints from CMB+ISW only, as it is in general good practice to add data sets gradually, to control that there are no strong tensions between them, which would produce artificially tight posteriors. We show in Fig. 6.3 (red dashed lines) our constraints

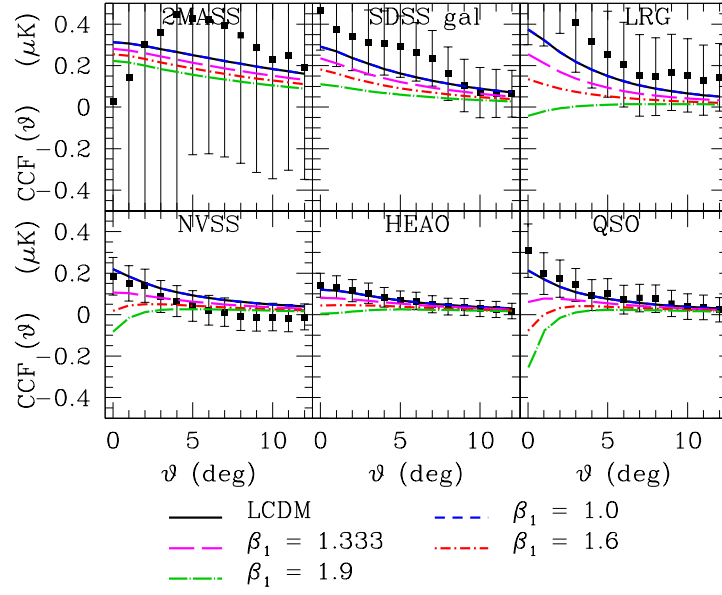


**Figure 6.2.** Same as previous plot for a family of Yukawa-like theories with fixed  $B_0 = 2$ . In this case non-unitary coupling generate a redshift evolution of the signal.

from this run. Here we see the one-dimensional marginalised likelihood distributions of the cosmological parameters. It can be seen that the usual  $\Lambda$ CDM parameters have likelihoods peaked around their standard values, while the extra parameter  $B_0$  has an upper limit, so that we find

$$B_0 < 0.5 \quad \text{or} \quad \lambda_1 < 2000 \text{ Mpc}/h \quad @95\% \text{ c.l.} \quad (6.1)$$

This result, which has been made possible by a full combined CMB-ISW analysis data, improves the previous constraints of  $B_0 < 1$  by [94], obtained only by considering models with a positive ISW-matter correlation signal.

We then perform a new analysis by adding the constraints from the Union supernovae catalogue by [76]. By adding these constraints, the parameter space allowed from the background expansion history becomes narrower, and thus so become the constraints on the modification of gravity, mainly due to the degeneracy of the theory wavelength  $\lambda_1$  with other parameters such as  $\Omega_m$ , as can be seen in the 2D contour plot of Fig. 6.5 (top panel). We can see the one-dimensional marginalised likelihood curves for the models in Fig. 6.3 (black solid lines). The resulting constraint from the combination of CMB+ISW+SN is

$$B_0 < 0.4 \quad \text{or} \quad \lambda_1 < 1900 \text{ Mpc}/h \quad @95\% \text{ c.l.} \quad (6.2)$$

We have also tested how the results can improve by adding the latest additional priors on the value of the Hubble constant  $H_0$  [95]; however, since the background is already well constrained by the interSection of CMB and SNe data, the improvement is marginal (at the percent level in the value of the upper limit).

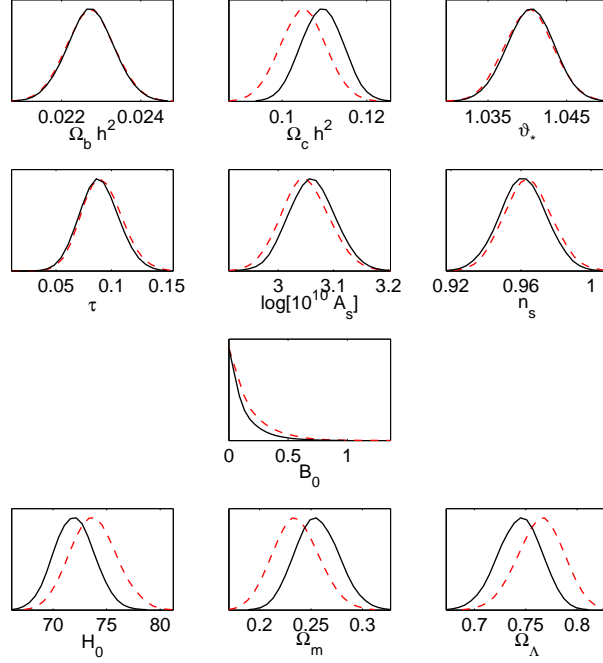


**Figure 6.3.** Posterior likelihood distributions for the model parameters for the  $f(R)$  case, using the combined CMB and ISW data (red, dashed lines) and adding also the SNe data (black, solid). We can see that the usual  $\Lambda$ CDM parameters peak around the concordance values, while the extra parameter  $B_0$  has an upper limit. The SNe tighten the constraints by reducing the degeneracy between  $\Omega_m$  and  $B_0$ .

### Yukawa-type dark matter interaction

Finally we perform an analysis with three parameters to investigate theories in which dark matter particles interact via a Yukawa-type force. In this case, we directly include all data sets, i.e. CMB ISW and SNe, since we expect the marginalised constraints to be weaker due to the additional parameters. We can see the result of the 1D posterior likelihood in Fig. 6.4. In this case, the upper limit on  $B_0$  (or  $\lambda_1^2$ ) is weakened and becomes uninteresting due to additional degeneracies, while we find a constraint on the coupling parameter

$$0.75 < \beta_1 < 1.25 \text{ @ } 95\% \text{ c.l.} \quad (6.3)$$

This limit is enhanced by the lack of strong redshift evolution of the ISW signal. The result is comparable with the previous constraints by [96], although obtained under different assumptions. We can not find any significant bound on the additional parameter  $s$ . We show in the bottom panels of Fig. 6.5 the 2D likelihood contours for  $\Omega_m, B_0, \Omega_m, \beta_1$  and  $\beta_1, B_0$ .

From the last panel of Fig. 6.5 we can better understand why the constraint on  $B_0$  is now weakened. In the  $f(R)$  case, the coupling parameter is fixed to  $\beta_1 = 4/3$ , for which high values of  $B_0$  are disfavoured. When the coupling is set free in the Yukawa-type theories, its preferred values are around  $\beta_1 \simeq 1$ , for which we can see that  $B_0$  is unconstrained.

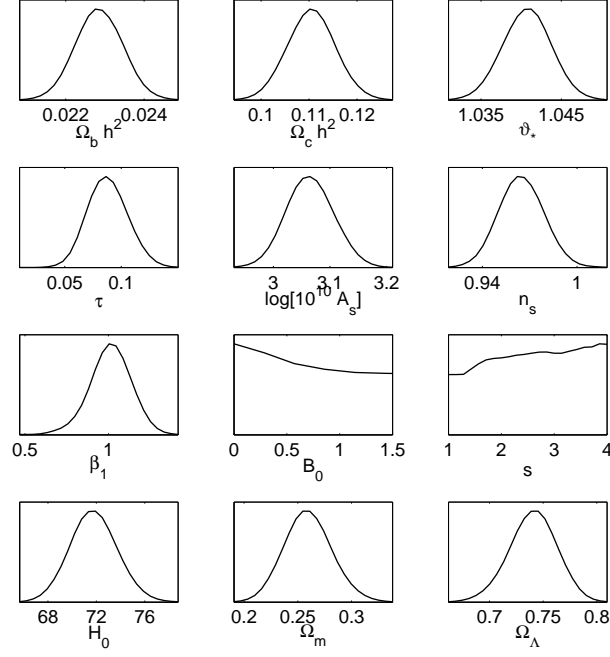


**Figure 6.4.** Posterior likelihood distributions for the Yukawa-type case. Here we only show the full CMB+ISW+SN result. The upper limit on  $B_0$  disappears in this case due to the removal of the corrective factor from calculated in [49] and the additional degeneracies, and we can not constrain  $s$  either, but a value of the coupling  $\beta_1$  close to unity is required to fit the data.

### 6.1.3 On the parametrisations and the Bayesian priors

In Bayesian theory, the posterior probability of a model  $M$  with  $N$  parameters  $\Theta$  given the data  $\mathbf{D}$  is obtained as

$$\mathcal{P}(\theta|\mathbf{d}) = \frac{L(\mathbf{d}|\theta)\mathcal{P}(\theta)}{\mathcal{P}(\mathbf{d})}, \quad (6.4)$$

where, as in Appendix A  $L(\mathbf{d}|\theta)$  is the likelihood function,  $\mathcal{P}(\theta)$  the prior and  $\mathcal{P}(\mathbf{d})$  is the Bayesian evidence for the model, which we can here consider constant. The marginalised posterior of a single parameter  $\theta$  is then obtained integrating over the other parameters:

$$\mathcal{P}(\theta|\mathbf{d}) \propto \int \mathcal{P}(L(\mathbf{d}|\theta)\theta) d^{N-1}\theta. \quad (6.5)$$

We normally assume the priors to be flat over the sampled interval, so that they can be ignored in the marginalisation process. In this case, the posterior is simply mapped by the likelihood, upon which assumption the MCMC technique is based. However, if we change one parameter as  $\theta \rightarrow \zeta(\theta)$ , we have that a prior which was flat in  $\theta$  will not in general be flat in  $\zeta$ . In other words, changing parametrisation modifies the prior from  $\mathcal{P}(\theta)$  to

$$\mathcal{P}(\zeta) = \mathcal{P}(\theta) \frac{d\theta}{d\zeta}, \quad (6.6)$$

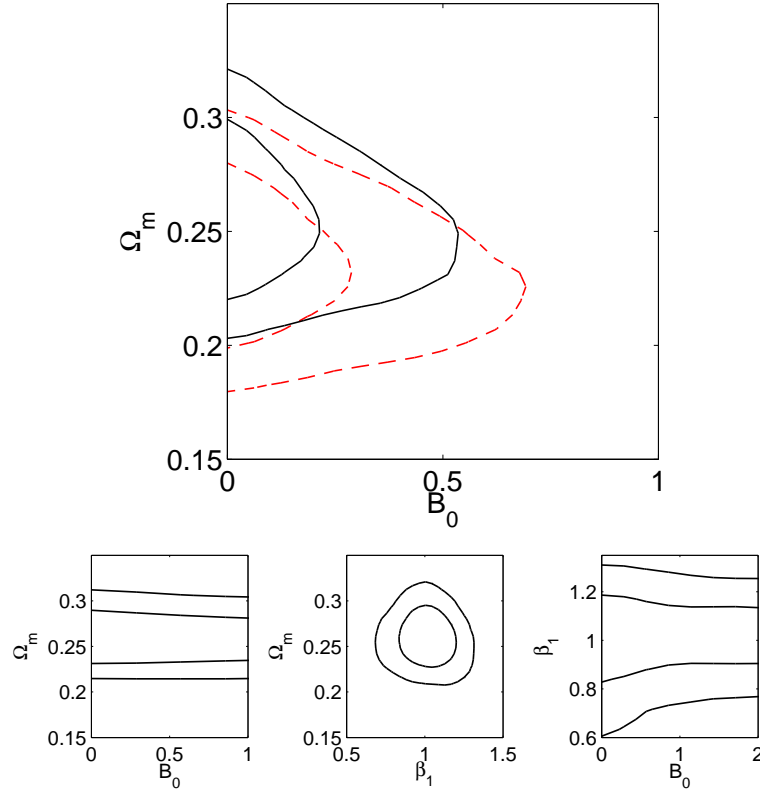


**Figure 6.5.** 2D posterior likelihood distributions; the 68% and 95% probability contours are shown. In the top panel we can see the parameters  $\Omega_m, B_0$  for the  $f(R)$  case, using the combined CMB and ISW data (red, dashed lines) and adding also the SNe data (black, solid). The SNe tighten the constraint by reducing the degeneracy between  $\Omega_m$  and  $B_0$ . In the bottom panels, we show the Yukawa-type case for the parameters  $\Omega_m, B_0$  (left),  $\Omega_m, \beta_1$  (centre), and  $\beta_1, B_0$  (right).

which corresponds to a different weighting of the likelihood in Eq.(6.5); in higher dimensions, the derivative is replaced by the Jacobian of the transformation, as described for example in [97]. If we now run an MCMC chain using the new parameter  $\zeta$  as a primary parameter, we will in practice force the prior  $\mathcal{P}(\zeta)$  to be flat, meaning that the prior on the old parameter  $\mathcal{P}(\theta)$  will be tilted by a factor  $d\zeta/d\theta$ . If a prior is tilted, it will cause a downweighting of the parameter region in one direction, thus affecting the results. All this is well known, and it has been discussed by [90]. Clearly, if the theory is well constrained by the data, then the interval of integration will be small, and the prior will be approximately flat in any parametrisation, yielding consistent posteriors. However, this does not apply to our case: since the current data are not yet strongly constraining MG, we have found that the choice of priors does indeed have strong effects. This leaves us with the problem of deciding which of the many possible MG parameters ( $B_0, \lambda_1, \lambda_1^2, \text{Log}\lambda_1^2, \dots$ ) is most *meaningful* or *well justified* to be assumed having flat priors. The conclusion seems uncertain since any modification of gravity is currently based on speculation without experimental backing, and it is thus hard to decide which parametrisation ought

to be preferred on physical grounds. Since there is no evidence for a modification of GR, we have then decided to make the most conservative choice by presenting the parametrisation which yields the weakest constraints on this modification.

$\zeta$	$d\zeta/d\lambda_1$	$d^2\zeta/d(\lambda_1)^2$	prior on $\lambda_1$	bias on $\lambda_1$	$\lambda_1$ @ 95% c.l.
$\lambda_1$	1	0	flat	baseline	$\lambda_1 < 1400$ Mpc/h
$\lambda_1^2$	$\propto \lambda_1$	$> 0$	positive tilt	biased to higher $\lambda_1$	$\lambda_1 < 1900$ Mpc/h
$B_0$	$\propto \lambda_1$	$> 0$	positive tilt	biased to higher $\lambda_1$	$\lambda_1 < 1900$ Mpc/h
$\text{Log } \lambda_1^2$	$\propto 1/\lambda_1$	$< 0$	negative tilt	biased to lower $\lambda_1$	$\lambda_1 < 700$ Mpc/h

**Table 6.2.** Effect of the priors on the estimation of the baseline parameter  $\lambda_1$ . Using flat priors on different parameters  $\zeta$  defined by transformations whose second derivative is positive (negative) will produce effective tilted priors on  $\lambda_1$ . This will overestimate regions with higher (lower)  $\lambda_1$ , thus leading to biased posteriors. The results of MCMC chains using different parameters agree with this prediction.

Nevertheless, at least in the simplest  $f(R)$  case with one extra parameter, we can forecast the effect of the different options by using Eq. (6.6). If we take the parameter  $\lambda_1$  as our baseline choice, we can predict that by switching to flat priors in the other parameters we will have the effects summarised in Table 6.2: any transformation to a parameter  $\zeta$  with  $d^2\zeta/d(\lambda_1)^2 > 0$  will tilt the priors — and bias the posteriors — towards higher values of  $\lambda_1$ ; the opposite for  $d^2\zeta/d(\lambda_1)^2 < 0$ .

Finally we compare these predictions with the results we infer on the baseline parameter  $\lambda_1$  by running MCMC chains using different primary parameters; we find a good agreement with the prediction, and in particular we confirm that our choice of  $B_0$  (or equivalently  $\lambda_1^2$ ) is the most conservative one. If we decide that the wavelength  $\lambda_1$  should be considered the most physically justified quantity, we then obtain the following stricter bounds in the  $f(R)$  case using CMB+SN+ISW:

$$\lambda_1 < 1400 \text{ Mpc/h} \quad \text{or} \quad B_0 < 0.2 \quad @ 95\% \text{ c.l.} \quad (6.7)$$

## 6.2 Forecasted constraints

We can use the MCMC method already used above to forecast the future accuracy of forthcoming experiments. To do this we need to create simulated datasets and to write a likelihood function to analyze these datasets.

It is possible to evaluate a priori the likelihood of the data for a given theoretical model exactly from the temperature and polarization maps. The standard likelihood is given by

$$L(\vec{m}|S) d\vec{m} = \frac{\exp\left[-\frac{1}{2}\vec{m}^t(S+N)^{-1}\vec{m}\right]}{\sqrt{|S+N|}} \frac{d\vec{m}}{(2\pi)^{3n_p/2}} \quad (6.8)$$

where  $\vec{m}$  is the data vector containing the temperature map,  $\vec{T}$ , as well as the polarization maps,  $Q$ , and  $U$ ,  $n_p$  is the number of pixels of each map, and  $S$  and  $N$  are the signal and noise covariance matrix ( $3n_p \times 3n_p$ ), respectively.

In real cases is computationally impossible to evaluate this function at high resolution (better than  $1^\circ$ ). This is connected to the fact that for high resolution we have to analyze too many pixels and the signal and noise covariance matrix are too heavy to handle.



For this reason under the assumption of white noise, absence of foregrounds and full sky observation we can rewrite the likelihood function in a more convenient way:

$$-2 \ln P(T|C_\ell) = \sum_\ell (2\ell + 1) \left[ \ln \left( C_\ell B_\ell^2 + \mathcal{N}_\ell \right) + \frac{\mathcal{D}_\ell}{C_\ell B_\ell^2 + \mathcal{N}_\ell} \right] \quad (6.9)$$

with  $\mathcal{N}_\ell = \ell(\ell + 1)N_\ell/2\pi$ , where  $N_\ell = \langle |n_{\ell m}|^2 \rangle$  is the noise power spectrum in spherical harmonics, and  $\mathcal{D}_\ell = [\ell(\ell + 1)/2\pi] \sum_m |a_{\ell m}|^2/(2\ell + 1)$  is the power spectrum of the full data (noise plus beam-smoothed signal).

It is possible to compute the noise power spectrum starting for a given experiment from the sensitivity per pixel ( $\sigma_c$ ) and the beam ( $\theta_c$ ) of each experimental frequency channel [98]:

$$w_c^{-1} = (\sigma_c \theta_c)^2 \quad (6.10)$$

where  $\theta$  is the FWHM (Full-Width at Half-Maximum) of the beam assuming a Gaussian profile and  $\sigma$  is the temperature sensitivity  $\Delta T$ . The  $B_\ell$  term is the beam transfer function defined as

$$B_\ell \equiv \sum_c e^{-\frac{\ell(\ell+1)}{l_c^2}} \quad (6.11)$$

where  $l_c$  is given by for each experimental channel:

$$l_c = \sqrt{8 \ln 2} / \theta_c \quad (6.12)$$

It is possible to generalize Eq.(6.9) to the  $n$ -spectra case simply replacing  $\mathcal{D}_\ell$ ,  $\mathcal{N}_\ell$  and  $C_\ell$  with the corresponding matrices  $\hat{\mathcal{D}}_\ell$ ,  $\hat{\mathcal{N}}_\ell$  and  $\hat{C}_\ell$  containing the different spectra:

$$-2 \ln P(T|\hat{C}_\ell) = \sum_\ell (2\ell + 1) \left[ \ln \left| \hat{C}_\ell \hat{B}_\ell^2 + \hat{\mathcal{N}}_\ell \right| + \frac{\hat{\mathcal{D}}_\ell}{\hat{C}_\ell \hat{B}_\ell^2 + \hat{\mathcal{N}}_\ell} \right] \quad (6.13)$$

### 6.2.1 CMB data

In order to use this Eq.(6.13) to forecast future CMB results, we must generate a simulated dataset starting from the experimental characteristics of the instrument considered and from a theoretical CMB power spectrum. In the following Sections we will use full mock CMB datasets (temperature, E-polarization mode and lensing deflection field) with noise properties consistent with the Planck [87] and CMBpol/EPIC experiments [99] (see Tab. 6.3 for specifications).

The Planck satellite, launched on May of 2010 is currently working and it shall be able, in the next years, to provide measurements of the CMB with unprecedented accuracy.

In the last years several new experiments have been planned to complete the future observation of Planck, such as the future CMB mission CMBpol/EPIC. This future satellite will be able to detect the CMB polarization spectra with a sensitivity than the one planned for Planck. This way it will be able to further improve the constraints that will be soon released by the Planck collaboration.

Experiment	Channel	FWHM	$\Delta T/T$
Planck	70	14'	4.7
	100	10'	2.5
	143	7.1'	2.2
$f_{sky} = 0.85$			
CMBpol/EPIC	70	12'	0.05
	100	8.4'	0.05
	150	5.6'	0.06
$f_{sky} = 0.85$			

**Table 6.3.** Planck and CMBpol/EPIC experimental specifications. Channel frequency is given in GHz, FWHM (Full-Width at Half-Maximum) in arc-minutes, and the temperature sensitivity per pixel in  $\mu K/K$ . The polarization sensitivity is  $\Delta E/E = \Delta B/B = \sqrt{2}\Delta T/T$ .

In order to create a mock dataset for these two experiments, we consider, when dealing with temperature and polarization CMB spectra, for each channel a detector noise of  $w^{-1} = (\theta\sigma)^2$  and add to each  $C_\ell$  fiducial spectra a noise spectrum given by:

$$N_\ell = w^{-1} \exp(\ell(\ell + 1)/\ell_b^2), \quad (6.14)$$

where  $\ell_b$  is given by  $\ell_b \equiv \sqrt{8 \ln 2}/\theta$ .

Moreover we include in the CMB datasets also the lensing deflection power spectrum of Eq.(4.31); we make use of the method presented in [69] to construct the weighting factor  $W$  of Eq. (4.33). In that paper, the authors choose  $W$  to be a function of the power spectra  $C_\ell^{ab}$ , which include both CMB lensing and primary anisotropy contributions. This choice leads to five quadratic estimators, with  $ab = TT, TE, EE, EB, TB$ ; the  $BB$  case is excluded because the method of Ref. [69] is only valid when the lensing contribution is negligible compared to the primary anisotropy, assumption that fails for the B modes in the case of Planck.

In the case of CMBpol/EPIC we have decided to neglect the  $BB$  channel since it may be contaminated by unknown foregrounds and/or it may be used for foregrounds removal. The results presented here for the CMBpol/EPIC mission have therefore to be considered as conservative.

The five quadratic estimators can be combined into a minimum variance estimator which provides the noise on the deflection field power spectrum  $C_\ell^{dd}$ :

$$N_\ell^{dd} = \frac{1}{\sum_{aa'bb'} (N_\ell^{aba'b'})^{-1}}. \quad (6.15)$$

We compute the minimum variance lensing noise for Planck experiment by means of a routine publicly available at <http://lesgourg.web.cern.ch/lesgourg/codes.html>. The datasets (which include the lensing deflection power spectrum) are analyzed with a full-sky exact likelihood routine available at the same URL.

## 6.2.2 Galaxy weak lensing data

Future weak lensing surveys will measure photometric redshifts of billions of galaxies allowing the possibility of 3D weak lensing analysis (e.g.[100, 101, 102, 103]) or a

$n_{gal}(\text{arcmin}^{-2})$	$redshift$	$f_{sky}$	$\gamma_{rms}^2$
35	$0 < z < 2$	0.5	0.22

**Table 6.4.** Specifications for the Euclid like survey considered in this paper. The table shows the number of galaxies per square arcminute ( $n_{gal}$ ), redshift range,  $f_{sky}$  and intrinsic ellipticity ( $\gamma_{rms}^2$ ).

tomographic reconstruction of growth of structures as a function of time through a binning of the redshift distribution of galaxies, with a considerable gain of cosmological information (e.g. on neutrinos [72]; dark energy [103]; the growth of structure [104, 105] and map the dark matter distribution as a function of redshift [106]).

In [107] we use typical specifications for futures weak lensing surveys like the Euclid experiment, observing about 35 galaxies per square arcminute in the redshift range  $0 < z < 2$  with an uncertainty of about  $\sigma_z = 0.03(1+z)$  (see [86]), to build a mock dataset of convergence power spectra. Table 6.4 shows the number of galaxies per arcminute<sup>-2</sup> ( $n_{gal}$ ), redshift range,  $f_{sky}$  and intrinsic ellipticity for this survey. The expected  $1\sigma$  uncertainty on the convergence power spectra  $P(\ell)$ , expressed as  $C_\ell$  in Eq.(4.43), is given by [108]:

$$\sigma_\ell = \sqrt{\frac{2}{(2\ell+1)f_{sky}\Delta_\ell}} \left( P(\ell) + \frac{\gamma_{rms}^2}{n_{gal}} \right) \quad (6.16)$$

where  $\Delta_\ell$  is the bin used to generate data. Here we choose  $\Delta_\ell = 1$  for the range  $2 < \ell < 100$  and  $\Delta_\ell = 40$  for  $100 < \ell < 1500$ . For the convergence power spectra we use  $\ell_{max} = 1500$  in order to exclude the scales where the non-linear growth of structure is more relevant and the shape of the non-linear matter power spectra is, as a consequence, more uncertain (see [109]). We describe the galaxy distribution of Euclid survey as in [110],  $n(z) \propto z^2 \exp(-(z/z_0)^{1.5})$  where  $z_0$  is set by the median redshift of the sources,  $z_0 = z_m/1.41$ . Here we calculate the power spectra assuming a median redshift  $z_m = 1$ . Although this assumption is reasonable for Euclid, it is known that the parameters that controls the shape of the distribution function may have strong degeneracies with some cosmological parameters as matter density,  $\sigma_8$  and spectral index ([111]). However we conduct an analysis also varying the value of  $z_m$ , finding no significant variations in the results (see below).

In one case we show also constraints achievable with tomography dividing the distribution  $n(z)$  in three equal redshift bins. The distribution we are using is showed in Figure 6.6 normalized so that  $\int n(z)dz = 1$ , together with the distributions of each redshift bin. As said above Euclid will observe about 35 galaxies per square arcminute corresponding to a total of  $\sim 2.5 \cdot 10^9$  galaxies. In the tomographical analysis each one of the bins in Figure 6.6 contains respectively 25%, 51% and 26% of the sources. As expected, using tomography, we find an improvement on the cosmological parameters with respect to the single redshift analysis. However, in this first-order analysis we are not considering other systematic effects as intrinsic alignments of galaxies, selection effects and shear measurements errors due to uncertainties in the point spread function (PSF) determination. Future real data analysis will require the complete treatment of these effects in order to avoid biases

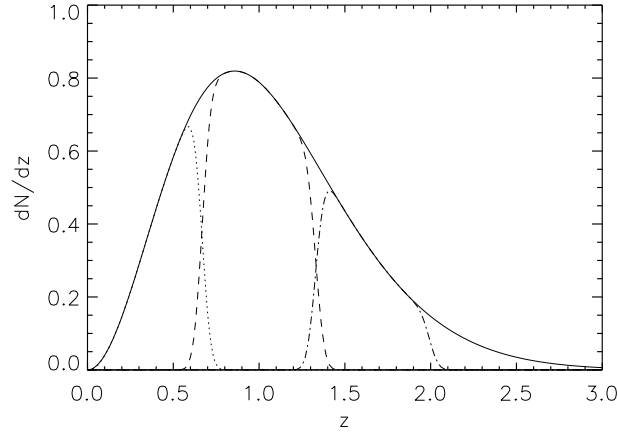


**Figure 6.6.** Redshift distribution of the sources used in this analysis and galaxy distributions in each redshift bin used for the tomography.

on the cosmological parameters. Moreover the uncertainty we are assuming on the redshift is the most optimistic value for Euclid and we note also that the intrinsic ellipticity value of table 6.4 is probably redshift dependent, and may be higher for the fainter galaxies at higher redshifts. For all these reasons we use the convergence power spectra calculated at a single redshift to do most of our forecasts, in order to be more conservative.

### 6.2.3 Forecasted Results

#### Future CMB missions

In this Section we perform two different analysis; firstly, we evaluate the achievable constraints on the  $f(R)$  parameter  $\lambda_1^2$  without including the lensing deflection spectra in Planck and CMBpol datasets. Secondly, we add the deflection spectra in order to find out how much improvement this tool can bring to the constraints. We perform a Monte Carlo Markov Chain analysis based on the publicly available package `cosmomc` [90] with a convergence diagnostic using the Gelman and Rubin statistics.

In order to build our CMB datasets, we assume a fiducial model for the standard cosmological parameters that is the best-fit from the WMAP seven years analysis of Ref. [112] with  $\Omega_b h^2 = 0.02258$ ,  $\Omega_c h^2 = 0.1109$ ,  $n_s = 0.963$ ,  $\tau = 0.088$ ,  $A_s = 2.43 \times 10^{-9}$ ,  $\Theta = 1.0388$ .

For modified gravity parameters, we assume a fiducial value  $\lambda_1^2 = 0 \text{ Mpc}^2$  and fix  $\beta_1 = 1.33$  and  $s = 4$  to test the constraints achievable on  $f(R)$  models.

In Table 6.5 we can see how the introduction of the lensing deflection spectrum  $C_\ell^{dd}$  and the cross-correlation with temperature  $C_\ell^{Td}$  in the Planck analysis brings to an improvement only in the  $\lambda_1^2$  constraint, while the other parameters are barely affected.

In Table 6.6 we can see instead how adding the lensing information to the

	Planck no lens	Planck lens
Fiducial: Parameter	$\lambda_1^2 = 0$	$\lambda_1^2 = 0$
$\Delta(\Omega_b h^2)$	0.00015	0.00013
$\Delta(\Omega_c h^2)$	0.0012	0.0010
$\Delta(\theta_s)$	0.00031	0.00027
$\Delta(\tau)$	0.0047	0.0041
$\Delta(n_s)$	0.0038	0.0031
$\Delta(\log[10^{10} A_s])$	0.016	0.013
$\Delta(H_0)$	0.62	0.50
$\Delta(\Omega_\Lambda)$	0.0068	0.0050
$\lambda_1^2(\text{Mpc}^2)$	$< 4.3 \times 10^5$	$< 2.42 \times 10^4$

**Table 6.5.** 68% c.l. errors on cosmological parameters using Planck without and with lensing extraction. Upper limits on  $\lambda_1^2$  are 95% c.l. constraints.

CMBpol/EPIC dataset, the parameter are slightly more affected. This can be explained with the fact that the better sensitivity of CMBpol for temperature and polarization CMB spectra brings to a better lensing extraction and therefore to a lower noise, as we can see in Fig.6.7.

	CMBpol no lens	CMBpol lens
Fiducial: Parameter	$\lambda_1^2 = 0$	$\lambda_1^2 = 0$
$\Delta(\Omega_b h^2)$	0.00004	0.00003
$\Delta(\Omega_c h^2)$	0.0005	0.0003
$\Delta(\theta_s)$	0.00007	0.00004
$\Delta(\tau)$	0.0023	0.0020
$\Delta(n_s)$	0.0018	0.0013
$\Delta(\log[10^{10} A_s])$	0.008	0.005
$\Delta(H_0)$	0.23	0.13
$\Delta(\Omega_\Lambda)$	0.0028	0.0016
$\lambda_1^2(\text{Mpc}^2)$	$< 4.0 \times 10^4$	$< 2.41 \times 10^3$

**Table 6.6.** 68% c.l. errors on cosmological parameters using CMBpol without and with lensing extraction. Upper limits on  $\lambda_1^2$  are 95% c.l. constraints.

### Future Weak Lensing missions

In [107] we choose to perform two different analysis; firstly, we evaluate the achievable constraints on the  $f(R)$  parameter  $\lambda_1^2$  and on the more general scalar-tensor parametrization including also  $\beta_1$  and  $s$ . Secondly, we investigate the effects of a wrong assumption about the gravity framework on the cosmological parameters, by generating an  $f(R)$  datasets with non-zero  $\lambda_1^2$  fiducial value but analysing it assuming  $\Lambda$ -CDM and  $\lambda_1^2 = 0 \text{ Mpc}^2$ .

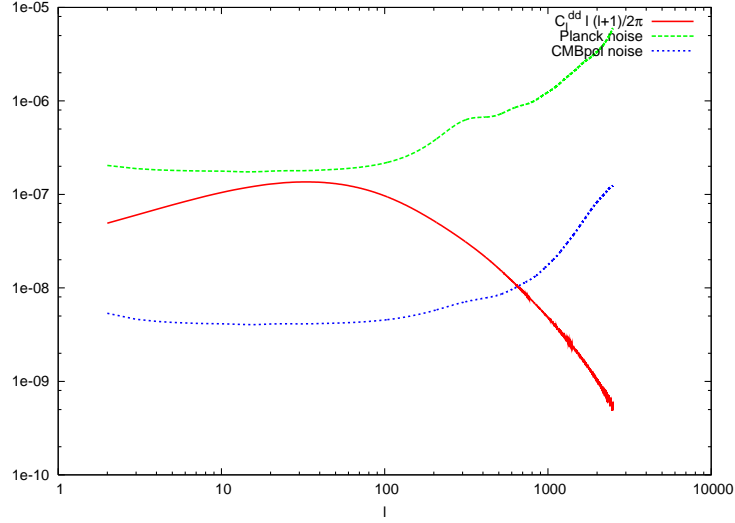


**Figure 6.7.** Planck and CMBpol noises on the  $C_\ell^{dd}$  power spectrum.

As we did above we perform a Monte Carlo Markov Chain analysis based on the publicly available package `cosmomc` [90] with a convergence diagnostic using the Gelman and Rubin statistics.

In order to build our Weak Lensing dataset, we assume a fiducial model for the standard cosmological parameters that is the best-fit from the WMAP seven years analysis of Ref. [112] with  $\Omega_b h^2 = 0.02258$ ,  $\Omega_c h^2 = 0.1109$ ,  $n_s = 0.963$ ,  $\tau = 0.088$ ,  $A_s = 2.43 \times 10^{-9}$ ,  $\Theta = 1.0388$ .

For modified gravity parameters, we first assume a fiducial value  $\lambda_1^2 = 0 \text{ Mpc}^2$  and fix  $\beta_1 = 1.33$  and  $s = 4$  to test the constraints achievable on the  $f(R)$  model. We then repeat the analysis allowing  $\beta_1$  and  $s$  to vary. Furthermore, to investigate the ability of the combination of Planck and Euclid data to detect an hypothetical modified gravity scenario, we study a model with fiducial  $\lambda_1^2 = 300 \text{ Mpc}^2$  leaving  $\lambda_1^2$ ,  $\beta_1$  and  $s$  as free variable parameters allowing them to vary in the ranges  $0 \leq \lambda_1^2 \leq 10^6$ ,  $0.1 \leq \beta_1 \leq 2$  and  $1 \leq s \leq 4$ . Finally, we analyse a dataset with a fiducial value  $\lambda_1^2 = 300 \text{ Mpc}^2$  but wrongly assuming a  $\Lambda$ CDM scenario with  $\lambda_1^2 = 0 \text{ Mpc}^2$ . This will let us to investigate the bias introduced on cosmological parameter inference from a wrong assumption about the gravity model.

In Table 6.7 we show the MCMC constraints at 68% c.l. for the  $f(R)$  case for Planck alone and Planck combined with Euclid. For this last case we also fit the data fixing  $\lambda_1^2$  to 0, thus performing a standard analysis in a General Relativity framework, in order to show the importance of the degeneracies introduced by  $\lambda_1^2$  on the other cosmological parameters errors. The parameters mostly correlated with modified gravity are  $H_0$  and  $\Omega_c h^2$  (see also Figure 6.8) because these parameters strongly affect the lensing convergence power spectrum as well as  $\lambda_1^2$  through  $P(k, z)$ . As expected in fact, when assuming General Relativity we find strong improvements on the errors on these parameters for the combination Planck+Euclid in comparison to the varying  $\lambda_1^2$  analysis. We note that the constraints on the standard cosmological parameters are in good agreement with those reported in [113].

	Planck	Planck+Euclid	
Fiducial: Model: Parameter	$\lambda_1^2 = 0$ varying $\lambda_1^2$	$\lambda_1^2 = 0$ varying $\lambda_1^2$	$\lambda_1^2 = 0$ fixed $\lambda_1^2$
$\Delta(\Omega_b h^2)$	0.00013	0.00011	0.00010
$\Delta(\Omega_c h^2)$	0.0010	0.00073	0.00057
$\Delta(\theta_s)$	0.00027	0.00025	0.00023
$\Delta(\tau)$	0.0041	0.0030	0.0026
$\Delta(n_s)$	0.0031	0.0029	0.0027
$\Delta(\log[10^{10} A_s])$	0.013	0.0091	0.0091
$\Delta(H_0)$	0.50	0.38	0.29
$\Delta(\Omega_\Lambda)$	0.0050	0.0040	0.0031
$\lambda_1^2 (\text{Mpc}^2)$	$< 2.42 \times 10^4$	$< 2.9 \times 10^2$	—

**Table 6.7.** 68% c.l. errors on cosmological parameters. Upper limits on  $\lambda_1^2$  are 95% c.l. constraints. In the third column we show constraints on the cosmological parameters when fitting the data assuming General Relativity, i.e. fixing  $\lambda_1^2 = 0 \text{ Mpc}^2$ .

In Figure 6.8 we show the 68% and 95% confidence level 2-D likelihood contour plots in the  $\Omega_m - \lambda_1^2$ ,  $H_0 - \lambda_1^2$  and  $n_s - \lambda_1^2$  planes, for Planck on the left (blue) and Planck+Euclid on the right (red). As one can see the inclusion of Euclid data can improve constraints on the standard cosmological parameters from a 10% to a 30%, with the most important improvements on the dark matter physical density and the Hubble parameter to which the weak lensing is of course very sensitive as showed in Section 4.2.2. Concerning modifications to gravity, Euclid data are decisive to constrain  $\lambda_1^2$ , improving of two order of magnitude the 95% c.l. upper limit, thanks to the characteristic effect of the modified theory of gravity on the growth of structures.

As stated above a big advantage of future surveys is the possibility to reconstruct tomographically the matter distribution. We repeated the analysis considering hence also a tomographic survey, splitting the galaxy distribution in three redshift bins; this way, as shown in Table 6.8, we obtain a  $\approx 30\%$  improvement on constraints, confirming the importance of tomography for future data analysis.

Nevertheless in [107] we are focusing on the relative improvement achievable with Euclid data with respect to Planck data alone, rather than on the absolute uncertainty on the parameters. Indeed we are not taking into account several systematic effects (such as PSF or intrinsic alignment) that may weaken constraints. Hence, we choose to use the non-tomographic analysis as a conservative estimation of the constraints.

Furthermore we also performed the analysis with a different median redshift ( $\bar{z}=1.5$ ) in order to check how possible degeneracies between  $\bar{z}$  and other parameters may affect the results. These results are also shown in Table 6.9 and they are very close to the results obtained with  $\bar{z} = 1$ ; thus the assumption of  $\bar{z} = 1$  should not affect the analysis.

Moreover, when analyzing the  $f(R)$  mock datasets with  $\lambda_1^2 = 300 \text{ Mpc}^2$  as fidu-

Parameter	Planck+Euclid	
	No tomography	with tomography
$\Delta(\Omega_b h^2)$	0.00011	0.00010
$\Delta(\Omega_c h^2)$	0.00073	0.00063
$\Delta(\theta_s)$	0.00025	0.00024
$\Delta(\tau)$	0.0030	0.0026
$\Delta(n_s)$	0.0029	0.0021
$\Delta(\log[10^{10} A_s])$	0.0091	0.007
$\Delta(H_0)$	0.38	0.33
$\Delta(\Omega_\Lambda)$	0.0040	0.0035
$\lambda_1^2(\text{Mpc}^2)$	$< 2.9 \times 10^2$	$< 2.02 \times 10^2$

**Table 6.8.** 68% c.l. errors on cosmological parameters and upper limits (at 95% c.l.) on  $\lambda_1^2$  with and without tomographic survey.

Parameter	Planck+Euclid	
	$\bar{z} = 1$	$\bar{z} = 1.5$
$\Delta(\Omega_b h^2)$	0.00011	0.00012
$\Delta(\Omega_c h^2)$	0.00073	0.00076
$\Delta(\theta_s)$	0.00025	0.00025
$\Delta(\tau)$	0.0030	0.0032
$\Delta(n_s)$	0.0029	0.0029
$\Delta(\log[10^{10} A_s])$	0.0091	0.009
$\Delta(H_0)$	0.38	0.40
$\Delta(\Omega_\Lambda)$	0.0040	0.0042
$\lambda_1^2(\text{Mpc}^2)$	$< 2.9 \times 10^2$	$< 2.67 \times 10^2$

**Table 6.9.** 68% c.l. errors on cosmological parameters and upper limits (at 95% c.l.) on  $\lambda_1^2$  using  $\bar{z} = 1$  and  $\bar{z} = 1.5$ .

	Planck+Euclid	Planck+Euclid	Fiducial values
Model: Parameter	$\lambda_1^2 = 0$	varying $\lambda_1^2$	
$\Omega_b h^2$	$0.022326 \pm 0.000096$	$0.02259 \pm 0.00012$	0.02258
$\Omega_c h^2$	$0.1126 \pm 0.00055$	$0.11030 \pm 0.00083$	0.1109
$\theta_s$	$1.0392 \pm 0.00023$	$1.0395 \pm 0.00025$	1.0396
$\tau$	$0.0775 \pm 0.0024$	$0.08731 \pm 0.0029$	0.088
$n_s$	$0.9592 \pm 0.0027$	$0.9636 \pm 0.0029$	0.963
$H_0$	$69.94 \pm 0.27$	$71.20 \pm 0.42$	71.0
$\Omega_\Lambda$	$0.724 \pm 0.003$	$0.738 \pm 0.005$	0.735
$\sigma_8$	$0.8034 \pm 0.0008$	$0.8245 \pm 0.0039$	0.8239

**Table 6.10.** best fit value and 68% c.l. errors on cosmological parameters for the case with a fiducial model  $\lambda_1^2 = 300$  fitted with a  $\Lambda$ CDM model where  $\lambda_1^2 = 0$  is assumed.

cial model, assuming  $\lambda_1^2 = 0 \text{ Mpc}^2$  we found a consistent bias in the recovered best fit value of the cosmological parameters due to the degeneracies between  $\lambda_1^2$  and the other parameters. As it can be seen from the comparison of Figures 6.8 and



Figures 6.9 and from Table 6.10 the shift in the best fit values is, as expected, along the degeneracy direction of the parameters with  $\lambda_1^2$ , for example for  $n_s$ ,  $H_0$  and  $\Omega_m$ . These results show that for an even small modifications to gravity, the best fit values recovered by wrongly assuming General Relativity are more than 68% c.l. (for some parameters at more than 95% c.l.) away from the correct fiducial values, and may cause an underestimation of  $n_s$  and  $H_0$  ( $\sim 1 - \sigma$  away from fiducial value), and of  $\sigma_8$  ( $\sim 5 - \sigma$ ). More generally, as shown in table 6.10, all parameters are affected.

We conclude, hence, that a future analyses of high precision data from Euclid and Planck need to consider possible deviations from General Relativity in order to do not bias the constraints on the cosmological parameters.

We also perform an analysis allowing  $\beta_1$  and  $s$  to vary; in this way we can constrain not only  $f(R)$  theories but also more general scalar-tensor models, adding to the standard parameter set the time variation of the new gravitational interaction  $s$  and the coupling with matter  $\beta_1$ .

We perform this analysis assuming as a fiducial model a  $f(R)$  theory with  $\lambda_1^2 = 3.0 \times 10^4 \text{ Mpc}^2$  and  $\beta_1 = 4/3$ .

Fiducial: Parameter	Planck $\lambda_1^2 = 3.0 \times 10^4$	Planck+Euclid $\lambda_1^2 = 3.0 \times 10^4$
$\Delta(\Omega_b h^2)$	0.00013	0.00011
$\Delta(\Omega_c h^2)$	0.0011	0.00082
$\Delta(\theta_s)$	0.00026	0.00025
$\Delta(\tau)$	0.0043	0.0040
$\Delta(n_s)$	0.0033	0.0029
$\Delta(\log[10^{10} A_s])$	0.014	0.011
$\Delta(H_0)$	0.54	0.40
$\Delta(\Omega_\Lambda)$	0.0060	0.0045
$\Delta(\beta_1)$	0.13	0.038
$\lambda_1^2$	unconstrained	unconstrained
$s$	unconstrained	unconstrained

**Table 6.11.** 68% c.l. errors on cosmological parameters and  $\beta_1$ . We do not show limits on  $\lambda_1^2$  and  $s$  because this kind of analysis does not allow to constrain them (see text).

In Table 6.11 we report the 68% c.l. errors on the standard cosmological parameters, plus the coupling parameter  $\beta_1$ . Performing a linear analysis, with a fiducial value of  $\lambda_1^2 = 3 \times 10^4$ , we obtain constraints on  $\beta_1$  with  $\Delta(\beta_1) = 0.038$  at 68% c.l. and therefore potentially discriminating between modified theories of gravity and excluding the  $\beta_1 = 1$  case (corresponding to the standard  $\Lambda$ CDM model) at more than  $5 - \sigma$  from a combination of Planck+Euclid data (only  $2 - \sigma$  for Planck alone). The strong correlation present between  $\beta_1$  and  $\lambda_1^2$ , as can be seen in Eq.(3.66), implies that, choosing a lower  $\lambda_1^2$  fiducial value for a  $f(R)$  model, the same variation of  $\beta_1$  brings to smaller modifications of CMB power spectra and therefore we can expect weaker bounds on the coupling parameter. In order to verify this behaviour we made three analysis fixing  $s = 4$  and choosing three different fiducial values for

$\lambda_1^2$ :  $3 \times 10^2$ ,  $3 \times 10^3$  and  $3 \times 10^4$  Mpc<sup>2</sup>. The respectively obtained  $\beta_1$  68% c.l. errors are 0.11, 0.052 and 0.035, confirming the decreasing expected accuracy on  $\beta_1$  for smaller fiducial values of  $\lambda_1^2$ .

The future constraints presented in this paper are obtained using a MCMC approach. Since most of the forecasts present in literature on  $f(R)$  theories are obtained using a Fisher matrix analysis, it is useful to compare our results with those predicted by a Fisher Matrix approach. We therefore perform a Fisher Matrix analysis for Planck and Planck+Euclid (see [114, 72, 115]) assuming a  $\Lambda$ CDM fiducial model and we compare the results with those in Table 6.7 [107].

We find that for Planck alone the error on  $\lambda_1$  is underestimated by a factor  $\sim 3$  while the error is closer to the MCMC result for the Planck+Euclid case (underestimated by a factor  $\sim 1.2$ ).

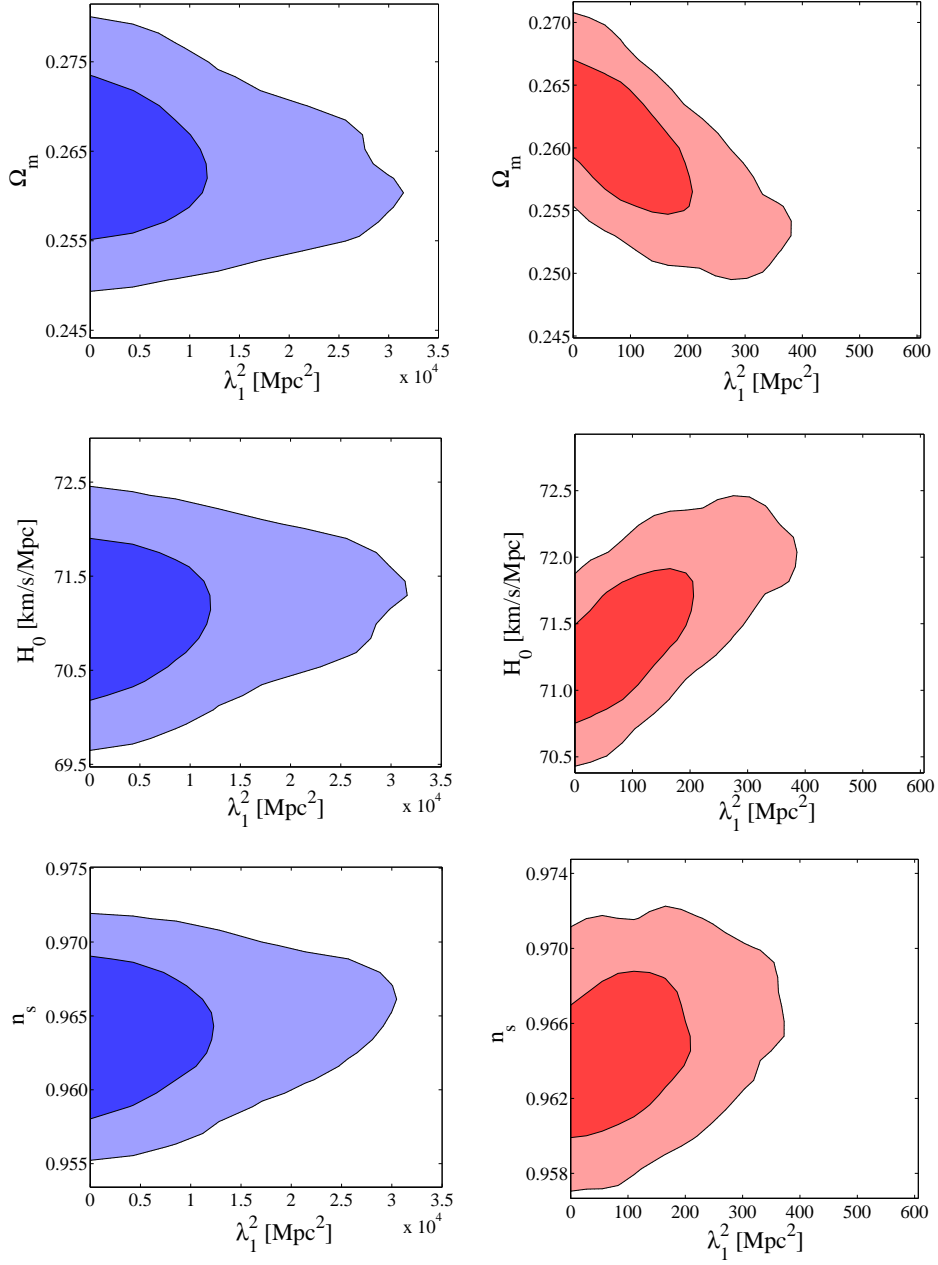


**Figure 6.8.** 2-dimensional contour plots showing the degeneracies at 68% and 95% confidence levels for Planck on the left (blue contours) and Planck+Euclid on the right (red contours). Notice different scale for abscissae.

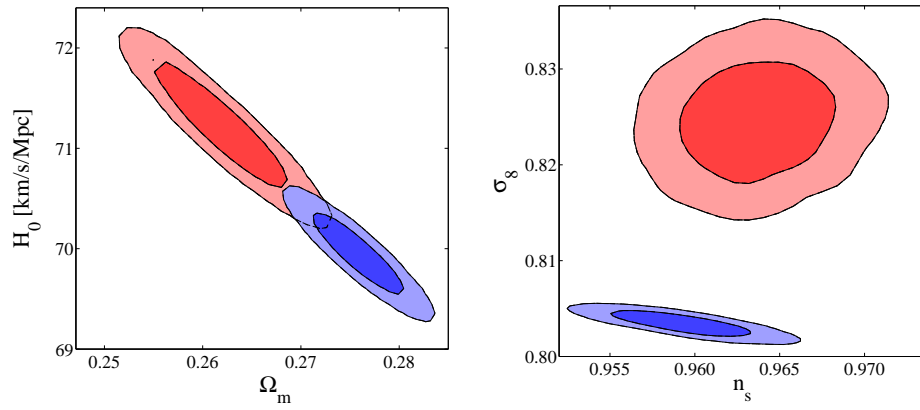


**Figure 6.9.** 2-dimensional contour plots showing the degeneracies at 68% and 95% confidence levels for Planck+Euclid assuming a  $f(R)$  fiducial cosmology with  $\lambda_1^2 = 300\text{Mpc}^2$  considering an analysis with  $\lambda_1^2$  fixed to 0 (blue countours) or allowing it to vary (red countours).

## Chapter 7

# Dark Coupling

In this Chapter we will not focus on the nature of dark energy or of other mechanisms that can produce the late time accelerated expansion; we will instead study the possibility that the dark matter and the dark energy fluids interacts with each other.

At the level of the background evolution equations, one can generally introduce a coupling between the dark matter and dark energy sectors as follows:

$$\dot{\bar{\rho}}_{dm} + 3\mathcal{H}\bar{\rho}_{dm} = a\bar{Q}, \quad (7.1)$$

$$\dot{\bar{\rho}}_{de} + 3\mathcal{H}\bar{\rho}_{de}(1+w) = -a\bar{Q}, \quad (7.2)$$

where the bars denotes background quantities,  $\bar{\rho}_{dm}(\bar{\rho}_{de})$  refers to the dark matter (dark energy) energy density, the dot indicates derivative with respect to conformal time  $d\tau = dt/a$  and  $w = \bar{P}_{de}/\bar{\rho}_{de}$  is the dark-energy equation of state ( $P$  denotes the pressure). We take  $\mathcal{H} = \dot{a}/a$  as the background expansion rate. We work in the context of a FRW metric, assuming a flat universe and pressureless dark matter  $w_{dm} = \bar{P}_{dm}/\bar{\rho}_{dm} = 0$ .  $\bar{Q}$  encodes the dark coupling and drives the background energy exchange between dark matter and dark energy. In order to deduce the evolution of the background as well as the density and velocity perturbations in coupled models, we need an expression for the energy transfer at the level of the stress-energy tensor:

$$\nabla_\mu T_{(a)}^{\mu\nu} = Q_\nu^{(a)}, \quad (7.3)$$

where  $a = \{dm, de\}$ ,  $T^{\mu\nu}$  refers to the energy-momentum tensor and  $Q_\nu^{(a)}$  is the energy-momentum transfer between the dark matter and dark energy fluids. We consider

$$Q_\nu^{(dm)} = \xi H \rho_{de} u_\nu^{(dm)} = -Q_\nu^{(de)}, \quad (7.4)$$

where  $\xi$  is a dimensionless coupling (considered constant, as well as  $w$ , in the present analysis).  $H$  and  $\rho_{de}$  refer to the total expansion rate and dark energy density, background plus perturbation, i.e.  $H = \mathcal{H}/a + \delta H$  and  $\rho_{de} = \bar{\rho}_{de} + \delta\rho_{de}$  respectively. In the previous Eqs. (7.1) and (7.2),  $\bar{Q}$  corresponds to  $\xi\mathcal{H}\bar{\rho}_{de}/a$ , see our choice of coupling in Eq. (7.4). Notice from Eq. (7.4) that  $Q_\nu^{(a)}$  has been chosen parallel to the dark matter four velocity  $u_\nu^{(dm)}$ , in order to avoid momentum transfer in the rest frame of the dark matter component [116]. For this choice of energy exchange  $Q_\nu^{(a)}$ ,

positive (negative) values of the coupling  $\xi$  will lead to lower (higher) dark matter energy densities in the past than in the uncoupled  $\xi = 0$  case. In the following, we restrict ourselves here to negative couplings and  $w > -1$ , which avoids instability problems in the dark energy perturbation equations [119].

The interacting model given by Eq. (7.4) has already been previously explored under several assumptions, see Refs. [116, 117, 118, 119]. In those works, the linear perturbation analysis did not include perturbation of the expansion rate  $\delta H$ . In the numerical analysis used here we include the new terms arising in the linear perturbation evolution due to the presence of the  $\delta H$  term. This term is quite relevant for the correct treatment of gauge invariant perturbation but it does not affect much the physical results. Details of the complete linear perturbation analysis in terms of gauge invariant variables are presented in [120], including the specification of the initial conditions which have been chosen adiabatic for all the components, as well as for the dark energy fluid. Here we briefly summarize the most relevant results of [120]. In the following, in order to lighten the notations, background quantities are not explicitly written as barred. In the synchronous gauge, the perturbation in the expansion rate reads

$$\delta H = \theta_T / (3a) + \dot{h} / (6a) \quad (7.5)$$

where  $(\rho + P)\theta_T = \sum_a (\rho_a + P_a)\theta_a$ , being  $\theta_a$  the divergence of the peculiar velocity of the different fluids and  $h$  the usual synchronous gauge metric perturbation. The linear perturbation equations including the term in  $\delta H$  are

$$\dot{\delta}_{dm} = -(\theta_{dm} + \frac{1}{2}\dot{h}) + \xi \mathcal{H} \frac{\rho_{de}}{\rho_{dm}} (\delta_{de} - \delta_{dm}) + \xi \frac{\rho_{de}}{\rho_{dm}} \left( \frac{1}{3}\theta_T + \frac{\dot{h}}{6} \right) \quad (7.6)$$

$$\dot{\theta}_{dm} = -\mathcal{H}\theta_{dm} \quad (7.7)$$

$$\begin{aligned} \dot{\delta}_{de} = & -(1+w)(\theta_{de} + \frac{1}{2}\dot{h}) - 3\mathcal{H}(\hat{c}_{sde}^2 - w) \left[ \delta_{de} + \mathcal{H}(3(1+w) + \xi) \frac{\theta_{de}}{k^2} \right] \\ & - \xi \left( \frac{1}{3}\theta_T + \frac{\dot{h}}{6} \right) \end{aligned} \quad (7.8)$$

$$\dot{\theta}_{de} = -\mathcal{H} \left( 1 - 3\hat{c}_{sde}^2 - \frac{\hat{c}_{sde}^2 + 1}{1+w} \xi \right) \theta_{de} + \frac{k^2}{1+w} \hat{c}_{sde}^2 \delta_{de} - \xi \mathcal{H} \frac{\theta_{dm}}{1+w}, \quad (7.9)$$

where  $\delta_a \equiv \delta\rho_a/\rho_a$ ,  $\theta_a \equiv \partial_i v_a^i$  is the divergence of the fluid proper velocity  $v_a^i$  and  $\theta_T$  is defined as  $(\rho + P)\theta_T = \sum_a (\rho_a + P_a)\theta_a$ . In [120] is also shown that adiabatic initial conditions for the matter and radiation components automatically imply adiabatic initial conditions for dark energy, alike to the case for tracking scalar quintessence or those obtained for dark energy-dark matter couplings which do not depend explicitly on the Hubble rate. We have therefore used in our numerical analysis adiabatic initial conditions for all the fluids.

For the numerical analysis presented here, we have modified the publicly available CAMB code [121], taking into account the presence of the dark coupling in both the background and the linear perturbation equations.

## 7.1 Observational Signatures

As for modified gravity, also Dark Coupling model are better constrained studying the evolution of matter perturbations. In fact, as we saw in the previous Section, the introduction of a Dark Energy-Dark Matter coupling changes the evolution of these perturbations with respect to the  $\Lambda$ CDM model.

Therefore we can think to exploit the observables introduced in Section 4.2, i.e. CMB temperature, polarization and lensing deflection power spectra and weak lensing. In fact, as we can see in Fig. 7.1, different values of the coupling parameter  $\xi$  brings to different theoretical spectra for the observables that we considered.

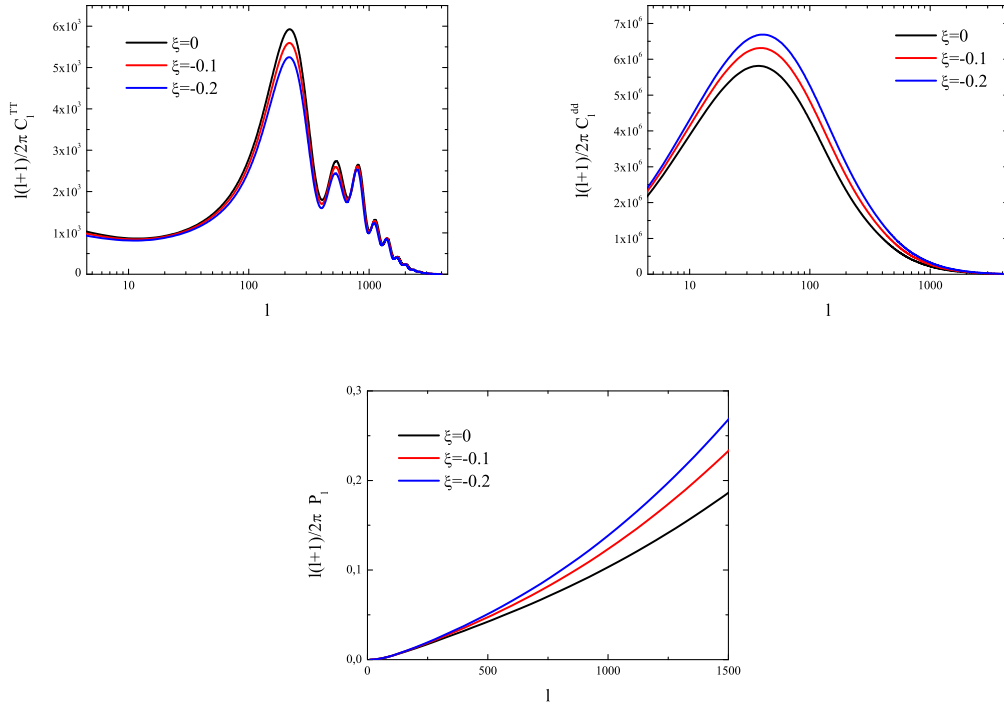


**Figure 7.1.** Dependence on the coupling parameter  $\xi$  for CMB temperature (top left panel), CMB lensing deflection (top right panel) and convergence (bottom panel) power spectra. All other parameters are fixed to the WMAP7  $\Lambda$ CDM best fit values.

The complementarity of CMB and weak lensing measurements is particularly useful in order to constrain coupled dark energy as we can see from Fig. 7.2, where we report degenerate CMB angular power spectra and predictions for the same models for the CMB lensing and converge spectra. As we can see, while it is possible to choose models that can produce identical CMB angular power spectra, the same models have different CMB lensing and convergence spectra. CMB angular power spectra observations determine the angular diameter distance to the last scattering surface: there will always be a choice of the coupling  $\xi$  and of the physical dark matter energy density which will reproduce the expectations for a  $\Lambda$ CDM model. This effect is due to the fact that CMB constraints the amount of dark matter at redshift  $\sim 1000$ . In the presence of a negative dark coupling, the energy flows from

dark matter to dark energy, and the present dark matter energy density is smaller. Therefore  $\Omega_c h^2$  is strongly correlated with the coupling  $\xi$  and it is difficult to break their degeneracy if one uses CMB primary anisotropy information only. However, in the context of interacting cosmologies, the matter overdensities are being enhanced as the background dark matter density is evaporating into dark energy: the effect of a smaller dark matter density is compensated for large scale structures by a larger growth of the dark matter perturbation (see e.g. [122]). Measuring the modified dark matter growth factor via future galaxy surveys in some interacting cosmologies could be extremely challenging, since, for some choices of the interacting term, the growth equations for the dark matter and for the baryon components are different. Galaxy surveys are likely to measure the baryon peculiar velocities, while dark matter overdensities will be biased and not directly measured [123]. Lensing probes, however, could offer the best tool since the lensing potential tests dark matter directly, and alleviate the degeneracy among coupled and uncoupled universes from CMB primary anisotropy measurements.

In fact, lensing observables are sensitive to the dark matter density perturbation times the dark matter energy density, and the value of the former product can be different for coupled and uncoupled models even if they are degenerate from the point of view of CMB observations [124]. A combination of CMB with weak lensing measurement is therefore decisive in constraining coupled cosmologies.

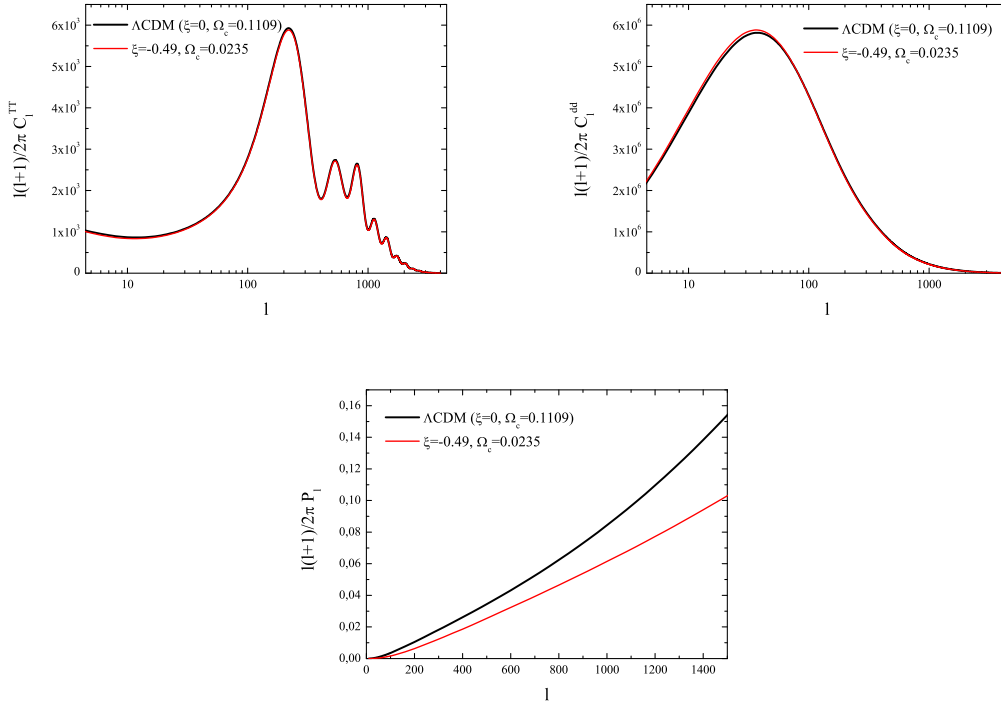


**Figure 7.2.** Temperature (top left panel), lensing deflection (top right panel) and convergence (bottom panel) power spectra produced in the case of standard  $\Lambda$ CDM model with  $\xi = 0$  (solid line) and with a model with  $\xi = -0.49$  and  $\Omega_c h^2 = 0.0235$ .



## 7.2 Constraints on Dark Coupling

### CMB results

In [125] we evaluate the achievable constraints on the coupling parameter  $\xi$  by a Monte Carlo Markov Chain analysis of future mock CMB datasets. The analysis method we adopt here is based on the publicly available Markov Chain Monte Carlo package `cosmomc` [90] with a convergence diagnostic using the Gelman and Rubin statistics.

For the numerical analysis presented here and in next Section, we have modified the publicly available CAMB code [121], taking into account the presence of the dark coupling in both the background and the linear perturbation equations.

We sample the following seven-dimensional set of cosmological parameters, adopting flat priors on them: the baryon and cold dark matter densities  $\Omega_b h^2$  and  $\Omega_c h^2$ , the ratio of the sound horizon to the angular diameter distance at decoupling  $\theta_s$ , the scalar spectral index  $n_s$ , the overall normalization of the spectrum  $A_s$  at  $k = 0.002 \text{ Mpc}^{-1}$ , the optical depth to reionization  $\tau$ , and, finally, the coupling parameter  $\xi$ .

As we did for modified gravity, we create full mock CMB datasets (temperature, E-polarization mode and lensing deflection field) with noise properties consistent with Planck [87] and CMBpol/EPIC [99] experiments (see Table 6.3 for their specifications). The fiducial model is chosen to be the best-fit from the WMAP analysis [126] with  $\Omega_b h^2 = 0.0227$ ,  $\Omega_c h^2 = 0.113$ ,  $n_s = 0.963$ ,  $\tau = 0.09$  and  $\xi = 0$ , fixing  $w = -0.9$  for our numerical calculations.

The experimental noise for both Planck and CMBpol/EPIC are obtained as in Section 6.2.1.

Experiment Parameter	Planck	Planck Lens	CMBpol/EPIC	CMBpol/EPIC Lens
$\Delta(\Omega_b h^2)$	0.00015	0.00012	0.00004	0.00003
$\Delta(\Omega_c h^2)$	0.0297	0.0296	0.0295	0.016
$\Delta(\theta_s)$	0.00229	0.00215	0.00216	0.00102
$\Delta(\tau)$	0.0047	0.0041	0.0022	0.0021
$\Delta(n_s)$	0.0037	0.0029	0.0018	0.0013
$\Delta(\log[10^{10} A_s])$	0.016	0.012	0.005	0.004
$\Delta(H_0)$	2.34	2.16	2.17	1.33
$\Delta(\Omega_\Lambda)$	0.064	0.061	0.062	0.038
$\xi$	$> -0.59$	$> -0.54$	$> -0.56$	$> -0.34$

**Table 7.1.** 68% c.l. errors on cosmological parameters. Upper limits on  $\xi$  are 95% c.l. constraints.

Table 7.1 summarizes the errors from Planck and CMBpol/EPIC future data on the main cosmological parameters when a coupling  $\xi$  among the dark energy and dark matter fluids is introduced in the model. Notice that the errors on the cosmological parameters which are degenerate with  $\xi$  are larger than the errors that one would get for these parameters within a standard cosmology, where  $\xi = 0$  (see

Experiment Parameter	Planck Lens	CMBpol/EPIC Lens
$\Delta(\Omega_b h^2)$	0.00013	0.00003
$\Delta(\Omega_c h^2)$	0.0010	0.0003
$\Delta(\theta_s)$	0.00026	0.00005
$\Delta(\tau)$	0.0042	0.0022
$\Delta(n_s)$	0.0031	0.0014
$\Delta(\log[10^{10} A_s])$	0.013	0.005
$\Delta(H_0)$	0.53	0.12
$\Delta(\Omega_\Lambda)$	0.005	0.001

**Table 7.2.** 68% c.l. errors on cosmological parameters from Planck and CMBpol/EPIC with lensing extraction in the standard non interacting case ( $\xi = 0$ ).

Tab. 7.2). In particular, in the case of  $\Omega_c h^2$ ,  $H_0$ ,  $\Omega_\Lambda$  and  $\theta_s$ , the errors we obtain here are one order of magnitude larger than the ones obtained with  $\xi = 0$ . For comparison, we show in Tab. 7.1 the parameter constraints both with and without lensing extraction. The cosmological parameter constraints from CMBpol/EPIC mock data are stronger than those coming from future Planck data when the CMB lensing signal is exploited. The reason for that is because the CMBpol/EPIC experiment is expected to reduce the noise in the CMB lensing extraction.

As an example, a  $\Lambda$ CDM universe with  $\Omega_c h^2 = 0.113$  and a coupled model with  $\xi = -0.4$  and  $\Omega_c h^2 = 0.0463$  would be degenerate if only the CMB unlensed temperature spectrum is used since they have identical spectra, albeit with different cold dark matter densities, since a more negative coupling can be compensated with a lower  $\Omega_c h^2$ .

Neither Planck nor CMBpol/EPIC data will be able to distinguish among coupled and uncoupled models using only primary CMB anisotropy data. However, these two models predict distinguishable lensing potential spectra, as previously discussed, and, while the Planck experiment will not have enough sensitivity to distinguish coupled versus uncoupled models, the CMBpol/EPIC experiment, with a reduced noise on the CMB lensing extraction, will be able to better test coupled models, as it can be seen in Table 7.1.

Figures (7.3) and (7.4) depict the 68% and 95% confidence level contours combining the five most correlated parameters arising from a fit to mock Planck and CMBpol/EPIC data respectively, without considering CMB lensing extraction. We can see that the cold dark matter density  $\Omega_c h^2$ , the Hubble constant  $H_0$ , the cosmological constant  $\Omega_\Lambda$ , the sound horizon angle  $\theta_s$  and the coupling  $\xi$  are all strongly correlated and neither Planck nor CMBpol/EPIC data will be able to break these degeneracies. Notice as well that, despite the technological advances of CMBpol/EPIC, the error on the cosmological parameters achieved by the Planck experiment will not be further improved by CMBpol/EPIC data if no lensing signal is considered.

Figures (7.5) and (7.6) show the 68% and 95% confidence level contours combining the five most correlated parameters arising from a fit to Planck and CMBpol/EPIC future data respectively, considering the information from CMB lensing. Notice that the inclusion of lensing power spectrum improves drastically the CMBpol/EPIC

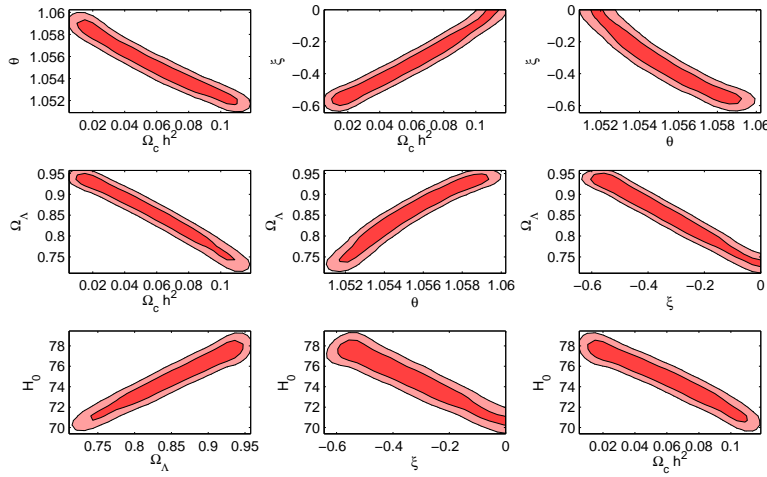


**Figure 7.3.** The panels show the 68% and 95% confidence level contours combining the five most correlated parameters ( $\Omega_c h^2$ ,  $\theta_s$ ,  $H_0$ ,  $\Omega_\Lambda$  and  $\xi$ ) arising from a fit to mock Planck data without including lensing extraction in the analysis.

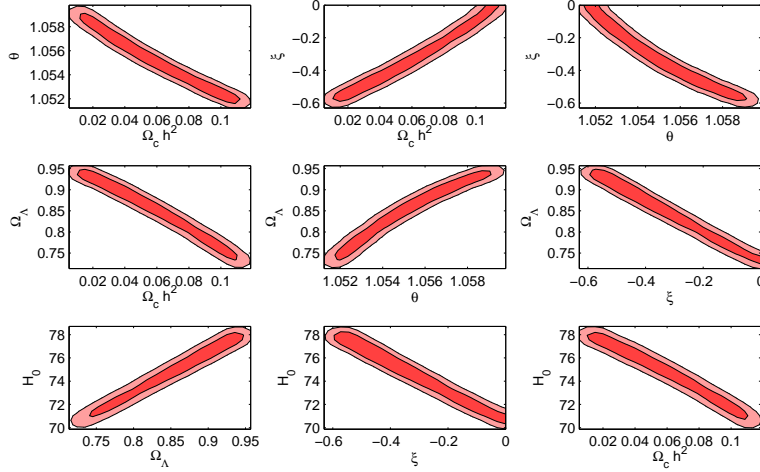


**Figure 7.4.** The panels show the 68% and 95% confidence level contours combining the five most correlated parameters ( $\Omega_c h^2$ ,  $\theta_s$ ,  $H_0$ ,  $\Omega_\Lambda$  and  $\xi$ ) arising from a fit to mock EPIC data without including lensing extraction in the analysis.

constraints. However, the addition of CMB lensing information does not change Planck results. This is due to the fact that the lensing noise for CMBpol/EPIC is significantly lower than for the Planck experiment, as we can see in Fig.6.7, and therefore CMBpol/EPIC data would be able to reject models that otherwise would be accepted by Planck.

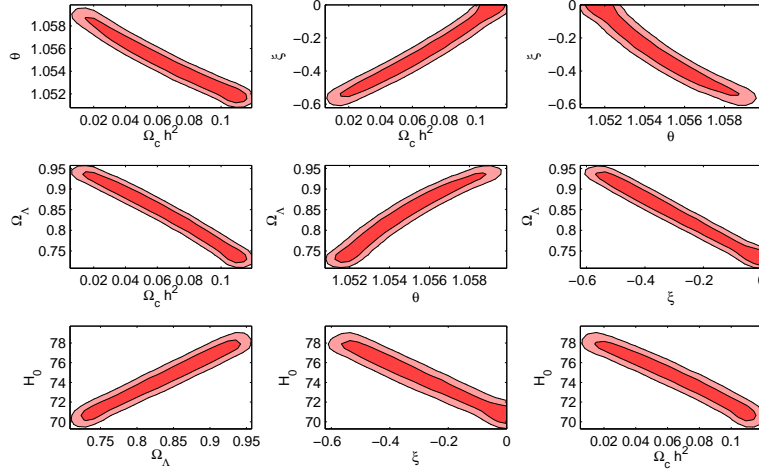


**Figure 7.5.** The panels show the 68% and 95% confidence level contours combining the five most correlated parameters ( $\Omega_c h^2$ ,  $\theta_s$ ,  $H_0$ ,  $\Omega_\Lambda$  and  $\xi$ ) arising from a fit to mock Planck data including lensing extraction in the analysis.

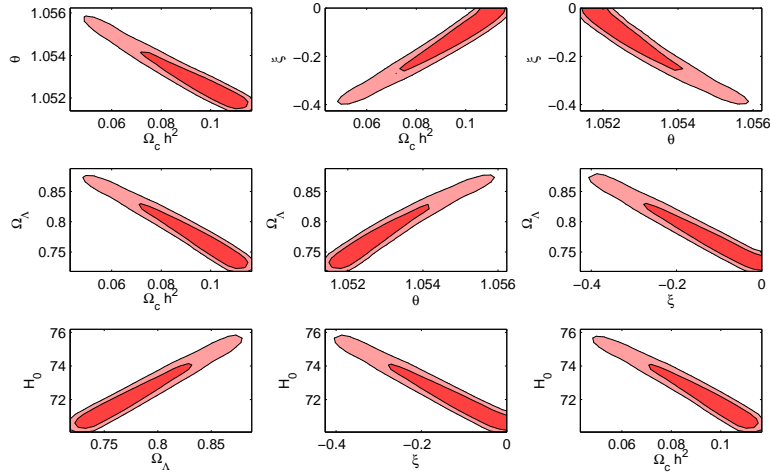


**Figure 7.6.** The panels show the 68% and 95% confidence level contours combining the five most correlated parameters ( $\Omega_c h^2$ ,  $\theta_s$ ,  $H_0$ ,  $\Omega_\Lambda$  and  $\xi$ ) arising from a fit to mock EPIC data including lensing extraction in the analysis.

### Weak Lensing results

In [127] we include weak lensing data and we perform two different analyses. First, we compute the expected constraints on the coupling parameter  $\xi$  from Planck and Euclid data, comparing the results with the limits arising from Planck and LSST data [128]. Secondly, we investigate the effects of a wrong assumption about the interaction between dark matter and dark energy on the values of the cosmological

parameters: we generate a dataset with a non-zero  $\xi$  fiducial value but analyze the data assuming that there is no coupling between the dark components ( $\xi = 0$ ). We perform a MCMC analysis based on the publicly available package `cosmomc` [90] with a convergence diagnostic using the Gelman and Rubin statistics. In principle, since we are dealing only with statistical uncertainties on the observables and neglecting any systematic effects, we could perform a simple *Fisher matrix analysis*. The Fisher matrix method offers the advantage of being less time-consuming and to reduce the forecast process to a series of matrices operations. Nevertheless, we prefer to conduct a MCMC exploration of the parameter space to avoid possible numerical instabilities that may arise in the computation of the derivatives with respect to the coupling parameter  $\xi$  (note that a fiducial model  $\xi = 0$  would force the computation of one-side derivatives due to the restriction  $\xi < 0$ ). Moreover the gaussian approximation implied by the Fisher matrix is reliable for the standard cosmological parameters but may become risky for non-standard parameters. We sample the same set of cosmological parameters as in the CMB only analysis, but here the fiducial model for the standard cosmological parameters is the best-fit from the WMAP seven year data analysis [112] with  $\Omega_b h^2 = 0.02258$ ,  $\Omega_c h^2 = 0.1109$ ,  $n_s = 0.963$ ,  $\tau = 0.088$ ,  $A_s = 2.43 \times 10^{-9}$  and  $\Theta = 1.0388$ . For the coupling parameter we first assume a fiducial value  $\xi = 0$  to test the constraints achievable on the coupling model. Finally, we analyse a dataset with a fiducial value  $\xi = -0.1$  assuming (wrongly) a  $\Lambda$ CDM scenario with  $\xi = 0$ , with Planck and Euclid forecasted data. This exercise will allow us to investigate the bias introduced on cosmological parameter inference from a wrong assumption about the coupling model.

In Table 7.3 we show the MCMC constraints at 68% c.l. for the coupled universe from Planck data alone and from Planck data combined with Euclid data. For this last case we also fit the data fixing  $\xi$  to 0, thus performing a standard analysis in a universe where dark matter and dark energy are not interacting, in order to show the importance of the degeneracies introduced by the presence of a coupling  $\xi$  on the other cosmological parameters errors. There is a very high level of correlation among the dimensionless coupling  $\xi$  and the parameters  $H_0$  and  $\Omega_c h^2$  in the Planck analysis (see also Figs. 7.8 and 7.9). When Planck and Euclid data are combined, the degeneracy between  $\xi$  and  $H_0$  is broken, leading to a much better constrain on the coupling parameter  $\xi$  than when using CMB data alone [125], as one can notice from Table 7.3, Fig. 7.8 and Fig. 7.9.

However, the degeneracy between  $\xi$  and  $\Omega_c h^2$  is still not completely broken by the combination of Planck and Euclid, thus it will be possible to further improve the constraints on  $\xi$  with independent measurements of the dark matter density. We also note that the constraints on the standard cosmological parameters are in good agreement with those reported in [113].

The combination of galaxy weak lensing data and CMB data is decisive to improve the constraints on coupled models for the higher sensitivity of Euclid to the parameters that affect the growth of structure, namely the Hubble parameter and the dark matter density. In fact, as shown in [125], an improved CMB experiment could strengthen the constraints on  $\xi$  improving both the lensing extraction and the measurement of the polarization power spectrum but the constraints from CMB data alone, even from future surveys, remain about one order of magnitude weaker than those achievable from the combination with weak lensing data. Moreover, as stated above, future surveys like Euclid will be able to tomographically reconstruct

	Planck		Planck+Euclid	
Model Parameter	Varying $\xi$	$\xi = 0$	Varying $\xi$	$\xi = 0$
$\Delta(\Omega_b h^2)$	0.00013	0.00013	0.00010	0.00010
$\Delta(\Omega_c h^2)$	0.0299	0.0010	0.0024	0.00055
$\Delta(\theta_s)$	0.0023	0.00026	0.00027	0.00023
$\Delta(\tau)$	0.0042	0.0042	0.0026	0.0026
$\Delta(n_s)$	0.0030	0.0031	0.0029	0.0027
$\Delta(\log[10^{10} A_s])$	0.013	0.013	0.0097	0.0093
$\Delta(H_0)$	2.28	0.43	0.29	0.27
$\Delta(\Omega_\Lambda)$	0.0614	0.0050	0.0062	0.0026
$\xi$	$> -0.56$	—	$> -0.04$	—

**Table 7.3.** 68% c.l. errors on cosmological parameters. Upper limits on  $\xi$  are 95% c.l. constraints.

the matter distribution with a consequent gain of a three-dimensional information that is generally not accessible with CMB lensing. Exploiting this possibility would improve the constraints, but, as already pointed out in [107], the non tomographic analysis we performed here can be thought as a conservative estimation of the constraints as we are not including the systematic effects that may affect a galaxy weak lensing survey.

Table 7.4 contains both the results from the combination of Planck and Euclid data and those from the combination of Planck and LSST. Notice that the results are quite similar. However, the slightly better constraints on  $\xi$  from the Planck plus Euclid combination leads to a better measurement of the cold dark matter content of the universe than the one performed by Planck plus LSST data (see also Fig. 7.7). Moreover, the difference between Planck+Euclid and Planck+LSST results would be bigger if systematic effects are included, as LSST, being a ground based survey, will be more affected by these.

	Planck+Euclid	Planck+LSST
Parameter		
$\Delta(\Omega_b h^2)$	0.00010	0.00010
$\Delta(\Omega_c h^2)$	0.0024	0.0026
$\Delta(\theta_s)$	0.00027	0.00028
$\Delta(\tau)$	0.0026	0.0027
$\Delta(n_s)$	0.0029	0.0029
$\Delta(\log[10^{10} A_s])$	0.0097	0.010
$\Delta(H_0)$	0.29	0.29
$\Delta(\Omega_\Lambda)$	0.0062	0.0065
$\xi$	$> -0.04$	$> -0.06$

**Table 7.4.** 68% c.l. errors on cosmological parameters. Upper limits on  $\xi$  are 95% c.l. constraints.

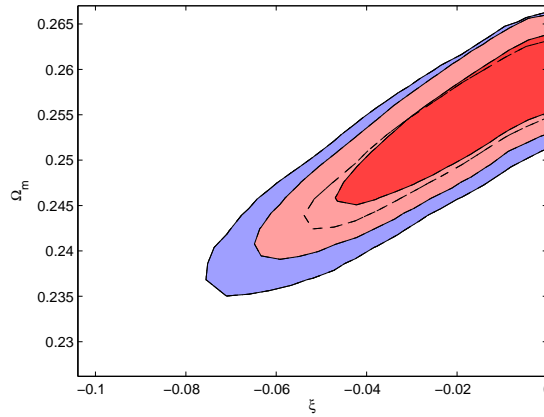


**Figure 7.7.** 2-D constraints on  $\xi$  and  $\Omega_m$  using Planck and LSST data (blue contours) and Planck and Euclid data (red contours).

In addition, we have also (wrongly) fitted a mock dataset with  $\xi = -0.1$  to a non interacting cosmology in which the dimensionless coupling vanishes ( $\xi = 0$ ). From this exercise we find a consistent bias in the recovered best fit value of the cosmological parameters due to the strong degeneracies among  $\xi$  and both the Hubble constant  $H_0$  and the matter energy density  $\Omega_m$  parameters, see Tab.7.5. Note, from the results depicted in Figs. 7.8, 7.9 and 7.10 and also from the results in Tab. 7.5 that the shift in the best fit values is, as expected, along the direction of the degeneracy of  $\xi$  with these parameters. These results show that even for a small value of  $\xi$ , the best fit values recovered by wrongly assuming that there is no dark coupling are more than 68% c.l. (for some parameters at more than 95% c.l.) away from the correct fiducial values, and may induce an underestimation of both  $H_0$  and  $\sigma_8$  and an overestimation of  $\Omega_c h^2$ . In the last column in Tab. 7.5 we show the difference between the *wrong* value estimated fixing  $\xi = 0$  and the fiducial value, relative to the  $1\sigma$  error: as expected the largest shifts are in the parameters that are directly involved in determining the energy momentum transfer between components, namely matter and dark energy densities and Hubble parameter. We note that also other parameters, as  $\sigma_8$  and  $n_s$ , have significant shifts.

We conclude, hence, that future analyses of high precision data from Euclid and Planck need to consider possible deviations from the minimal  $\Lambda$ CDM scenario in order to avoid biases in the measurements of the cosmological parameters.

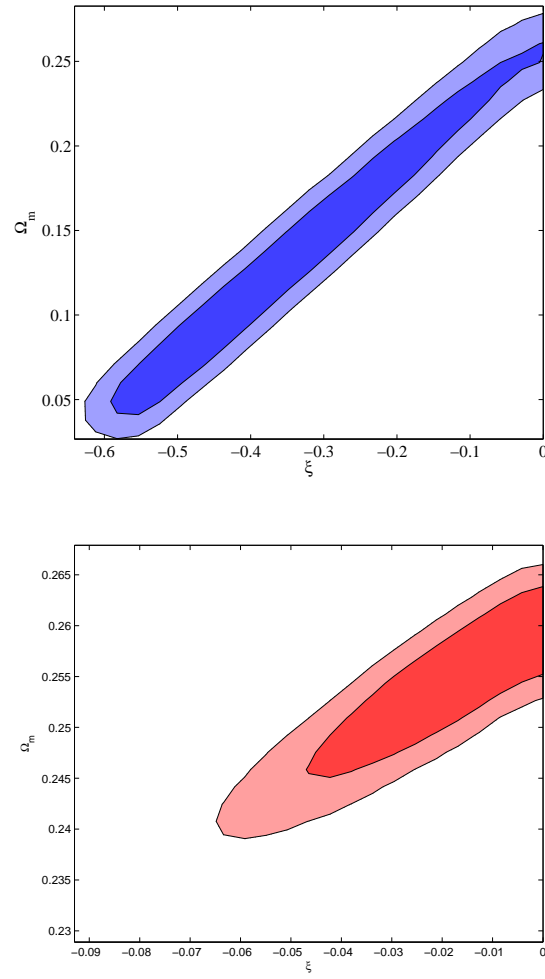


**Figure 7.8.** Top panel: 68% and 95% c.l. contours in the  $(\Omega_m, \xi)$  plane from Planck data only. Bottom panel: same as in the top panel, but for the combination of Planck plus Euclid data (note the different scale for the x-axis).



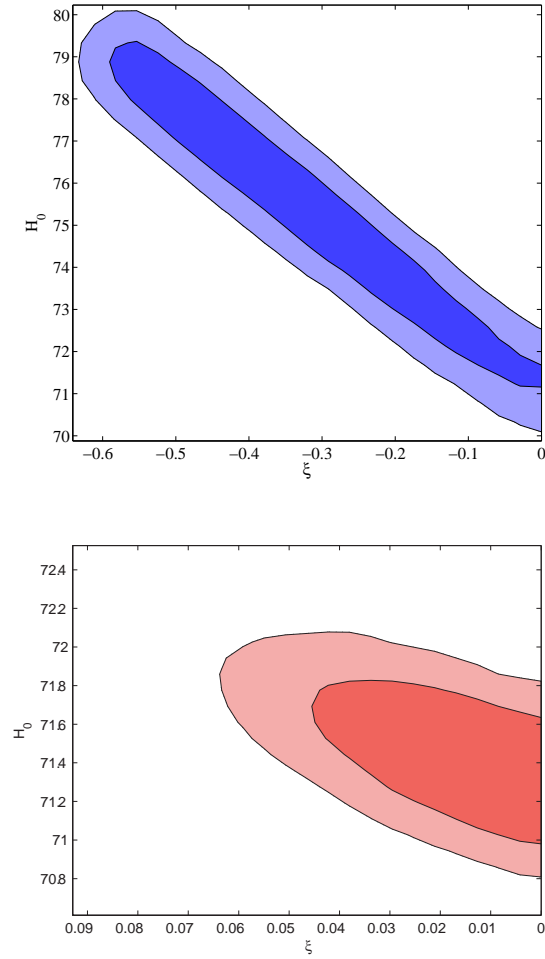


**Figure 7.9.** Top panel: 68% and 95% c.l. contours in the  $(H_0, \xi)$  plane from Planck data only. Bottom panel: same as in the top panel, but for the combination of Planck plus Euclid data (note the different scale for the x-axis).

	Planck+Euclid		Fiducial values	$ \Delta/\sigma $
Model: Parameter	$\xi = 0$	varying $\xi$		
$\Omega_b h^2$	$0.02259 \pm 0.00010$	$0.02257 \pm 0.00010$	0.02258	0.1
$\Omega_c h^2$	$0.1245 \pm 0.00061$	$0.1083 \pm 0.0024$	0.1109	22
$\tau$	$0.086 \pm 0.0029$	$0.090 \pm 0.0033$	0.088	0.7
$n_s$	$0.955 \pm 0.0014$	$0.961 \pm 0.0028$	0.963	5.7
$H_0$	$69.6 \pm 0.23$	$70.9 \pm 0.30$	71.0	6
$\Omega_\Lambda$	$0.697 \pm 0.0031$	$0.739 \pm 0.0066$	0.735	12
$\sigma_8$	$0.752 \pm 0.00044$	$0.841 \pm 0.019$	0.82	15

**Table 7.5.** Best fit values and 68% c.l. errors on cosmological parameters for the case in which a fiducial model with  $\xi = -0.1$  is fitted to a  $\Lambda$ CDM model where  $\xi = 0$  is assumed. The last column shows the absolute value of the difference between the best-fit value estimated fixing  $\xi = 0$  and the fiducial value, relative to the  $1\sigma$  error.

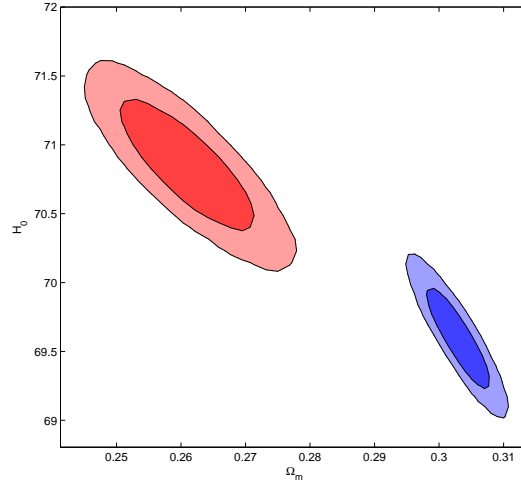


**Figure 7.10.** 68% and 95% confidence levels from Planck plus Euclid data when a fiducial cosmology with  $\xi = -0.1$  is fitted to a non interacting cosmology with  $\xi$  fixed to 0 (blue contours) or to an interacting cosmology in which  $\xi$  is allowed to vary.

## Chapter 8

# Conclusion

In this Thesis, in particular in Chapter 3, we described a particular  $f(R)$  model, the Hu and Sawicki model, that can produce a viable accelerated expansion of the Universe. We discussed its properties and its cosmological viability and described how it modifies the evolution of the equation of state parameter of Dark Energy and, therefore, the evolution of the Universe. In the same Chapter we introduced a parameterization that allows to describe deviations from General Relativity without having to assume a specific Lagrangian for gravitational interaction. This allows to theoretically predict the evolution of matter perturbations for different modified gravity models, such as  $f(R)$  and scalar-tensor theories.

In Chapter 4 we introduced many astrophysical observables that allow to constrain modified gravity models. We showed how a gravitational interaction different from the standard one will change the theoretical predictions both for background expansion observables (such as Supernovae and BAO) and for observables connected to the evolution of matter perturbations (such as CMB and weak lensing).

In Chapter 5 we focused on constraints that can be placed on the Hu and Sawicki model; at first we showed the constraints that can be obtained using only current background data and we pointed out that using just these observables it is not possible to obtain good results as these will be strongly dependent on the value of the matter content of the Universe  $\Omega_m$ . Nevertheless we compare the goodness-of-fit of this model with the standard  $\Lambda$ CDM model finding that this  $f(R)$  model fits better current data if the  $\Omega_m$  is higher or smaller than the overall best fit value.

Moreover we presented future constraints on the Hu-Sawicki modified gravity model arising from measurements of the linear growth of structure and of SNIa luminosity distances. While luminosity distance data allow for small values of  $n$ , the growth of structure data prefer higher values for this parameter. The combination of these two observables allows to tightly constrain the HS model. We have generated mock growth and luminosity distance data for a fiducial  $\Lambda$ CDM model and fitted these data in a Hu-Sawicki modified gravity scenario. The reconstructed effective dark energy equation of state is almost identical to that of a  $\Lambda$ CDM model as it is possible to see in Fig. 5.11.

In Chapter 6 instead we used current and forecasted data to constrain deviations from General Relativity using the parameterization described in Chapter 3. At first we use current CMB data alongside galaxy surveys data in order to constrain deviation from the standard  $\Lambda$ CDM ISW effect on the CMB photons and in particular to

constrain the modifications produced by  $f(R)$  theories. We then describe how it is possible to forecast data from future experiments as Planck and CMBpol/EPIC for CMB and Euclid for weak lensing. After introducing the CMB experiments and how the forecasted datasets are obtained we constrain the general parameterization for  $f(R)$  theories using CMB forecast for both Planck and CMBpol/EPIC with and without considering the lensing information contained in CMB maps; we point out how introducing the lensing deflection power spectrum in the analysis can improve the constraints on the  $\lambda_1^2$  parameter of one order of magnitude in both experiments. Furthermore we forecast weak lensing data for Euclid satellite and we show how the introduction of Euclid alongside Planck in the analysis can bring to a huge improvement on  $\lambda_1^2$ . As Planck+Euclid data are so sensitive we decided to study also the parameterization in the scalar-tensor theories case, when the free parameters are  $\beta_1$  and  $s$  in addition to  $\lambda_1^2$ ; in this case we use a fiducial  $\lambda_1^2 = 3.0 \times 10^4$  to produce our dataset, as choosing a vanishing  $\lambda_1^2$  would have made all the parameters totally unconstrained, while using this fiducial, even if  $s$  and  $\lambda_1^2$  are still unconstrained, we can obtain an error on  $\beta_1$ . Nevertheless, the constrain on this last parameter is dependent on the fiducial value of  $\lambda_1^2$  as this two parameters are strongly correlated, as can be seen in Eq.(3.66).

Therefore we can conclude from this analysis that future weak lensing surveys will be very useful to constrain modified gravity theories, thus we decided to analyze the bias introduced on the standard cosmological parameters if an  $f(R)$  Planck+Euclid dataset is analyzed wrongly assuming a  $\Lambda$ CDM cosmology; we found out that this bias is large enough for us to conclude that modified gravity scenarios will need to be considered when future weak lensing data will be analyzed.

In Chapter 7, finally, we didn't try to explain the nature of the accelerated expansion of the Universe, but we took into account a model where Dark Energy and Dark Matter are allowed to interact with each other. We explained how the perturbation observables introduced in Chapter 4 can be used to test this Dark Coupling model as different values of the coupling parameter  $\xi$  produce different theoretical predictions for CMB and weak lensing spectra. So we then constrained  $\xi$  using only CMB forecasted data for Planck and CMBpol/EPIC showing how also for this model is important to introduce the lensing deflection power spectrum in the analysis.

We then used Euclid forecasted data alongside the ones from Planck and showed how weak lensing will bring a huge improvement to the constraints that it is possible to give to coupled Universe.

Therefore we performed the same bias analysis we did for  $f(R)$  models, fitting a dataset with a fiducial non-vanishing  $\xi$  parameter with a wrongly assumed  $\Lambda$ CDM cosmology; as for the  $f(R)$  case we found out that the bias on the recovered standard cosmological parameters is large and that therefore it will be very important to consider Dark Coupling models when analyzing real future weak lensing data.

## Appendix A

# Principle of Maximum Likelihood

In this appendix we want to focus on the estimation problem, i.e. how it is possible to reconstruct the properties of a probability distribution function (PDF) starting from a limited number of observations, which constitute a random sample.

We can think of these PDF properties as unknown parameters which we want to determine; if we consider a set of  $n$  observations  $\mathbf{d} = \{d_1^{obs}, d_2^{obs}, \dots, d_n^{obs}\}$  of the variable  $X$  and a set of  $p$  parameters  $\boldsymbol{\theta} = \{\theta_1^{obs}, \theta_2^{obs}, \dots, \theta_p^{obs}\}$ , as the measurements have a conditional probability  $\mathcal{P}(d_i|\boldsymbol{\theta})$  to be observed given the value  $\theta$  for the parameters, our problem is to estimate the joint conditional probability

$$L(\mathbf{d}|\boldsymbol{\theta}) = \prod_{i=1}^n \mathcal{P}(d_i|\boldsymbol{\theta}) \quad (\text{A.1})$$

from the observations  $\mathbf{d}$ . In the above definition, we thought of  $L$  as a function of the random variable  $X$ ; however, once the observations have been done, we can think of  $L$  rather as a function of the unknown parameters  $\boldsymbol{\theta}$  for a given value of  $\mathbf{d}$  and call it the *Likelihood Function* (LF).

The *maximum likelihood principle* affirms that as an estimate for  $\boldsymbol{\theta}$  we should choose the value  $\boldsymbol{\theta}^*$  which makes the probability of the actual result obtained,  $\mathbf{d}$ , as large as it can be, i.e.

$$L(\mathbf{d}|\boldsymbol{\theta}^*) \geq L(\mathbf{d}|\boldsymbol{\theta}) \quad \forall \boldsymbol{\theta}. \quad (\text{A.2})$$

It is also common, instead of maximizing the LF, to minimize the lognormal LF

$$\mathcal{L} = -2 \ln L. \quad (\text{A.3})$$

If the PDF is Gaussian, then the maximum likelihood estimation reduces to the usual least square fit: suppose that the measured  $d_i^{obs}$  are independent from each other and Gaussian distributed around their (unknown) true values  $d_i(\boldsymbol{\theta})$ , with a variance given by the experimental errors  $\sigma_i^{obs}$ . Then minimizing  $\mathcal{L}$  is equivalent to the minimization of the chi-square

$$\chi^2(\boldsymbol{\theta}) = \sum_{i=1}^n \left( \frac{d_i^{obs} - d_i}{\sigma_i^{obs}} \right)^2. \quad (\text{A.4})$$

The maximum likelihood principle can be used to extract parameters from the CMB data as the estimated parameters must minimize the chi-square constructed with the observed spectra  $C_\ell^{obs}$  and their errors  $\sigma_\ell$ . This procedure only gives information about the set of parameters which are the “most probable” to have generated the measurements at hand. However, quantifying the error on our estimate for the parameters is a more subtle business, since it involves dwelling into the exact definition of what probability means. There is a long dispute going on among specialists about the correct interpretation of probability, and some fundamental issues are still unresolved. One can take fundamentally two different point of views on the subject, the orthodox (frequentist) approach [129] or the Bayesian [130] point of view; we will now focus on the Bayesian point of view as we adopt this approach in order to obtain the errors on the parameter estimation.

## A.1 Statistical Inference

Bayesian inference is based on Bayes’ Theorem, which is nothing more than rewriting the definitions of conditional probability:

$$\mathcal{P}(A|B) = \frac{\mathcal{P}(B|A)\mathcal{P}(A)}{\mathcal{P}(B)}. \quad (\text{A.5})$$

In order to apply this theorem to our problem let us write  $\boldsymbol{\theta}$  for  $A$  and  $\mathbf{d}$  for  $B$  obtaining

$$\mathcal{P}(\boldsymbol{\theta}|\mathbf{d}) = \frac{L(\mathbf{d}|\boldsymbol{\theta})\mathcal{P}(\boldsymbol{\theta})}{\int d\boldsymbol{\theta}\mathcal{P}(\mathbf{d}|\boldsymbol{\theta})\mathcal{P}(\boldsymbol{\theta})} = \frac{L(\mathbf{d}|\boldsymbol{\theta})\mathcal{P}(\boldsymbol{\theta})}{\mathcal{P}(\mathbf{d})}; \quad (\text{A.6})$$

this equation relates the *posterior probability*  $\mathcal{P}(\boldsymbol{\theta}|\mathbf{d})$  for the parameters  $\boldsymbol{\theta}$  given the data  $\mathbf{d}$  to the likelihood function  $L(\mathbf{d}|\boldsymbol{\theta})$  if the *prior PDF*  $\mathcal{P}(\boldsymbol{\theta})$  for the parameters is known. The quantity at the denominator is independent of  $\boldsymbol{\theta}$  and it is called the *evidence* of the data for a certain model [131] and can be thought as a normalization constant.

Thus the Bayes’ theorem can be summarized as

$$\text{posterior} = \frac{\text{likelihood} \times \text{prior}}{\text{evidence}}. \quad (\text{A.7})$$

The prior distribution contains all the knowledge about the parameters before observing the data: our physical understanding of the model, our insight into the experimental setup and its performance, thus the amount of all our prior scientific experience. This information is then updated via Bayes theorem to the posterior distribution, by multiplying the prior with the LF which contains the information coming from the data. The posterior probability is the base for inference about  $\boldsymbol{\theta}$ : the most probable value for the parameters is the one for which the posterior probability is largest.

In absence of other arguments, the prior probability should be assumed to be equal for all values of the parameters over a certain range,  $\boldsymbol{\theta}_{min} \leq \boldsymbol{\theta} \leq \boldsymbol{\theta}_{max}$ . This is called a *flat prior*, i.e.

$$\mathcal{P}(\boldsymbol{\theta}) = [H(\boldsymbol{\theta} - \boldsymbol{\theta}_{min})H(\boldsymbol{\theta}_{max} - \boldsymbol{\theta})] \prod_{i=1}^p \frac{1}{\theta_i^{max} - \theta_i^{min}} \quad (\text{A.8})$$

where  $H$  is the Heaviside function and  $\theta_i^{max} \geq \theta_i^{min} \forall i$ . This is one of the principal conceptual difficulties of Bayesian inference: a flat prior on  $\boldsymbol{\theta}$  does not correspond to a flat prior on some other set  $f(\boldsymbol{\theta})$ , obtained via a non-linear transformation  $f$ . Therefore the result of Bayesian inference do depend on the choice of priors, as we saw in Section 6.1.3.

We see from Eq.(A.6) that the Maximum Likelihood principle is equivalent to Bayesian inference in the case of flat priors. There is however an important conceptual difference: by writing the posterior distribution as

$$\mathcal{P}(\boldsymbol{\theta}|\mathbf{d}) = \frac{\mathcal{P}(\mathbf{d}, \boldsymbol{\theta})}{\mathcal{P}(\mathbf{d})} \quad (\text{A.9})$$

it follows that Bayes' Theorem imposes to maximise the joint probability  $\mathcal{P}(\mathbf{d}, \boldsymbol{\theta})$  of  $\boldsymbol{\theta}$ ,  $\mathbf{d}$ , while Maximum Likelihood requires that the conditional probability  $L(\mathbf{d}, \boldsymbol{\theta})$  should be maximised.

### A.1.1 Likelihood Intervals

Bayesian statistics use the likelihood function to perform an interval estimation for  $\boldsymbol{\theta}$ : basing on Bayes' Theorem, 4.28, we not only consider the maximum likelihood point in parameter space as the "most likely" value of the unknown parameter; we shall also interpret values further and further away as less and less likely to have generated the particular measurement that we obtained. Hence likelihood intervals drawn from the likelihood function measure our "degree of confidence" that the particular set of observations was generated by a parameter belonging to the estimated interval.

From now on we will write the likelihood function as  $L(\boldsymbol{\theta})$  instead of  $L(\boldsymbol{\theta}, \mathbf{d})$  in order to simplify the notation. Furthermore, we will assume that the likelihood function is a multivariate Gaussian distribution in the  $p$  parameters  $\boldsymbol{\theta}$ , i.e.

$$L(\boldsymbol{\theta}) = \frac{\exp[-\mathcal{L}/2]}{\sqrt{\det \mathbf{C}} (2\pi)^{p/2}} \quad (\text{A.10})$$

$$\mathcal{L} = -2 \ln L = (\boldsymbol{\theta} - \boldsymbol{\mu})^T \mathbf{C}^{-1} (\boldsymbol{\theta} - \boldsymbol{\mu}) \quad (\text{A.11})$$

where  $T$  denotes transposition,  $\boldsymbol{\mu}$  is the expectation value of the parameters  $\boldsymbol{\mu} \equiv \langle \boldsymbol{\theta} \rangle$  and  $\mathbf{C}$  is the covariance matrix

$$C_{ij} \equiv \langle (\theta_i - \mu_i) (\theta_j - \mu_j) \rangle. \quad (\text{A.12})$$

We can do the Taylor expansion of a general likelihood function around its maximum, which is given by our maximum likelihood estimation  $\boldsymbol{\theta}^*$ ; as by definition of maximum likelihood the first derivatives vanish, we obtain

$$\mathcal{L}(\boldsymbol{\theta}) \approx \mathcal{L}(\boldsymbol{\theta}^*) + \frac{1}{2} \sum_{ij} (\theta_i - \theta_i^*) \frac{\partial^2 \mathcal{L}}{\partial \theta_i \partial \theta_j} (\theta_j - \theta_j^*) \quad (\text{A.13})$$

If the likelihood function is sharply peaked around  $\boldsymbol{\theta}^*$ , i.e. the errors on the parameters are small enough, then third order terms can be neglected and the above Gaussian form is a good enough approximation everywhere in parameter space. By

comparing with Eq.(A.11) we find that the covariance matrix can thus be estimated as

$$\hat{\mathbf{C}} = \mathbf{F}^{-1} \quad \text{where} \quad F_{ij} \equiv \left\langle \frac{1}{2} \frac{\partial^2 \mathcal{L}}{\partial \theta_i \partial \theta_j} \right\rangle_{|\theta^*} \quad (\text{A.14})$$

and  $\mathbf{F}$  is called *Fisher information matrix* [129]. According to our understanding of the likelihood function as a measure of our degree of belief for the possible values of  $\boldsymbol{\theta}$ , the probability that parameters within a certain region from the maximum likelihood point have generated the observations should be proportional to the likelihood content of the region. The probability content depends on whether we are estimating all parameters jointly, or keeping some of them fixed to their maximum likelihood value, or rather disregarding a certain subset by integrating over them (marginalization). We now focus on each case in turn.

### Estimation of all $p$ parameters jointly

From now on we will assume, without loss of generality,  $\boldsymbol{\mu} = \mathbf{0}$ . Contours of constant likelihood define, in the assumption of a gaussian likelihood, hyperellipses in parameter space with some probability content we wish to determine. In order to do this we consider the quadratic form

$$Q(\boldsymbol{\theta}) = \boldsymbol{\theta}^T \mathbf{C}^{-1} \boldsymbol{\theta} \quad (\text{A.15})$$

as for the likelihood function of Eq.(A.10) the condition  $Q(\boldsymbol{\theta}) = Q_\gamma^s$ , where  $s$  is the number of parameters we wish to determine and  $\gamma$  is the desired probability content, for some constant  $Q_\gamma^s$  gives the contours of constant likelihood. It can be shown [129] that the quadratic form  $\mathbf{Q}$  is chi-square distributed with  $s$  degrees of freedom, which allows us to relate  $Q_\gamma^s$  with the probability content of the ellipse. If we want a confidence region containing  $100\gamma\%$  of the joint probability for all  $p$  parameters, then  $s = p$  and  $Q_\gamma^p$  is determined by solving

$$\int_0^{Q_\gamma^p} \mathcal{P}_{\chi_p^2}(u) du = \gamma. \quad (\text{A.16})$$

The projection of the hyperellipse  $Q(\boldsymbol{\theta}) = Q_\gamma^p$  onto each of the parameter axis gives the corresponding likelihood interval for each parameter when all parameter are estimated simultaneously (which we will call *joint likelihood interval*).

It is then a simple geometrical problem to find an analytical expression for the joint likelihood interval for each parameter: for the parameter  $1 \leq d \leq p$ , the intersection of the hyperellipse with the hyperplane defined by  $\hat{\mathbf{y}}_d = c$ , with  $c$  a constant, gives either an hyperellipse in  $p - 1$  dimensions, or a point or else an empty set. The extrema of the joint likelihood interval for the parameter  $d$  are given by the values of  $c$  for which the  $p - 1$  dimensional ellipse reduces to a point.

To find the equation of the  $p - 1$  dimensional ellipse we proceed as follows: define  $\mathbf{C}^{-1} \equiv \mathbf{M}$  and write  $Q(\boldsymbol{\theta}) = Q_\gamma^p$  in the form

$$\tilde{\boldsymbol{\theta}}^T \tilde{\mathbf{M}} \tilde{\boldsymbol{\theta}} + 2c \sum_{j \neq d} m_{dj} \tilde{\theta}_j = Q_\gamma^p - m_{dd} c^2 \quad (\text{A.17})$$

where we have

$$\tilde{\boldsymbol{\theta}} \equiv (\theta_1, \dots, \theta_{d-1}, \theta_{d+1}, \dots, \theta_p) \in \mathbf{R}^{p-1} \quad (\text{A.18})$$



$$\tilde{\mathbf{M}} = \begin{pmatrix} m_{1,1} & \cdots & m_{1,d-1} & m_{1,d+1} & \cdots & m_{1,p} \\ \vdots & & & & & \vdots \\ m_{d-1,1} & \cdots & m_{d-1,d-1} & m_{d-1,d+1} & \cdots & m_{d-1,p} \\ m_{d+1,1} & \cdots & m_{d+1,d-1} & m_{d+1,d+1} & \cdots & m_{d+1,p} \\ \vdots & & & & & \vdots \\ m_{p,1} & \cdots & m_{p,d-1} & m_{p,d+1} & \cdots & m_{p,p} \end{pmatrix} \quad (\text{A.19})$$

We now have to diagonalize the submatrix  $\tilde{\mathbf{M}}$

$$\text{diag}(\lambda_1, \dots, \lambda_{p-1}) \equiv \mathbf{\Lambda} = \mathbf{U}^T \tilde{\mathbf{M}} \mathbf{U} \quad (\text{A.20})$$

finding the eigenvalues  $(\lambda_1, \dots, \lambda_{p-1})$  and the eigenvectors  $(u_1, \dots, u_{p-1})$ . After some algebraic manipulations of Eq.(A.17) we arrive at the equation of the  $p-1$  dimensional hyperellipse

$$\sum_{i=1}^{p-1} \lambda_i z_i^2 = Q_\gamma^p - m_{dd} c^2 + \sum_{i=1}^{p-1} \frac{c^2}{\lambda_i} \left( \sum_{j \neq d} m_{dj} u_{ji} \right)^2 \quad (\text{A.21})$$

where we have defined the new variables

$$z_i \equiv \left( \theta \tilde{U} \right)_i + \frac{c}{\lambda_i} \sum_{j \neq d} m_{dj} u_{ji}, \quad 1 \leq i \leq p-1. \quad (\text{A.22})$$

The above hyperellipse becomes degenerate if

$$\sum_{i=1}^{p-1} \lambda_i z_i^2 = 0 \quad (\text{A.23})$$

from which we obtain a quadratic equation for  $c$  with solutions

$$c_{min,max} = \frac{\pm \sqrt{Q_\gamma^p}}{\sqrt{m_{dd} - \sum_{i=1}^{p-1} \lambda_i^{-1} \left( \sum_{j \neq d} m_{dj} u_{ji} \right)^2}}. \quad (\text{A.24})$$

It is easy to show that the positive definiteness condition for the Fisher matrix guarantees that the quantity under the square root in the denominator is always greater than 0. In conclusion, the joint likelihood interval for the parameter  $\hat{\mathbf{y}}_d$  with likelihood content  $\gamma$  is given by

$$c_{min} \leq \theta_d \leq c_{max}. \quad (\text{A.25})$$

### Estimation of $k < p$ parameters, the others fixed

We will not always need to estimate all the  $p$  parameters of a given theory, but we would rather focus on a subset  $k < p$  of parameters, while assuming the others  $p - k$  as known. Without losing in generality we will consider the first  $k$  parameters as those we are interested in and we split the parameters vector as

$$\boldsymbol{\theta} = \begin{pmatrix} \mathbf{t} \\ \mathbf{u} \end{pmatrix} \quad (\text{A.26})$$

with  $\mathbf{t} \in \mathbf{R}^k$  and  $\mathbf{u} \in \mathbf{R}^{p-k}$ . Correspondingly we write the covariance matrix in Eq.(A.11) as the Fisher matrix estimate of Eq.(A.14)

$$\mathbf{C}^{-1} = \mathbf{F} = \begin{pmatrix} \mathbf{A} & \mathbf{G} \\ \mathbf{G}^T & \mathbf{B} \end{pmatrix} \quad (\text{A.27})$$

where  $\mathbf{A} \in \mathbf{R}^{k \times k}$ ,  $\mathbf{B} \in \mathbf{R}^{p-k \times p-k}$  and  $\mathbf{G} \in \mathbf{R}^{p-k \times k}$ .

If the known parameters  $\mathbf{u}$  are held fixed at their maximum likelihood value, the likelihood function for the parameters of interests  $\mathbf{t}$  is simply the full likelihood function restricted to the  $k$  subspace

$$L(\mathbf{t}|\mathbf{u}^*) \propto \exp \left[ -\frac{1}{2} \mathbf{t}^T \mathbf{A} \mathbf{t} \right] \quad (\text{A.28})$$

with an appropriate normalization constant, and the new covariance matrix  $\mathbf{V} \in \mathbf{R}^{k \times k}$  for the  $k$  parameters of interest is

$$\mathbf{V} = \mathbf{A}^{-1} \quad (\text{A.29})$$

Let us consider as an example the best case scenario where all the parameters but one are known exactly thanks to previous experiments or by theoretical considerations and therefore  $k = 1$ . Then the  $1 - \sigma$  likelihood interval for the first parameter only is the square root of the covariance matrix element, and it is given by

$$\sigma_1 = \frac{1}{\sqrt{F_{11}}} \quad (\text{A.30})$$

### Estimation of $k < p$ parameters, the others marginalized

It will not be always possible to obtain the exact value of many parameters, so it is useful to describe how to disregard the parameters we are not interested in by integrating them away from the likelihood function obtaining the *marginalized* likelihood in the  $k$  parameters of interest

$$L(\mathbf{t}) \propto \int_{\Omega_u} L(\mathbf{t}|\mathbf{u}) \quad (\text{A.31})$$

with a suitable normalization constant so that the probability content of the marginalized likelihood function is equal to unity.

The marginalized likelihood function for  $\mathbf{t}$  is still a multivariate Gaussian, with the same covariance matrix as the full likelihood function, only with the last  $p - k$  rows and columns deleted:

$$V_{ij} = [\mathbf{F}]_{ij}^{-1} \quad 1 \leq i, j \leq k \quad (\text{A.32})$$

In terms of the splitting of Eq.(A.27), the covariance matrix for the marginalized distribution is

$$\mathbf{V} = [\mathbf{A} - \mathbf{G}\mathbf{B}\mathbf{G}^T]^{-1} \quad (\text{A.33})$$

Usually, one quotes marginalized likelihood intervals for one parameter alone,  $k = 1$  with all other parameters marginalized, in which case the  $1 - \sigma$  error is given by

$$\sigma_1 = \sqrt{\mathbf{F}_{11}^{-1}} \quad (\text{A.34})$$

If the parameters are uncorrelated, then  $\mathbf{F}$  is diagonal, and fixing  $\mathbf{u}$  or marginalizing over them is equivalent, otherwise the resulting likelihood intervals for the parameter(s) of interest are in general different, with the marginalized interval being broader.

Nevertheless, in practical applications, involving up to a dozen parameters, it is quite a demanding task to perform the multidimensional integral of Eq.(6.5). A computationally more feasible alternative which avoids the time consuming integration is to maximize the parameters we are not interested in,  $\mathbf{u}$ , for each value of the parameters of interest,  $\mathbf{t}$ , obtaining

$$L(\mathbf{t}) \propto \max_{\mathbf{u}} L(\mathbf{t}, \mathbf{u}). \quad (\text{A.35})$$

If the distribution is Gaussian, then the two procedures give the same result: maximizing  $L(\mathbf{t}, \mathbf{u})$  corresponds to minimization over  $\mathbf{u}$  of the quadratic form  $\boldsymbol{\theta}^T \mathbf{C} \boldsymbol{\theta}$ . Differentiating with respect to  $\mathbf{u}$ , we find that the minimum of the quadratic form lies at

$$\mathbf{u} = -\mathbf{B}^{-1} \mathbf{G}^T \mathbf{t} \quad (\text{A.36})$$

and therefore

$$L(\mathbf{t}) \propto \exp \left[ -\frac{1}{2} \mathbf{t}^T \left( \mathbf{A} - \mathbf{G} \mathbf{B}^{-1} \mathbf{G}^T \right) \mathbf{t} \right] \quad (\text{A.37})$$

which is the same result found in Eq.(A.33) marginalizing over  $\mathbf{u}$ . Numerical investigations have found that maximization tends to underestimate errors when the assumption of a Gaussian distribution is not accurately fulfilled [132].

## A.2 Monte Carlo Markov Chain

At first sight, the best way to numerically fit the data is to determine the shape of the likelihood function by evaluating the least-square estimator Eq.(A.4) at each point on a grid in the  $p$  dimensional parameter space and the minimization of the chi-square in the desired range of parameters gives the maximum likelihood estimate.

Nevertheless this method became less and less useful as the accuracy of new CMB experiments made it really expensive from the computational point of view. In order to overcome this problem Markov chain Monte Carlo (hereafter MCMC) methods are now becoming the standard tool to determine parameters from CMB data, combine it with large scale structure constraints or investigate the effect of different priors. MCMC [133] is a method to generate a sequence of (correlated) samples, called a Markov chain, from the posterior pdf of the parameters given the data, as in Eq.(A.6). The great advantages are that the computational time scales approximately linearly with the number of dimensions of the parameter space, and that once the chain has properly converged (see below for more details), the marginalized posterior distribution for the parameter(s) of interest can be simply recovered by plotting histograms of the sample list, thus avoiding completely the costly integration. It is easy to adjust the prior information or to include new data-sets into an existing chain without having to recompute it, with a procedure called *importance sampling*.

Moreover, the Monte Carlo sampling does not rely on the assumption of Gaussian

probability distribution functions: indeed, the direct sampling of the posterior permits to reveal features due to its non-Gaussian distribution, and therefore vastly improves on the methods based on chi-square goodness-of-fit described above.

For further details about MCMC methods see e.g. [131, 134].

At the core of the sample generation there is the *Metropolis-Hastings algorithm* [135, 136], and produces a Markov chain whose equilibrium distribution is the target probability density, here the posterior  $\mathcal{P}(\boldsymbol{\theta}|\mathbf{d})$ . The chain is started from a random point in parameter space,  $\boldsymbol{\theta}_0$ , and a new point  $\boldsymbol{\theta}_1$  is proposed with an arbitrarily *proposal density distribution*  $q(\boldsymbol{\theta}_n, \boldsymbol{\theta}_{n+1})$ . The *transition kernel*  $T(\boldsymbol{\theta}_n, \boldsymbol{\theta}_{n+1})$  gives the conditional probability for the chain to move from  $\boldsymbol{\theta}_n$  to  $\boldsymbol{\theta}_{n+1}$ , and it must satisfy the *detailed balance*

$$\mathcal{P}(\boldsymbol{\theta}_{n+1}|\mathbf{d}) T(\boldsymbol{\theta}_{n+1}, \boldsymbol{\theta}_n) = \mathcal{P}(\boldsymbol{\theta}_n|\mathbf{d}) T(\boldsymbol{\theta}_n, \boldsymbol{\theta}_{n+1}). \quad (\text{A.38})$$

The posterior  $\mathcal{P}(\boldsymbol{\theta}|\mathbf{d})$  is the stationary distribution of the chain if the transition kernel is defined as

$$T(\boldsymbol{\theta}_n, \boldsymbol{\theta}_{n+1}) \equiv q(\boldsymbol{\theta}_n, \boldsymbol{\theta}_{n+1}) \alpha(\boldsymbol{\theta}_n, \boldsymbol{\theta}_{n+1}) \quad (\text{A.39})$$

where  $\alpha(\boldsymbol{\theta}_n, \boldsymbol{\theta}_{n+1})$  gives the probability that the new point is accepted and it is defined as

$$\alpha(\boldsymbol{\theta}_n, \boldsymbol{\theta}_{n+1}) \equiv \min \left\{ 1, \frac{\mathcal{P}(\boldsymbol{\theta}_{n+1}|\mathbf{d}) q(\boldsymbol{\theta}_{n+1}, \boldsymbol{\theta}_n)}{\mathcal{P}(\boldsymbol{\theta}_n|\mathbf{d}) q(\boldsymbol{\theta}_n, \boldsymbol{\theta}_{n+1})} \right\} \quad (\text{A.40})$$

Since  $\mathcal{P}(\boldsymbol{\theta}|\mathbf{d}) \propto L(\mathbf{d}|\boldsymbol{\theta}) \mathcal{P}(\boldsymbol{\theta})$  and for the usual case of a symmetric proposal density,  $q(\boldsymbol{\theta}_n, \boldsymbol{\theta}_{n+1}) = q(\boldsymbol{\theta}_{n+1}, \boldsymbol{\theta}_n)$ , the new step is always accepted if it improves on the posterior, otherwise it is accepted with probability  $L(\mathbf{d}|\boldsymbol{\theta}_{n+1}) \mathcal{P}(\boldsymbol{\theta}_{n+1}) / L(\mathbf{d}|\boldsymbol{\theta}_n) \mathcal{P}(\boldsymbol{\theta}_n)$ . The result is a sample list from the target distribution, from which all the statistical quantities of interest can readily be evaluated. The samples are correlated with each other, a fact which does not constitute a problem for the statistical inference on the parameters.

# Bibliography

- [1] Einstein A., Sitzungsber. Preuss. Akad. Wiss. phys.-math. Klasse VI, 142 (1917)
- [2] Misner C.W., Thorne K.S., Wheeler J.A., Gravitation, W. H. Freeman and Company (1973)
- [3] N. Straumann, General Relativity and Relativistic Astrophysics, Springer-Verlag (1984)
- [4] Carroll S.M., An Introduction to General Relativity: Spacetime and Geometry, Addison Wesley (2004)
- [5] Tully R. B., Fisher J. R., Astronomy and Astrophysics, vol. 54, no. 3, 661 (1977)
- [6] E. Komatsu *et al.* [WMAP Collaboration], Astrophys. J. Suppl. **192** (2011) 18
- [7] E. L. Wright, S. S. Meyer, C. L. Bennett, N. W. Boggess, E. S. Cheng, M. G. Hauser, A. Kogut, C. Lineweaver *et al.*, Astrophys. J. **396** (1992) L13-L18.
- [8] P. de Bernardis *et al.* [Boomerang Collaboration], Proc. of the CAPP2000 conference, Verbier, arXiv:astro-ph/0011469.
- [9] G. Steigman, Int. J. Mod. Phys. E **15** (2006) 1.
- [10] S. Dodelson, Modern Cosmology, Academic Press (2003)
- [11] R. H. Brandenberger, Lect. Notes Phys. **646** (2004) 127.
- [12] R. Durrer, Lect. Notes Phys. **653** (2004) 31.
- [13] A. G. Riess *et al.* [Supernova Search Team Collaboration], Astrophys. J. **607** (2004) 665.
- [14] A. Klypin, H. Zhao, R. S. Somerville, Astrophys. J. **573** (2002) 597-613.
- [15] R. Jimenez, P. Thejll, U. Jorgensen, J. MacDonald and B. Pagel, Mon. Not. Roy. Astron. Soc. **282** (1996) 926-942
- [16] R. Amanullah *et al.*, Astrophys. J. **716** (2010) 712.
- [17] C. H. Lineweaver, C. A. Egan, Astrophys. J. **671** (2007) 853.

- [18] N. Straumann, In \*Duplantier, B. (ed.) et al.: Vacuum energy, renormalization\* 7-51, arXiv:astro-ph/0203330.
- [19] E. J. Copeland, M. Sami and S. Tsujikawa, Int. J. Mod. Phys. D **15** (2006) 1753.
- [20] J. Frieman, M. Turner and D. Huterer, Ann. Rev. Astron. Astrophys. **46** (2008) 385.
- [21] R. R. Caldwell, R. Dave and P. J. Steinhardt, Phys. Rev. Lett. **80** (1998) 1582.
- [22] T. Padmanabhan, Phys. Rept. **380** (2003) 235.
- [23] S. M. Carroll, Phys. Rev. Lett. **81** (1998) 3067.
- [24] S. Tsujikawa, review chapter on dark energy for a book "Dark Matter and Dark Energy: a Challenge for the 21st Century", arXiv:1004.1493 [astro-ph.CO].
- [25] M. Li, X. D. Li, S. Wang and Y. Wang, Commun. Theor. Phys. **56**, 525 (2011)
- [26] Weyl H., Ann. Phys. **59**, 101 (1919)
- [27] Eddington A. S., *The Mathematical Theory of Relativity*, Cambridge University Press (1923)
- [28] Utiyama R., DeWitt B.S., Journal of Mathematical Physics **3**, 608 (1962)
- [29] G. R. Dvali, G. Gabadadze and M. Porrati, Phys. Lett. B **485**, 208 (2000).
- [30] C. Deffayet, G. R. Dvali and G. Gabadadze, Phys. Rev. D **65** (2002) 044023.
- [31] S. Nojiri, S. D. Odintsov and M. Sasaki, Phys. Rev. D **71** (2005) 123509.
- [32] S. Tsujikawa, Lect. Notes Phys. **800** (2010) 99.
- [33] S. Capozziello, M. De Laurentis, Phys. Rep. doi:10.1016/j.physrep.2011.09.003
- [34] S. Capozziello, M. De Laurentis, V. Faraoni, The Open Astronomy Journal **2**, 1874, (2009)
- [35] R. P. Woodard, Lect. Notes Phys. **720** (2007) 403.
- [36] G. Magnano and L. M. Sokolowski, Phys. Rev. D **50** (1994) 5039.
- [37] S. Capozziello, P. Martin-Moruno, C. Rubano, Phys. Lett. **B689** (2010) 117-121.
- [38] S. Capozziello, Int. J. Mod. Phys. D **11** (2002) 483.
- [39] L. Amendola, R. Gannouji, D. Polarski and S. Tsujikawa, Phys. Rev. D **75** (2007) 083504.
- [40] W. Hu and I. Sawicki, Phys. Rev. D **76** (2007) 064004.
- [41] S. Capozziello, M. De Laurentis, S. Nojiri, S. D. Odintsov, Gen. Rel. Grav. **41** (2009) 2313-2344.

- [42] S. Capozziello, M. De Laurentis, S. Nojiri, S. D. Odintsov, Phys. Rev. **D79** (2009) 124007.
- [43] T. Faulkner, M. Tegmark, E. F. Bunn and Y. Mao, Phys. Rev. D **76** (2007) 063505.
- [44] S. Capozziello and S. Tsujikawa, Phys. Rev. D **77** (2008) 107501.
- [45] Clifford M. Will, Living Rev. Relativity 9, (2006), 3. URL (cited on December 9, 2011): <http://www.livingreviews.org/lrr-2006-3>
- [46] R. Bean, D. Bernat, L. Pogosian, A. Silvestri and M. Trodden, Phys. Rev. D **75** (2007) 064020.
- [47] Z. Girones, A. Marchetti, O. Mena, C. Pena-Garay and N. Rius, JCAP **1011** (2010) 004.
- [48] G. B. Zhao, L. Pogosian, A. Silvestri and J. Zylberberg, Phys. Rev. D **79** (2009) 083513.
- [49] T. Giannantonio, M. Martinelli, A. Silvestri and A. Melchiorri, JCAP **1004** (2010) 030.
- [50] <http://www.sfu.ca/~aha25/MGCAMB.html>
- [51] S. Capozziello, V. F. Cardone, V. Salzano, Phys. Rev. **D78** (2008) 063504.
- [52] L. Izzo, S. Capozziello, G. Covone, M. Capaccioli, A&A **508**, 63-67 (2009)
- [53] M. Hamuy et al., Astron. J. **106**, 2392 (1993)
- [54] M. M. Phillips Astrophys. J. **413** (1993) L105
- [55] J. Albert *et al.* [ SNAP Collaboration ], [astro-ph/0507460].
- [56] T. Okumura, T. Matsubara, D. J. Eisenstein, I. Kayo, C. Hikage, A. S. Szalay and D. P. Schneider, Astrophys. J. **676** (2008) 889.
- [57] D. J. Eisenstein *et al.* [ SDSS Collaboration ], Astrophys. J. **633** (2005) 560-574.
- [58] S. Cole *et al.* [ The 2dFGRS Collaboration ], Mon. Not. Roy. Astron. Soc. **362** (2005) 505-534.
- [59] W. Hu and N. Sugiyama, Astrophys. J. **471** (1996) 542.
- [60] G. Efstathiou and J. R. Bond, Mon. Not. Roy. Astron. Soc. **304** (1999) 75.
- [61] O. Elgaroy and T. Multamaki, A&A **471**, 65-70 (2007)
- [62] J. Simon, L. Verde and R. Jimenez, Phys. Rev. D **71** (2005) 123001.
- [63] R. Jimenez, J. MacDonald, J. S. Dunlop, P. Padoan and J. A. Peacock, Mon. Not. Roy. Astron. Soc. **349** (2004) 240.
- [64] R. Jimenez, L. Verde, T. Treu and D. Stern, Astrophys. J. **593** (2003) 622.

- [65] M. Tegmark, Proc. Enrico Fermi, Course CXXXII, Varenna, 1995
- [66] P. -S. Corasaniti, T. Giannantonio, A. Melchiorri, Phys. Rev. **D71** (2005) 123521.
- [67] L. Perotto, J. Lesgourgues, S. Hannestad, H. Tu and Y. Y. Y. Wong, JCAP **0610** (2006) 013.
- [68] C. M. Hirata and U. Seljak, Phys. Rev. D **68** (2003) 083002.
- [69] T. Okamoto and W. Hu, Phys. Rev. D **67** (2003) 083002.
- [70] J. A. Peacock, Phil. Trans. Roy. Soc. Lond. A **361** (2003) 2479.
- [71] M. Bartelmann and P. Schneider, Phys. Rept. **340** (2001) 291.
- [72] S. Hannestad, H. Tu and Y. Y. Y. Wong, JCAP **0606** (2006) 025.
- [73] F. Bernardeau, C. Pitrou, J. -P. Uzan, JCAP **1102** (2011) 015.
- [74] M. Martinelli, A. Melchiorri and L. Amendola, Phys. Rev. D **79** (2009) 123516.
- [75] A. Dev, D. Jain, S. Jhingan, S. Nojiri, M. Sami and I. Thongkool, Phys. Rev. D **78** (2008) 083515
- [76] M. Kowalski *et al.*, Astrophys. J. **686** (2008) 749.
- [77] J. Simon, L. Verde and R. Jimenez, Phys. Rev. D **71** (2005) 123001.
- [78] W. L. Freedman *et al.* [HST Collaboration], Astrophys. J. **553**, 47 (2001).
- [79] D. J. Eisenstein *et al.* Astrophys. J. **533** (2006) 47
- [80] H. Akaike IEEE Trans. Auto. Control **19** (1974) 716
- [81] G. Schwarz Annals of Statistics **5** (1978) 461
- [82] M. Martinelli, A. Melchiorri, O. Mena, V. Salvatelli, Z. Girones, [arXiv:1109.4736 [astro-ph.CO]].
- [83] A. G. Kim, E. V. Linder, R. Miquel, N. Mostek, Mon. Not. Roy. Astron. Soc. **347** (2004) 909-920.
- [84] N. Kaiser, Mon. Not. Roy. Astron. Soc. **227** (1987) 1-27.
- [85] D. J. Eisenstein *et al.* [ SDSS Collaboration ], Astron. J. **142** (2011) 72.
- [86] A. Refregier *et al.*, Proc. SPIE **6265**, 62651Y (2006)
- [87] [Planck Collaboration], arXiv:astro-ph/0604069.
- [88] L. Verde, H. Peiris, R. Jimenez, JCAP **0601** (2006) 019.
- [89] M. White, Y. -S. Song, W. J. Percival, Mon. Not. Roy. Astron. Soc. **397** (2008) 1348-1354.



- [90] A. Lewis and S. Bridle, Phys. Rev. D **66**, 103511 (2002) (Available from <http://cosmologist.info>.)
- [91] A. Lewis, A. Challinor and A. Lasenby, Astrophys. J. **538** (2000) 473
- [92] M. R. Nolta *et al.* [WMAP Collaboration], Astrophys. J. Suppl. **180** (2009) 296
- [93] T. Giannantonio, R. Scranton, R. G. Crittenden, R. C. Nichol, S. P. Boughn, A. D. Myers and G. T. Richards, Phys. Rev. D **77** (2008) 123520
- [94] Y. S. Song, H. Peiris and W. Hu, Phys. Rev. D **76** (2007) 063517
- [95] A. G. Riess *et al.*, Astrophys. J. **699** (2009) 539
- [96] R. Bean, E. E. Flanagan, I. Laszlo and M. Trodden, Phys. Rev. D **78** (2008) 123514
- [97] J. Valiviita and T. Giannantonio, Phys. Rev. D **80** (2009) 123516
- [98] M. Tegmark, Phys. Rev. D **56** (1997) 4514
- [99] J. Bock *et al.* [EPIC Collaboration], arXiv:0906.1188 [astro-ph.CO].
- [100] A. F. Heavens, 2003, Mon. Not. Roy. Astron. Soc. , **323**, 1327
- [101] P. G. Castro, A. F. Heavens, T. D. Kitching, 2005, Phys. Rev. D, **72**, 3516
- [102] A. F. Heavens, T. D. Kitching, A. N. Taylor, 2006, Mon. Not. Roy. Astron. Soc. , **373**, 105
- [103] T. D. Kitching, A. F. Heavens, A. N. Taylor, M. L. Brown, K. Meisenheimer, C. Wolf, M. E. Gray, D. J. Bacon, 2007, Mon. Not. Roy. Astron. Soc. , **376**, 771
- [104] Bacon, D.; et al.; 2003; Mon. Not. Roy. Astron. Soc. , 363, 723-733
- [105] Massey R.; et al.; 2007, ApJS, 172, 239
- [106] Taylor, A. N.; et al.; 2004, Mon. Not. Roy. Astron. Soc. , 353, 1176
- [107] M. Martinelli, E. Calabrese, F. De Bernardis, A. Melchiorri, L. Pagano and R. Scaramella, Phys. Rev. D **83** (2011) 023012
- [108] A. R. Cooray, Astron. Astrophys. **348** (1999) 31
- [109] R. E. Smith *et al.* [The Virgo Consortium Collaboration], Mon. Not. Roy. Astron. Soc. **341** (2003) 1311
- [110] F. B. Abdalla, A. Amara, P. Capak, E. S. Cypriano, O. Lahav and J. Rhodes, Mon. Not. Roy. Astron. Soc. **387** (2008) 969
- [111] L. Fu *et al.*, Astron. Astrophys. **479** (2008) 9
- [112] E. Komatsu et al. 2011 ApJS **192** 1

- [113] A. Refregier, A. Amara, T. D. Kitching, A. Rassat, R. Scaramella, J. Weller and f. t. E. Consortium, arXiv:1001.0061 [astro-ph.IM].
- [114] F. De Bernardis, L. Pagano, P. Serra, A. Melchiorri and A. Cooray, JCAP **0806** (2008) 013
- [115] J. R. Bond, G. Efstathiou and M. Tegmark, Mon. Not. Roy. Astron. Soc. **291** (1997) L33
- [116] J. Valiviita, E. Majerotto and R. Maartens, JCAP **0807**, 020 (2008).
- [117] J. H. He, B. Wang and E. Abdalla, Phys. Lett. B **671**, 139 (2009).
- [118] B. M. Jackson, A. Taylor and A. Berera, Phys. Rev. D **79**, 043526 (2009).
- [119] M. B. Gavela, D. Hernandez, L. L. Honorez, O. Mena and S. Rigolin, JCAP **0907**, 034 (2009).
- [120] M. B. Gavela, L. L. Honorez, O. Mena and S. Rigolin, [arXiv:to be published].
- [121] A. Lewis, A. Challinor and A. Lasenby, Astrophys. J. **538** (2000) 473.
- [122] G. Caldera-Cabral, R. Maartens and B. M. Schaefer, JCAP **0907**, 027 (2009)
- [123] Y. S. Song, L. Hollenstein, G. Caldera-Cabral and K. Koyama, JCAP **1004**, 018 (2010).
- [124] L. L. Honorez, B. A. Reid, O. Mena, L. Verde and R. Jimenez, JCAP **1009**, 029 (2010)
- [125] M. Martinelli, L. Lopez Honorez, A. Melchiorri and O. Mena, Phys. Rev. D **81** (2010) 103534
- [126] J. Dunkley *et al.* [WMAP Collaboration], Astrophys. J. Suppl. **180** (2009) 306; E. Komatsu *et al.* [WMAP Collaboration], Astrophys. J. Suppl. **180** (2009) 330.
- [127] F. De Bernardis, M. Martinelli, A. Melchiorri, O. Mena and A. Cooray, Phys. Rev. D **84** (2011) 023504
- [128] [LSST Science Collaborations and LSST Project Collaboration], arXiv:0912.0201 [astro-ph.IM].
- [129] Kendall, M. & Stuart, A. (1977). The advanced theory of statistics. Griffin & Co, London & High Wycombe, fourth edition. 3 volumes.
- [130] Box, G. E. & Tiao, G. C. (1973). Bayesian inference in statistical analysis. Addison-Wesley series in behavioral science: quantitative methods. Addison-Wesley, Reading, Massachusetts.
- [131] MacKay, D. J. (2003). Information theory, inference, and learning algorithms. Cambridge University Press, Cambridge.
- [132] G. Efstathiou, S. L. Bridle, A. N. Lasenby, M. P. Hobson and R. S. Ellis, Mon. Not. Roy. Astron. Soc. **303** (1999) L47–L52

- 
- [133] N. Christensen, R. Meyer, L. Knox and B. Luey, *Class. Quant. Grav.* **18** (2001) 2677
  - [134] Gilks, W., Richardson, S., & Spiegelhalter, D., editors (1996). *Markov chain Monte Carlo in practice*. Chapman & Hall, London.
  - [135] Metropolis, N., Rosenbluth, A. W., Rosenbluth, M. N., Teller, A. H., & Teller, E. (1953). Equation of state calculations by fast computing machines. *J. Chem. Phys.*, 21:1087-1092.
  - [136] Hastings, W. (1970). Monte Carlo sampling methods using Markov chains and their applications. *Biometrika*, 57:97-109.